Battelle
Columbus Laboratories

Report

DETECTION OF ELECTROMAGNETIC
RADIATION LEAKAGE THROUGH SMALL
STRUCTURAL OPENINGS

to

DEFENSE ADVANCED RESEARCH
PROJECTS AGENCY

September 30, 1983

FINAL REPORT

ARPA Order No. 4576

Under Contract No. MDA903-82-C-0398 issued by
Department of Army, Defense Supply Service-Washington,
Washington, DC 20310

on

DETECTION OF ELECTROMAGNETIC RADIATION LEAKAGE THROUGH SMALL STRUCTURAL OPENINGS

to

DEFENSE ADVANCED RESEARCH
PROJECTS AGENCY

September 30, 1983

by

J. R. Birchmeier, J. G. Meadors,
and K. A. Shubert

BATTELLE
Columbus Laboratories
505 King Avenue
Columbus, Ohio 43201

Battelle
Columbus Laboratories
505 King Avenue
Columbus, Ohio 43201
Telephone (614) 424-6424
Telex 24-5454

September 30, 1983

Director
Defense Advanced Research
Projects Agency
Attention: Program Management
1400 Wilson Boulevard
Arlington, Virginia 22209

Dear Sir:

Enclosed are three copies of the Final Report for the program sponsored under the Contract No. MDA903-82-C-0398 issued by Department of Army, Defense Supply Service-Washington. This report summarizes the results obtained during the period August 10, 1982 - September 30, 1983.

If there are any questions, please contact me at (614) 424-6387.

Sincerely,

John R Birchmeier

John R. Birchmeier
Research Scientist
Electronic Systems and
Technology Section

JRB:mvv

Enc. (3)

xc: Director (3)
DARPA
Attention: TIO/Admin
1400 Wilson Boulevard
Arlington, VA 22209

Defense Documentation Center (12)
Cameron Station
Alexandria, VA 22314

TACTEC (1)
Battelle Memorial Institute
505 King Avenue
Columbus, OH 43201

A1

ACKNOWLEDGMENT

This research program was sponsored by DARPA under contract MDA903-82-C-0398. Dr. Allen Atkins was the COR and provided technical guidance and direction at critical times in this research. The following served as consultants to this program and contributed greatly to its success: Dr. R.E. Collin, M.A. Poirier, Dr. P. Kosel, and Dr. W.H. Peake.

Dr. Collin's contribution offered insight into the sampler design and the behavior of electromagnetic fields on ground planes and near narrow cracks. Mr. Poirier kept a very complex laser system operational and lent his assistance in refining experimental techniques which resulted in meaningful empirical data. Dr. Kosel and the University of Cincinnati fabricated the gallium arsenide switches including the ohmic contacts. Dr. Peake lent his assistance by examining theoretical and experimental techniques and letting his years of experience influence the direction of several technical initiatives.

Contributions of other researchers at Battelle Columbus are also noted. Dr. C.E. Wickersham was responsible for the fabrication of most of the semiconductor switches investigated. Mrs. J.I. Halman was responsible for the calculated data involving the moment method code. Mr. B.L. Chapman performed laser maintenance and implemented most of the experimental procedures.

TABLE OF CONTENTS

SUMMARY

Task Objectives

The purpose of this research program was to develop and demonstrate a system capable of detecting and monitoring the leakage of electromagnetic (EM) energy through cracks, slits, or other openings in a shielded enclosure. Central to this work was the correlation of leakage detection and monitoring with structural deformation. An assumed system constraint limited the placement of any monitoring hardware to the source side of a slit or opening (i.e. the placement of all hardware was limited to the interior of a structure while predicting and/or detecting the EM leakage to the exterior of that structure).

Technical Problems

The proposed system required the development and integration of special hardware and signal processing algorithms. The hardware specifications were primarily determined by the minimum crack dimension to be detected. The hardware dependence on the crack size followed from the expectation that the crack dimension should be a portion of a wavelength at the highest test frequency in free space. To detect leakage through small cracks, time-domain EM techniques with broadband test signals rich in high frequency content offer many practical advantages. The need for high frequency test signals led to the following requirements:

1. Development of a broadband transient EM source and antennas to examine the unknown structure.

2. Development of a broadband transient data acquistion system.

3. Development of the signal processing techniques required to detect the change in a crack structure that allows EM leakage.

4. Integration of the EM source and data acquisition hardware to allow automated measurements to be performed.

General Methodology

An electrically large ground plane with a slit in the center was used as the test fixture. Transmit and receive antennas were mounted on opposite sides of the crack. A broadband EM source was used to excite the transmit antenna, thus launching a wave traveling across the crack to be interrogated. The second antenna received the signal from the transmitter. This received signal was modified by the presence of a crack. The received signal was then processed to characterize the crack and to determine if the crack structure had changed.

The crack structure was modeled using numerical techniques to develop a data base for evaluating leakage measurements. Two models were developed that differed in approach and application. One model, the traveling wave line source model, assumed a short monopole radiating in the presence of a finite thickness ground plane. The second model, the moment method model, assumed only that the transmit and receive antennas were much thinner then they were long, however it was restricted to an infinitesimally thin ground plane. The numerical model used depended on

the configuration of the test structure.

A broadband FM source was exploited to generate fields in the near vicinity of a crack. These fields were used to investigate the nature of the crack and its surrounding structure. The frequency range of interest for this program was from 8 GHz to 18 GHz. Three distinct methods were used to generate the required broadband signals:

1. The source was generated by illuminating the transmit antenna with a short duration, high intensity laser beam. This high intensity illumination caused thermionic emission; the effect of the thermionic emission was the same as a transient current monopole at the target surface. The bandwidth generated was proportional to one over the pulse duration. An infrared laser with a pulse duration of 30 picoseconds (ps) was used to generate bandwidths up to 20 GHz (the theoretical limit is 33 GHz). The short transient pulse generated by the laser was used to perform time-domain measurements and frequency-domain measurements. The laser induced signal had a large component of random noise which was removed through signal processing. However, the laser had a repetition rate of only 10 Hz which made signal processing a time consuming task.

2. A solid state pulser was also used to drive the transmit antenna. The pulser generated an electrical pulse that was similar to that generated by the laser. The solid state pulser was able to generate frequencies up to 12 GHz, however more signal processing could be done in a shorter time since the solid state pulser has a high repetition rate (up to 10 KHz).

3. The frequency-domain continous wave (CW) source was also used to drive the transmit antenna directly. The CW source was a low noise variable frequency signal generator, thus eliminating much of the need for signal processing.

The method of acquisition of the received signal was dependent on the type of source that was driving the transmitter. If the laser or the pulser was used, a time-domain sampler was needed. Two types of

time-domain samplers were used. The first sampler was a real time acquisition system (bandwidth limited to 1 GHz), the second was a repetitive sampling system (bandwidth limited to 14 GHz). A new sampler design was developed as part of this research program; this sampler design exploited ultra-fast optically sensitive switches. Practical implementation of this single transient sampler was limited by the achieved electrical and optical characteristics of photoconducting switches fabricated with amorphous silicon, gallium arsenide, indium phosphide, and galluim antimonide (this sampler is discussed in detail in the Procedures and Findings sections of this report). When the transmitter source was the CW signal generator, a data acquisition system such as a network analyzer was used.

Technical Results

The successful detection of small structure' openings has been demonstrated using electromagnetic fields to probe an unknown crack structure. Using EM fields, with frequency components from 2 GHz to 18 GHz, crack dimensions as small as 0.020 inch were detected. This resolution was limited by the data acquisition system and the mechanical tolerances of the test structure. With higher test frequencies and better measurement hardware this resolution should be improved. The crack detection has been accomplished using time-domain reflectomety (TDR) and frequency-domain analysis. The best measured resolution to date was obtained with frequency-domain (CW) techniques.

The numerical models of the crack structure produced calculated data that agree well with the measured data; the numerical models also predict field levels on the exterior of the structure. Using the results from the models, it was possible to determine in advance if a given crack size could be detected with the existing hardware. In addition, when the measured data were correlated with the predicted data it was possible to determine the leakage level that existed outside the structure. This latter step was important in that it allows exterior leakage levels to be calculated with all instrumentation mounted inside the structure.

The broadband excitation of the transmit antenna has been demonstrated using the laser induced transient pulse, the solid state electronic pulser, and the CW signal generator. The primary limitations of the laser excitation method was the low repetition rate (10 Hz), the pulse-to-pulse amplitude instability (greater than 5%), and the random noise generated by the plasma at the target surface. To reduce the effects of the instability and the random noise, a large amount of signal processing was required. Because of the low repetition rate of the laser, a large amount of time was required to perform the necessary signal processing. This problem will be less severe when improved sampling hardware is available that allows single-shot transient signals to be recorded with bandwidths up to 18 GHz. When the solid state pulser was used as the transient source to drive the transmit antenna, the bandwidth was limited to approximately 12 GHz. This bandwidth was less than desired, but was adequate for the laboratory demonstration of

the system operation. The pulser was able to operate with a repetition rate of 10 KHz, therefore allowing the computer to perform a large amount of signal processing in a short time period. A CW signal generator was also used to excite the transmit antenna. This was done by stepping the CW source over the frequency range from 2 GHz to 18 GHz; the frequency step size was a variable that ranged from 10 MHz to 2 GHz.

A broadband transient sampling device was proposed and a basic design developed. This sampler would be optically switched and be capable of digitizing a transient signal with bandwidths as high as 18 GHz. The sampler would convert the spatial distribution of a signal traveling on a transmission line into a temporal waveform. This would be accomplished by placing switches, connected to "hold" circuitry, at an even spacing along the transmission line. The switches would then be strobed at the same instant in time. The effective sampling time would then be the switch separation divided by the propagation velocity of the signal. The fabrication of the proposed sampler was limited by the availabilty of optically sensitive switches.

Important Findings And Conclusions

The detection of small structural openings has been demonstrated using electromagnetic fields. The smallest crack that was reliably detected was 0.020 inches. It was felt that smaller cracks could be detected with the existing system if a test structure with better mechanical tolerances was used. This resolution was also limited by the data

acquisition system and the highest test frequency used to probe the crack.

The results from the numerical models were used to correlate measured data with predicted data. When the measured and calculated data were correlated, the leakage levels exterior to the structure could be predicted. The numerical models could predict the changes in the field levels for a given change in the crack dimension. Using the calculated changes in the field intensity, it was possible to determine the hardware measurement accuracy required to detect a given size crack. The models also provided some insight into the field structure as a function of crack geometry. This knowledge will allow identification of optimal discriminants for monitoring crack structures.

Significant Hardware Developments

An integrated system utilizing EM techniques for automatically detecting changes in a given crack has been developed. The system was developed as a laboratory demonstration unit. A field worthy system could be developed using the same functional design as the laboratory demonstration system.

Optically sensitive switches have been fabricated using four different materials. To date these switches have not met the specifications needed for their intended application. Because of the performance of the switches that have been fabricated the proposed sampler has not been

demonstrated. With further switch material developments the fabrication of a single-shot transient sample should be possible.

Implications For Further Research

This program has demonstrated the potential of using transient electromagnetic fields to determine simple features of an unknown structure. This technique could, with additional development, be used to detect and predict leakage from a structural opening, make high spatial resolution radar cross section measurements, investigate the transient response of antenna systems, and investigate the resonant behavior of objects. An additional feature of the laser induced source is that it can be used to generate transient signals without contaminating the local area with an electronic feed.

The investigation of simple crack structures has been demonstrated in the laboratory environment. The ability to monitor small changes was limited by the measurement accuracy of the data acquisition system and the highest test frequency used to probe the structure. With additional development, the monitoring system should be able to automatically predict the leakage fields outside of a structure with all monitoring hardware contained inside the structure.

The laser induced transient EM source demonstrated the most promise of providing very broadband signals (up to 33 GHz). The primary limitation was the data acquisition system that was needed to record transient

broadband signals. The optically sensitive switch technology should offer a possible solution to the data acquisition problem. As such, further research and development of this technology should prove valuable.

INTRODUCTION

Experimental methods and techniques that can be used to design transient (broadband) electromagnetic sources have been developed over the past few years. Using optical techniques a target can be excited with an approximate impulse in time with high spatial selectivity corresponding to a point source on the target. This source, induced by laser irradiation, is electromagnetically equivalent to a basic elemental transient current monopole. Electromagnetic interference is minimized, and no electrical connections are required between the target and an external source. Since the current moment vector of the monopole can be controlled very accurately, the visualization of this source as a small, transient current element or dipole antenna located at a selected point on the target with a chosen vector direction is intuitively helpful. From a mathematical perspective, this source corresponds approximately to an impulsive source in both space and time; hence, the response of the target to this type excitation will be related to the Green's function of the target. Knowledge of the Green's function for a target geometry allows calculation of the target response to arbitrary excitation by superposition for linear systems.

Development of this new technology will substantially enhance our current capability in high resolution electromagnetic measurements on targets for analysis of edges, corners and hot spots, in the measurement of the permittivity and permeability of classes of materials, particularly at high frequencies (greater than 16 GHz), in the investigation of mutual coupling among electromagnetic structures common to a single vehicle, and in the

investigation of electromagnetic leakage through very small structural openings. In addition, this experimental diagnostic tool can be used to guide and validate modeling and analysis in the resonance regions of a target where present numerical techniques encounter difficulties.

The purpose of this research program was to investigate methods for detecting and monitoring the leakage of electromagnetic energy through cracks, slits, or other small openings in a shielded enclosure. Instrumentation for accomplishing these technical objectives will be housed and should be compatible with other hardware within the enclosure. Central to this work was the correlation of leakage detection and/or monitoring with structural deformation. The frequency range of interest spans both X and K_u bands, i.e., 8 to 18 GHz. The waveform measurement problem then lies in the picosecond range when considered in the time domain. From the perspective of the frequency domain, the hardware, such as a network analyzer, for monitoring electromagnetic leakage is commercially available but tends to be large in size and measurement methods require relatively long times for broadband investigations. In this research, extensive measurements in both the time and frequency domains were made; but, in terms of projected applications, emphasis was placed on time domain techniques and instrumentation development.

Figure 1 elucidates the technical issues pertinent to solving this measurement problem. A short transient pulse can propagate along a transmission line to a short monopole antenna mounted in a large ground plane as depicted. If the radiated pulse duration is less than the distance

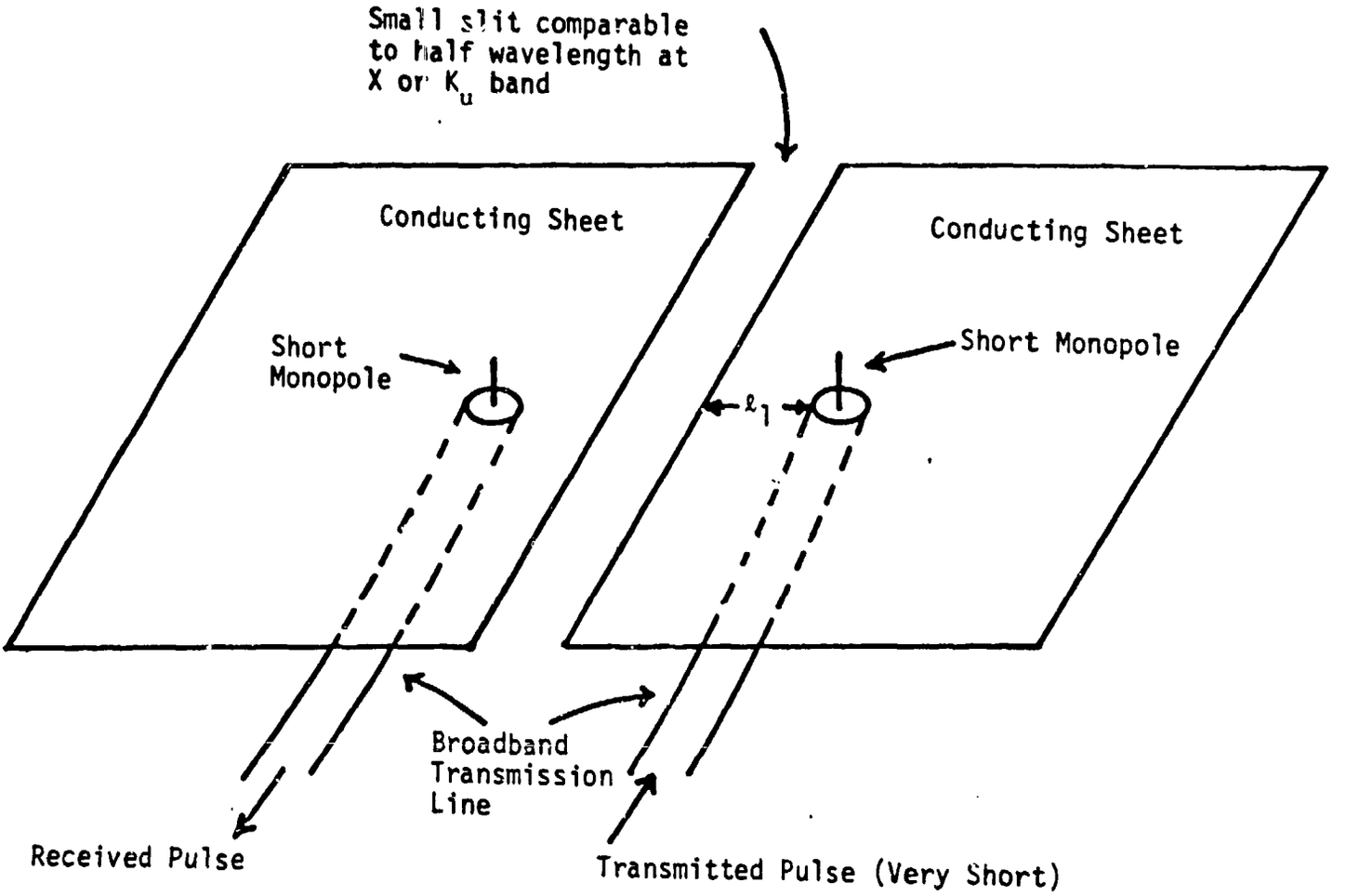

FIGURE 1. CONCEPTUAL ARRANGEMENT FOR IDENTIFYING THE ESSENTIAL FEATURES OF THE EM LEAKAGE PROBLEM

divided by the pulse velocity on the ground plane, the transmitting antenna can also be used to receive the reflected waveform from the slit edges free of interference. By acquisition of the radiated, the reflected, and the transmitted waveforms in real time, the occurrence of electromagnetic leakage through the slit can be ascertained. While similar in geometry to standard single-mode transmission-reflection experiments, the interpretation of measured results requires considerable analysis due to the expanding wavefront along the edge of the crack and the proximity of the crack with the transmit/receive antennas. Practical geometries also include a ground plane finite thickness which causes the crack to exhibit transmission line characteristics. The actual characterization of the crack electromagnetically over a broad frequency range was accomplished by Fourier transformation of the time waveforms and comparison with a detailed model of the crack structure. Alternatively, time domain reflectometry was used to obtain dimensional information on the crack.

The measurement system can be used to detect signals reflected from each electrical discontinuity subject to sensitivity and time resolution limitations. For example, the thickness of the ground plane (or penetration of electromagnetic energy into the crack for finite thickness conducting sheets) and the width of the slit can be determined from the relative timing of reflected pulses provided these electrical field pulses can be acquired in real time.

The technical aspects of this research program considered difficult to realize were:

1. Development of a transient source for broadband excitation of interesting electromagnetic geometries,

2. Development of a measurement system for real time acquisition of transient field pulses to preserve the high frequency, K_u band, information content, and

3. Development of a detailed mathematical model of the crack structure with transmit/receive antennas in close proximity.

In laboratory breadboard experiments, methods and techniques for detection and monitoring of electromagnetic leakage through small structural openings were demonstrated with good agreement between measured and calculated results.

RESEARCH BACKGROUND

Program Objectives

This research program was designed to lead to a laboratory "proof-of-principle" demonstration for the detection and monitoring of electromagnetic (EM) leakage through small structural openings in the frequency range between 8 GHz and 18 GHz. Development of experimental methods and techniques for EM leakage detection through small openings and their practical implementation in hardware were central to this research effort. The experimental work was supported by analyses of the EM field structure both within and near electrically small structural openings. A comparison of theory and measurement was made to gain an improved physical insight. In addition, the analyses were designed to delineate and identify discriminants for detection of EM leakage.

An integral part of this research was the development of methods and techniques for generating and receiving picosecond EM waveforms. The generation of these waveforms involved laser induced transient excitation of EM structures with major emphasis on broadband signal generation with minimal interference and noise contamination. Program requirements demanded experimental operation at a level equal to or exceeding the current state-of-the-art.

Acquisition of transient waveforms with preservation of high frequency content was required for successful detection and/or monitoring of EM

leakage through practical structural openings. Thus, an objective of this research was to develop a signal acquisition system capable of operating up to 18 GHz. By combination of this signal acquisition system with the appropriate signal processing techniques, the first phase of this research program was to culminate in a laboratory demonstration of improved capability in the detection/monitoring of high frequency EM leakage through very small structural openings.

Existing Technology Versus Requirements

A. Transient Sources

Time-domain metrology techniques and hardware have been developed primarily for material measurements up to approximately 16 GHz [1]. The measurement geometry consists of an elaborate repetitive transient source exciting an air-filled waveguide network with the sample located in the waveguide structure. Modern pulse generation techniques are restricted to frequencies below approximately 30 GHz with conventional hardware. In most applications of transient sources, considerable care must be accorded the EM interference problem and the radiative inefficiency of most antennas for baseband pulses. In many cases the presence of such a source can significantly alter the local EM geometry. Thus electrical interference can be detrimental to precise measurements unless proper attention is given to its control.

Utilization of ultrashort optical pulses provides several methods for generating electrical pulses having durations and amplitudes which are

unobtainable by conventional electrical techniques [2]. One method of target excitation used laser induced thermionic emission to create a transient current monopole at a point on the surface of the target. With a 1 ns duration, 1.06 micron laser pulse, target excitations with spectral content exceeding one GHz have been routinely accomplished [3,4]. Basic experiments with conducting targets demonstrate the EM equivalent of this source excitation to be a transient current monopole directed inwardly along the normal to the target surface. Recent experimental results suggest that bandwidths in the range from 6 to 10 GHz are possible with this simple technique. Excitation frequencies up to 50 GHz should be achievable with ultrashort laser pulses of 20 ps duration. Laser induced transient excitation of non-metallic targets can be realized by placing a tiny metal post in close proximity to the surface of the target without contaminating the EM geometry if direct optical illumination of the target itself is unsatisfactory.

This basic research data for designing broadband transient sources was vital to the adaptation of laser induced excitation into a practical time-domain EM source for investigation of EM leakage through structural openings.

B. Transient Measurements

1. Real-Time Continuous Measurements: The state-of-the-art for temporal resolution in electric field real-time measurements is approximately 50 ps with a sensitivity of approximately 150 mv/cm utilizing a traveling wave cathode ray tube incorporating a channel plate electron multiplier [5]. Commercially available instrumentation for real-time electric field measurements are limited to time resolutions of approximately 100 ps with sensitivities of the order of a volt per meter. This temporal resolution corresponds to a distance resolution of approximately 3 cm

which is not adequate for the purposes of this program. With commercially available transient digitizers interfaced with a computer, single transients can be acquired in real-time with harmonic content up to approximately 1.7 GHz with extensive data processing (software bandwidth extension).

2. Real-Time Sampled Measurements: Real-time electric field sampled measurement describes the acquisition of multiple samples from a single transient signal occurrence. Neither multiple sampling with a single low repetition rate sampling gate and signal replication nor multiple sampling with a single high repetition rate sampling gate have been successfully used to acquire transients in the picosecond range. Substantial work has been done using multiple amplitude discriminators, but the time resolution required in studying EM leakage through real-time measurements does not appear achievable with present hardware.

3. Equivalent-Time Measurements: Equivalent-time measurement methods require multiple occurrences of the signal to acquire the waveform. Equivalent-time sample measurements may be accomplished in three ways: (1) amplitude discrimination, (2) sequential sampling, and (3) random sampling. In the former an amplitude discriminator is biased to an amplitude reference level. When the signal value rises to the reference level, the discriminator abruptly switches state and stops a time interval meter whose start time is synchronized to the signal occurrences. The reference level and the time interval corresponds to one point on the pulse waveform. The discrimination reference level was the known part of the sampled data coordinate and the measurement provides the time coordinate. The sampled data output consists of the discrete time value corresponding to specified signal amplitude levels. One channel of data storage is required to store the signal sampled time values. In the sequential sampling mode, the time coordinate of a given sample is known and is specified through time base electronic circuits which can be designed to provide uniform (periodic) or nonuniform (aperiodic) sampling intervals, each sample being taken successively at a later time coordinate of the signal. The sampled data storage system then stores only signal amplitude information as the time of each sample is predetermined in relation to the start of the signal. In the random sampling mode, both time and amplitude data are simultaneously acquired and stored. This particular method requires two data storage channels and is a more complex system. However, the additional complexity provides for some remarkable capabilities since, in general, the method does not require any synchronization between the signal and the

sampling commands, nor does it require a signal channel delay line. For electrical pulse measurements, commercial systems using equivalent-time sequential sampling and random sampling have been used to achieve time resolution of approximately 20 ps. Thus utilization of this instrumentation in a straightforward manner to investigate EM leakage through structural openings will require the development of a reproducible, repetitively pulsed transient source with frequency content extending above 18 GHz (20 ps duration).

C. Summary

The problem of detecting and monitoring EM leakage at frequencies up to 18 GHz lies just beyond the state-of-the-art in the generation and real-time measurement of transient wavoforms. As outlined above, recent technological developments in optics and transient generation suggest reasonable approaches to the solution of these problems. Laser induced transient excitation of conducting structures provides a practical method for producing broadband EM fields with frequency content up to, and past, 20 GHz. With the construction of a high repetition rate transient source, commercially available sampling equipment would handle the measurement requirements for EM leakage detection.

With a low repetition rate transient source, the major problem confronting this research program was the development of hardware and techniques to acquire the electrical transient field with a sufficient bandwidth to preserve its informational content at frequencies up to 18 GHz.

Proposed Solution

Accomplishment of program objectives required research in the development of both transient sources and receivers. In work on a broadband, transient source, a mode-locked Nd:YAG laser would be used to irradiate one (or more) antenna structures on either side of the structural opening. This optical illumination of the antenna would induce a transient current monopole on the conducting sheet without external electrical connections. For a laser pulse width of approximately 30 ps and energy of approximately one millijoule, a broadband transient source with frequency content up to 33 GHz should be achievable. A mode-locked laser with this energy specification can operate at a repetition rate of 10 Hz. This laser induced transient excitation would be used as a tool for the investigation of EM leakage through structural openings.

In response to the need for improved transient acquisition capability, research on an ultra-fast single transient acquisition device was conducted. This device was designed to consist of an array of optically controlled switches arranged in a carefully designed transmission line geometry with extreme care given to impedance matching and minimal pulse waveform distortion. The purpose of this research was to fabricate a single transient sampler with effective bandwidth capabilities to approximately 20 GHz.

An ultrafast single transient acquisition device would use optically

sensitive photoconductive switches. Candidate materials for the photoconductive switches include amorphous silicon [6], amorphous gallium antimonide, gallium arsenide[7], indium phosphide [8], and cadmium selenide [9]. After evaluation of the switching speeds, optical efficiency, and the ratio of switch resistance under optical irradiation relative to dark resistance, the best material would be fabricated in a strip-line transmission geometry for characterization as an ultra-fast sampler.

In this first phase of research, the best available components would be integrated into an automated instrumentation system to demonstrate "proof-of-principle" experiments for the detection and monitoring of EM radiation leakage through small structural openings.

PROCEDURE

The overall strategy of this program was to develop a system to detect the presence of a crack in a perfectly conducting ground plane. An imposed constraint that all measurement hardware be located on the interior side of the geometry (the side which had the electromagnetic source which might be leaking to the exterior side) was observed. This research issue was approached by first collecting as much empirical and analytical data concerning electromagnetic radiation in and near narrow slits as possible. This compilation of data was performed to find a method or methods for predicting changes in crack geometry from changes in measured electromagnetic field strengths. Because it was known from the start of the program that this research would be near the boundaries of several technological limitations, somewhat parallel research initiatives were implemented concurrently on several facets of this problem.

This section of the report summarizes the approaches used in addressing the technical issues of this research program. Four topics are highlighted; one is theoretical, the others are experimental. The theoretical topic is the investigation of electromagnetic field structures in narrow cracks. Only the method of approach is outlined in this section of the report but a detailed derivation is given in Appendix A. In the discussion of the three experimental topics, electromagnetic instrumentation, waveform processing, and proof-of-principle experiments, the laboratory approaches are

identified. Some findings, by way of examples of measured results are given in this section but the significant findings are given in the next section of this report.

Electromagnetic Field Structure Analysis

An effort was initiated at the start of this program to examine theoretical electromagnetic field behavior in and near a narrow slit. The method to be employed should 1) be applicable over a wide frequency band (d.c. to 18 GHz), 2) allow application to a slit in a ground plane of finite thickness, 3) allow transmitting and receiving monopoles to be placed on the surface in the vicinity of the slit, and 4) be amenable to frequency and time-domain examination. The second requirement was important because most theoretical approaches apply to ground planes with zero thickness; the third was important because the customary incident plane-wave approach could not be used. The approach taken combined two well-known theoretical electromagnetic techniques: the integration of a spectrum of traveling waves to model a point source, and a transmission line model for the interaction with the slit. These two methods used together allowed a solution which satisfied the four conditions stated above.

Figure 2 shows the basic geometry to be modeled. A transmitting antenna was placed a distance "a" from an infinitely long crack in a ground plane with finite thickness. A receiving antenna was placed a distance "b" from the crack on the other half-plane (the two antennas can be on

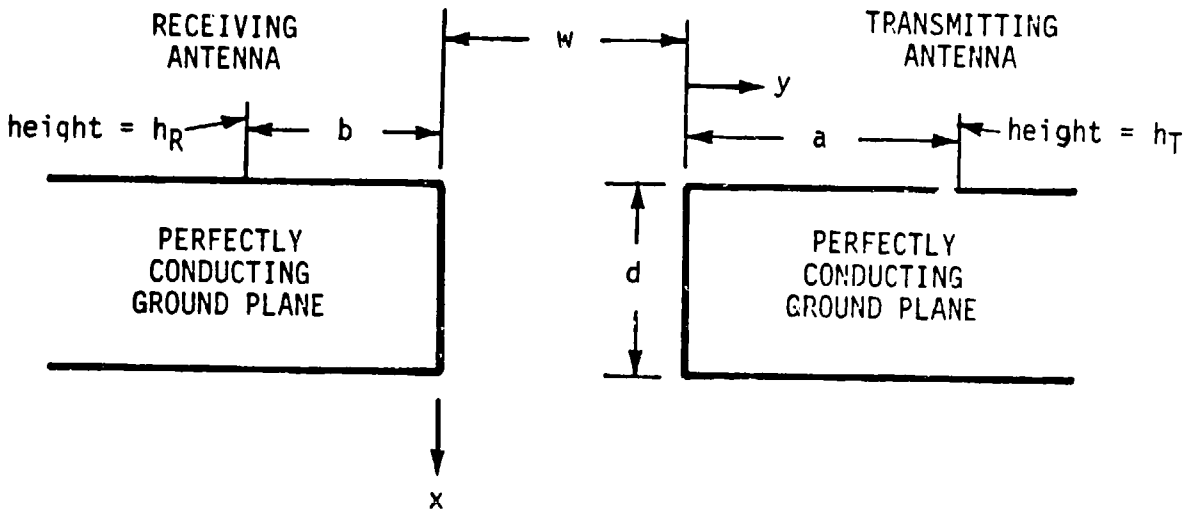

FIGURE 2. NARROW SLIT GEOMETRY

the same side of the slit or on opposite sides of the ground plane). The slit had width "w" and the ground plane thickness was "d". This structure was immersed in an infinite medium with permittivity and permeability of free space. The antenna dimensions were variable as shown.

Modeling of the crack was accomplished using the method presented by Harrington and Auckland in their 1980 paper "Electromagnetic Transmission Through Narrow Slots in Thick Conducting Screens" [9]. The approach given in this paper, which considers only plane-wave incidence, starts by matching all the fields in the apertures and using a moment method technique to match all required boundary conditions. The field equations presented in the paper are simplified by specializing them to narrow slots, which forces all TM modes to be cut off. This specialization will make the solution valid only for narrow slots. The magnetic field is now constant in the crack and polarized parallel to the crack. The resulting scalar equations which must be solved are analogous to the familiar transmission line equations.

The restriction of Harrington and Auckland's analysis to plane-wave incidence on the slit must be overcome to address geometries relevant to this research such as short monopole antennas in the vicinity of the slit. The case of ground plane mounted transmit and receive monopoles with a narrow slit in their near fields is a very complex three-dimensional problem. However, this three-dimensional geometry can be simplified to a series of two-dimensional problems by expressing the

effect of the transmitting antenna as a continuous spectrum of traveling wave sources as depicted in Figure 3. The line source was placed a distance "a" from the slit (as was the transmitting antenna) and was polarized in the direction orthogonal to the ground plane. Figure 3 shows the two fundamental reasons for employing this type of source. First, the source itself is in the near-field of the slit so effects of waves that are not planar can be studied. Second, with the line source parallel to the crack there is no variation in the z-direction; the original three-dimensional problem has been reduced to a two-dimensional problem. In fact, the line source did have periodic variation in the z-direction, i.e. $\exp(j\beta z)$ variation, but this variation was treated algebraically in the same manner as the time phasor factor, $\exp(j\omega t)$, is treated in classical electrical engineering theory.

It was necessary for there to be a method of transforming from the traveling wave line source to the short monopole. The procedure used was completely analogous to Fourier Tranform techniques in circuit theory where the response of a given circuit to a short pulse may be desired. The response as a function of frequency (for all frequencies) would first be calculated, then an integration would be performed along the frequency axis, with the desired weighting (or Fourier coefficients) to find the time response to the proposed short input pulse. In the present problem, this transformation was accomplished by a spatial Fourier Transform technique. Contributions from a spectrum of traveling wave line sources with different propagation constants were summed in the proper manner to model a single monopole. The line source had

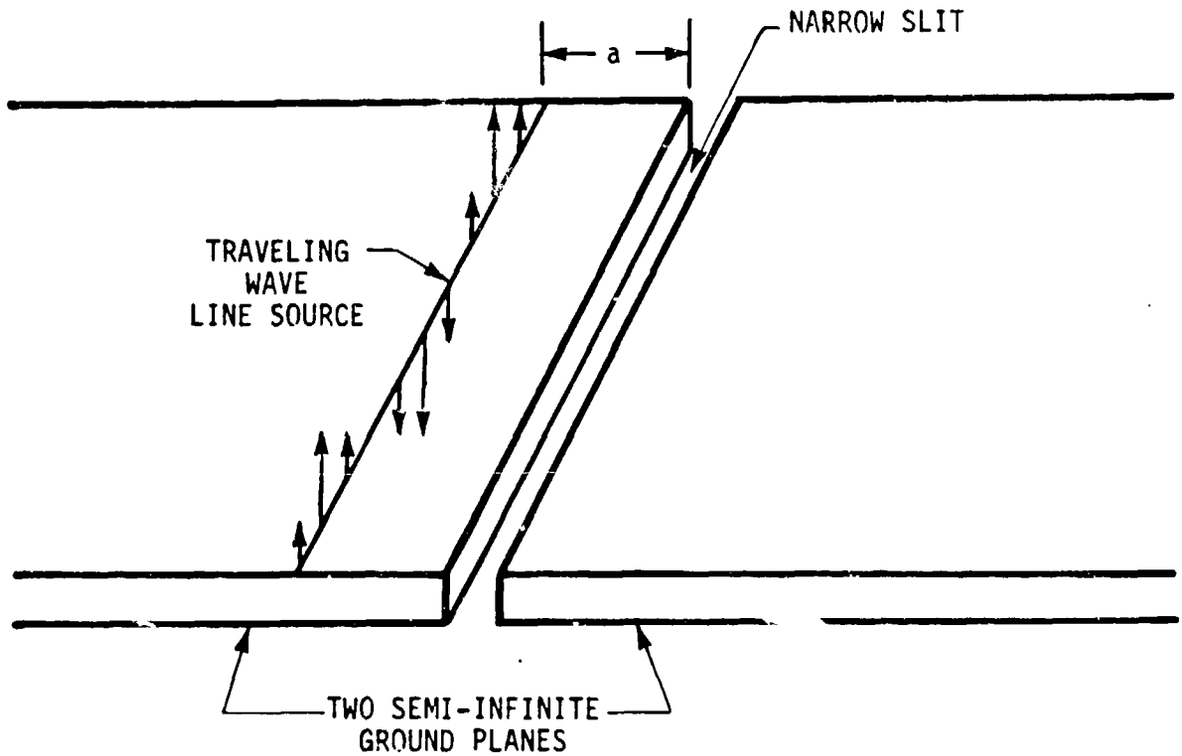

FIGURE 3. TRAVELING WAVE SOURCE GEOMETRY

propagation constant β, which became the variable of integration when it was appropriate to change from the traveling wave line source to a single thin source with current flowing orthogonal to the ground plane.

Conceptually, the method was the following: the entire derivation performed by Harrington and Auckland was followed but with the incident field being caused by a traveling wave source with propagation constant β, rather than by a plane-wave. Mathematical relations analogous to those in Harrington and Auckland's paper were found. For example, the sine and cosine functions used in the transmission line equations were replaced by the corresponding hyperbolic sine or cosine. The incident fields were written with Hankel or modified Bessel function behavior rather than with plane wave behavior. Once these relationships (which were all functions of the traveling wave propagation constant, β) were found, an integration was performed along β in the manner required to force the traveling wave sources to appear as a single vertical monopole. The final result was the electric field at some test point in or near the crack due to an infinitesimally small current monopole on the surface of the ground plane in the vicinity of the crack.

The mathematically complex part of the above operation was the integration along β, specifically when β was equal to the free space propagation constant, k, the radian frequency divided by the free space propagation velocity. At that point on the β axis, a singularity existed which had to be handled mathematically in the standard fashion [10]. Appendix A contains the derivation for the electric field and an

explanation of the integration along β including the handling of the singularity.

One more step was required in the modeling of the actual physical geometry. When the above steps were completed the source was a small current element rather than an actual antenna with finite length. Two approaches were followed. First, a simple circuit model was used but it was found to be lacking in accuracy at high frequency. Second, a moment method program was used to generate the input impedances for short monopoles over the range of frequencies of interest.

A method was found, however, for testing the accuracy of the model and the implemented computer code which was independent of the antennas. The results confirming the validity of the approach are given in the Findings section of this report.

A second moment method program was written to model the effects of the finite length of the transmit and receive antennas. The only assumption about the antennas was a large length to diameter ratio. The results of this program served as a check for experimental measurements. They were also used to generate input impedance parameters to allow finite length antennas to replace the infinitesimal monopoles used in the program that models the finite thickness ground plane effects. This program was able to accurately predict these input impedance parameters. Additionally, the program was able to predict the voltage transfer characteristics between two monopoles mounted in a ground plane. The Findings section

of this report contains the comparison between measured and calculated data.

The moment method program is being expanded to include the effects of the slit in the ground plane and to also include the time response between the transmit and receive antenna. However, the model will be limited to an infinitesimally thin ground plane. This latter restriction is necessary because the numerical calculations become too intensive in time and computer memory when the ground plane has finite thickness. This restriction may not be a serious limitation for simple crack structure where the ground plane is electrically thin.

A theoretical study was conducted which considered transient radiation over a ground plane. It gave excellent insight into the phenomena which could be expected. One concern, which this analysis brought to light, was an expected low signal to noise ratio caused by geometrical radiation loss between two ground plane mounted monopole antennas. Both have isotropic radiation patterns azimuthally and sine patterns in elevation. One way of overcoming this problem was to place a second ground plane above the ground plane which held the antennas and contained the narrow slit. The geometrical losses due to radiation away from the primary ground plane would be greatly reduced. This arrangement was used in initial studies to facilitate meaningful data acquisition. This analysis, which was critical in giving pre-experimental insight into the electromagnetic geometry, is included as Appendix C of this report.

Electromagnetic Instrumentation

In the laboratory many different techniques were explored for their applicability to the present problem. As originally conceived, a high-power, short duration laser pulse would be used to excite a very short (in space and time) monopole of current which contained a very rich spectral content in the range between 8 GHz and 18 GHz. A laser capable of exciting this monopole was purchased, the phenomenon was realized, and meaningful measurements were made. As the research program progressed, however, other techniques were pursued in order to allow the compilation of information from other approaches. The laser approach allowed investigation of the problem in the time-domain, and utilization of available network analysis equipment permitted alternative frequency-domain measurements to be made. This portion of the report, therefore, separates laboratory instrumentation according to whether its primary function was in the time-domain or frequency-domain.

Time-Domain Instrumentation

The laser used to generate the short electromagnetic pulse on a conducting target was a Quantel Nd:YAG mode-locked laser (wavelength 1.06 microns) with an output pulse of 30 picoseconds duration and 60 mJ energy at a 10 Hz repetition rate. Initially, the instrument which read the output signal from the receive antenna was a Tektronix 7912AD Transient Digitizer. This instrument was used because of its ability to capture and digitize a single shot event in the time-domain. Its

limitation, in the context of the present program, was its inherent bandwidth of 1 GHz. The 7912 was capable of capturing the output pulse but it could not resolve the rise-times associated with the input pulse generated by the laser induced microwave excitation. There is currently no commercially available instrument capable of performing this task. Therefore, this research program required the design, implementation, and testing of a single-shot transient sampling device capable of capturing the inherent rise time of the laser pulse and therefore information in the frequency-domain to 18 GHz.

A functional block diagram of the single-shot sampler which was designed during this program is shown in Figure 4. This sampler would convert the spatial resolution of a signal propagating along a transmission line (as shown in the upper left of Figure 4) into the time-domain (as shown in the lower right part of Figure 4) by strobing the sampling photoconductive switches at the same instant in time with an ultra short laser pulse. The optical paths from the laser to each switch would be matched to insure that all switches were engaged simultaneously. Each sampling unit would then record the signal voltage on the line at its respective position. A charge, which was proportional to the voltage, would be stored on a capacitor which was buffered by a high impedance, low bias amplifier. The photoconductive switch would trap the charge on the capacitor by returning to a high impedance after the light pulse is off. The buffer amplifier, therfore, could be a low bandwidth device without limiting the sampler bandwidth. The net result would be N recorded points of a waveform where each point was separated by a

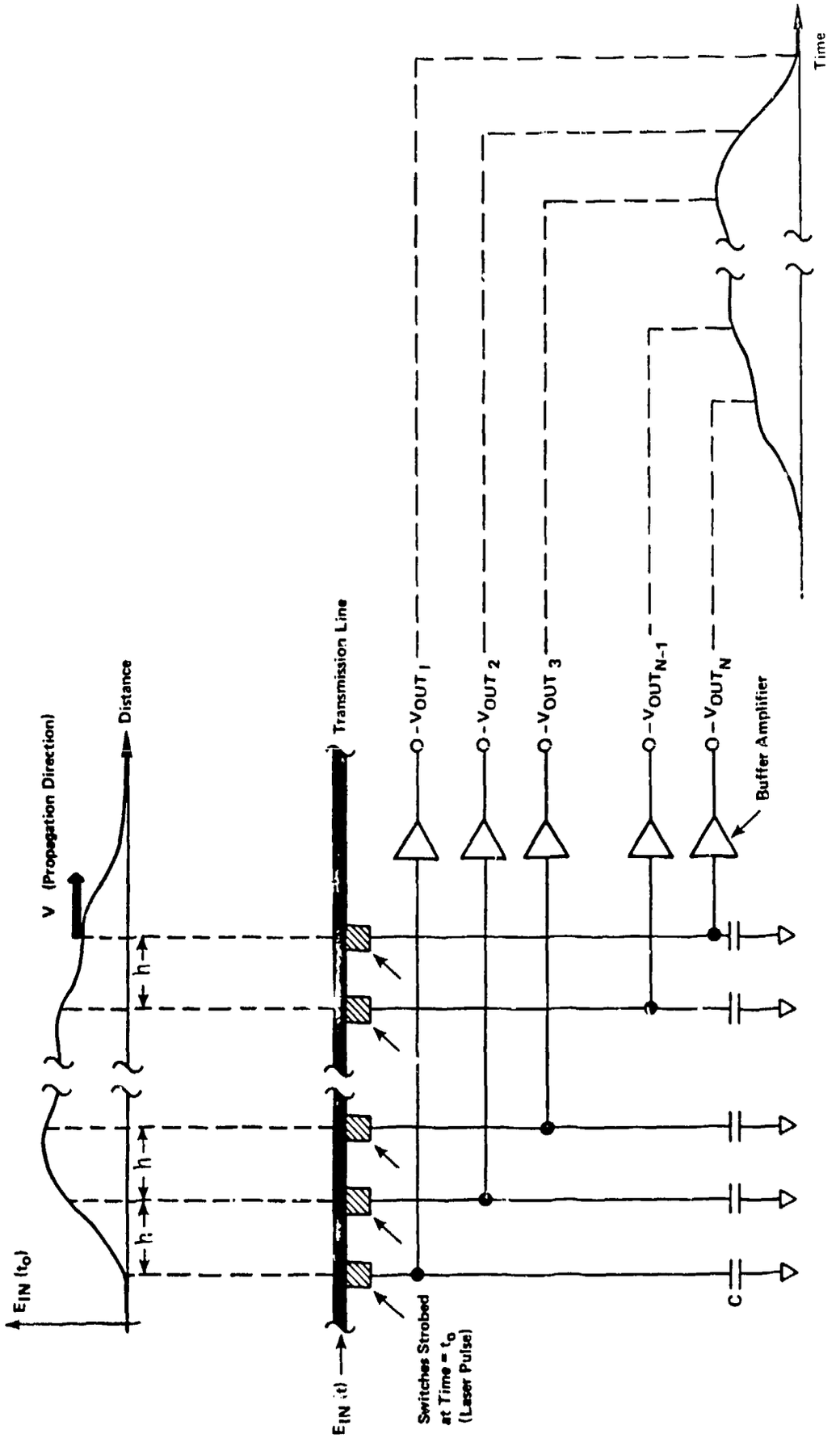

FIGURE 4. HIGH FREQUENCY SAMPLER

uniform distance h. This operation is equivalent to sampling a waveform every t seconds, where,

$t = h/v$ [seconds]

h = distance [meters]

v = velocity of propagation [meters/second].

This procedure can best be visualized by refering to Figure 4. A "picture" of the waveform at an instant in time would be recorded when a waveform was sampled at every h meters along the transmission line. The spatial distribution of a signal would then be converted to the time-domain. A more detailed analysis of this single-shot transient sampler design appears as Appenix D of this report. Reference information on transient behavior of transmission lines is also included as Appendix E.

The effective time between samples would be inversely proportional to the propagation velocity and directly proportional to the spacing between the sampler switches. The propagation velocity is dependent upon the transmission line geometry and material. While propagation characteristics do not change in time, dispersion can lead to pulse distortion on the transmission line. The effective time between samples can therefore be considered a function of the spacing between the sampling switches. By placing these switches very close together it would be possible to obtain samples of a single transient waveform separated in time by intervals only slightly exceeding the switching

(sampling) time. This fast sampling rate for nonrepetitive waveforms would be a significant improvement over currently available hardware.

The dispersion of the transmission line can cause significant errors when dealing with large bandwidths because of signal distortion as it propagates down the line. The sampling switches at the end of the line would see a distorted version of the signal which appeared at the first sampling switch. However, these errors can be corrected by characterizing the transmission line as a function of frequency and using this data to correct for the effects of the dispersion, i.e., deconvolution of the impulse response of the line with the measured signal waveform.

Although the design for the transient sampler went through several iterations the critical components were the ultra-fast optically strobed switches. The parameters of interest included switching speed, optical sensitivity, and ratio of the resistance of the switch when turned off (off resistance) to the resistance when illuminated by light (on resistance). A fast switching speed is necessary to allow high frequency sampling. The optical sensitivity is necessary because many switches must be enabled at the same instant of time and it is envisioned that one laser would excite all of them by way of optical fibers, one fiber per switch. The ratio of the "off-resistance" to the "on-resistance" must be high so maximum energy can be coupled through the switch when it is "on" and that a minimum amount of charge will leak back through the switch when it is no longer being illuminated. In the

laboratory, only the switching times were measured quantitatively. The optical sensitivities and resistance ratios were measured only qualitatively. For example, it was found that a single amorphous silicon (a-Si) switch required 30 percent of the laser power to function. This insensitivity would not allow the existing laser to drive a sufficient number of switches to implement a practical sampler. The "off-resistance" could be measured easily at d.c. but the on resistance, when the switch is enabled for only 30 picoseconds, has not been measured.

The test geometry for measurment of switch speeds is shown in Figure 5. The receiving instrument was a Tektronix 7S12 TDR/Sampler plug-in under the control of a Tektronix 7854 digitizing oscilloscope. Using a Tektronix S-53 Trigger Recognizer and an S-4 Sampling Head in the 7S12, time-domain measurements with frequency content up to 14 GHz (which is the nominal 3 dB bandwidth of the sampling equipment) were made in the repetitive sampling mode. A fixed d.c. bias was put on one terminal of the switch and the laser illuminated the gap for 30 picoseconds at a 10 Hz repetition rate. (The delay depicted in the laser path is explained below.) The output channel was a 50 ohm impedance system connected to the repetitive sampler. After sufficient signal processing the sampled signal was sent to a Tektronix 4052 Computer and plotted as shown in Figure 6.

In the investigation of EM leakage through a small structural opening, the laser was used to provide a transient pulse for propagation in the

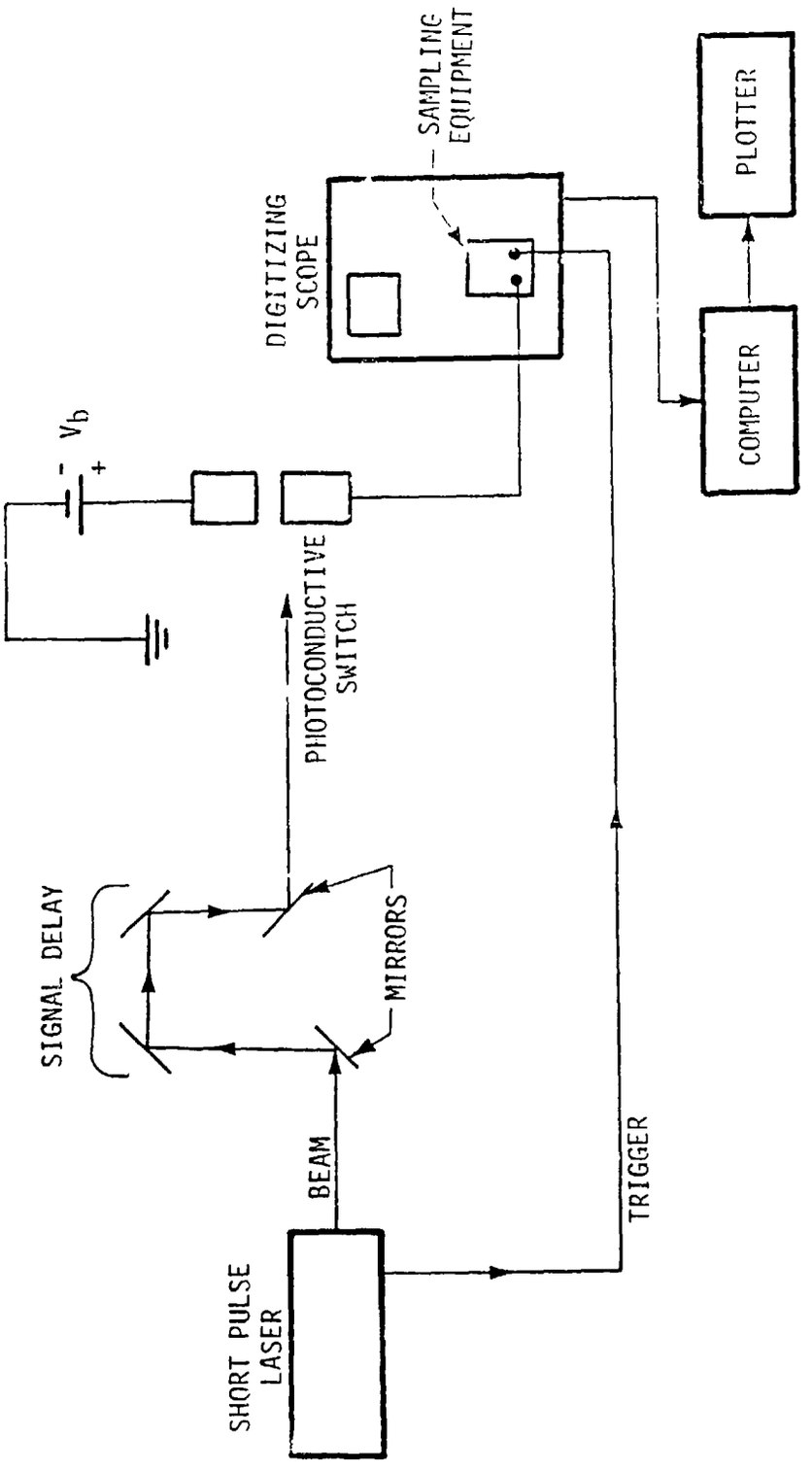

FIGURE 5. TEST GEOMETRY FOR SWITCH SPEED MEASUREMENT

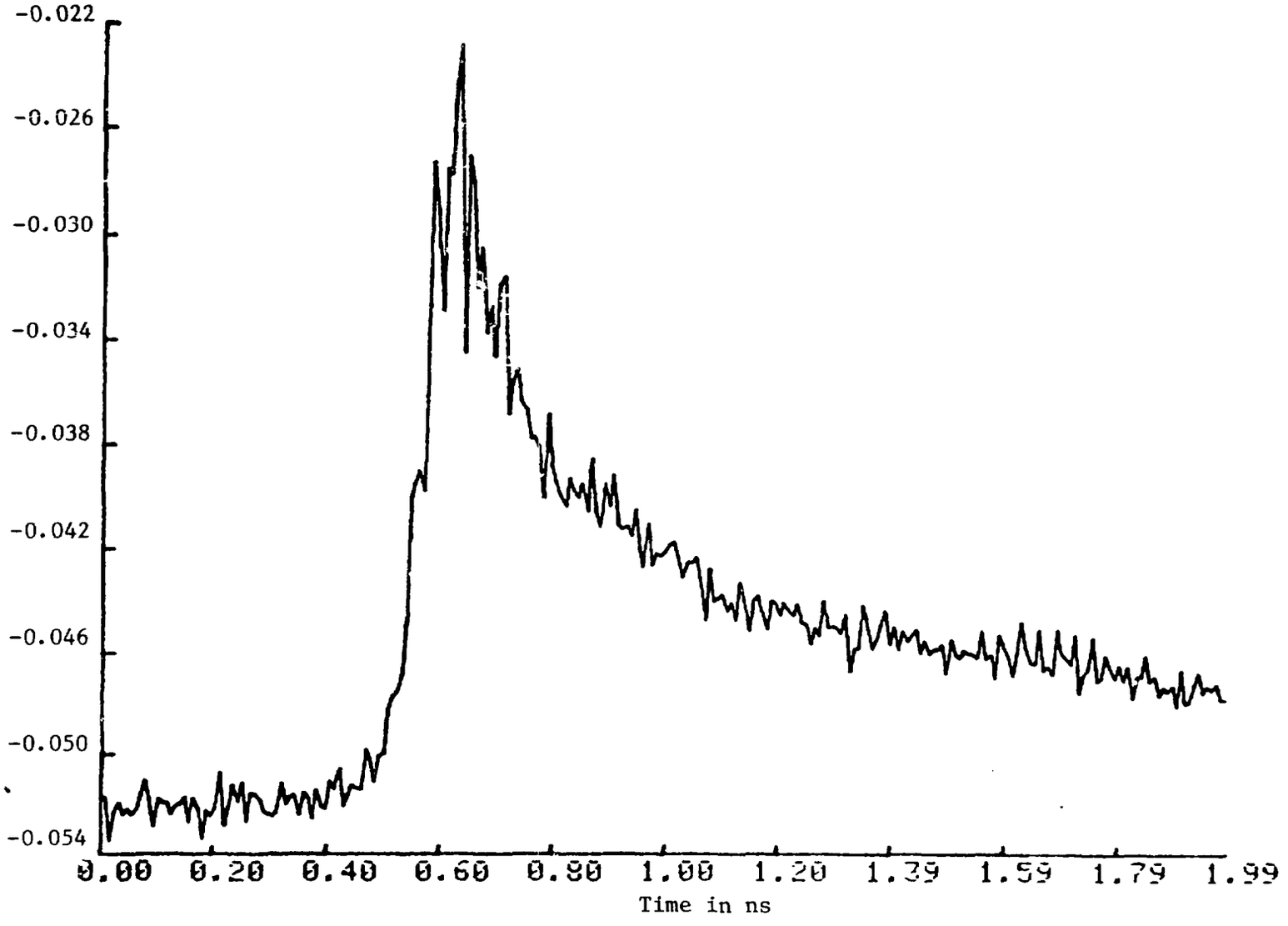

FIGURE 6. EXAMPLE OUTPUT OF A SWITCH SPEED MEASUREMENT

vicinity of the crack. The geometry for the microwave measurements with a gap or crack in the ground plane is shown in Figure 7. The instrumentation used was the same as employed in the switch speed measurement. The laser illuminated, with a focused beam, the tip of a short monopole near the crack. Radiation traveled across the crack to a receiving antenna which was connected to the sampling instrumentation. Generally, the illuminated antenna was inside a vacuum. The elimination of nitrogen near the monopole tip allowed the electrons flowing off the antenna to have a longer mean free path length and therefore yield a stronger microwave signal.

No focusing of the beam or vacuum was necessary during the switch measurements. These measurements required only incident light for strobing and not as high a concentration of energy as necessary for the microwave emission.

The delay in the laser path depicted in Figures 5 and 7 was necessitated by a requirement of the Tektronix sampling hardware. The 7S12 requires the trigger pulse to arrive at the front end of the sampler 75 nanoseconds (ns) before the signal to be measured arrives. The trigger signal was taken directly from the laser and fed into the trigger recognizer. Two options were available to implement the delay in the signal path. One option involved attaching a coaxial cable which was long enough to add the 75 ns delay between the receive antenna and the sampling equipment. This option was not viable because the high frequency losses in the cable would greatly distort the waveform. The

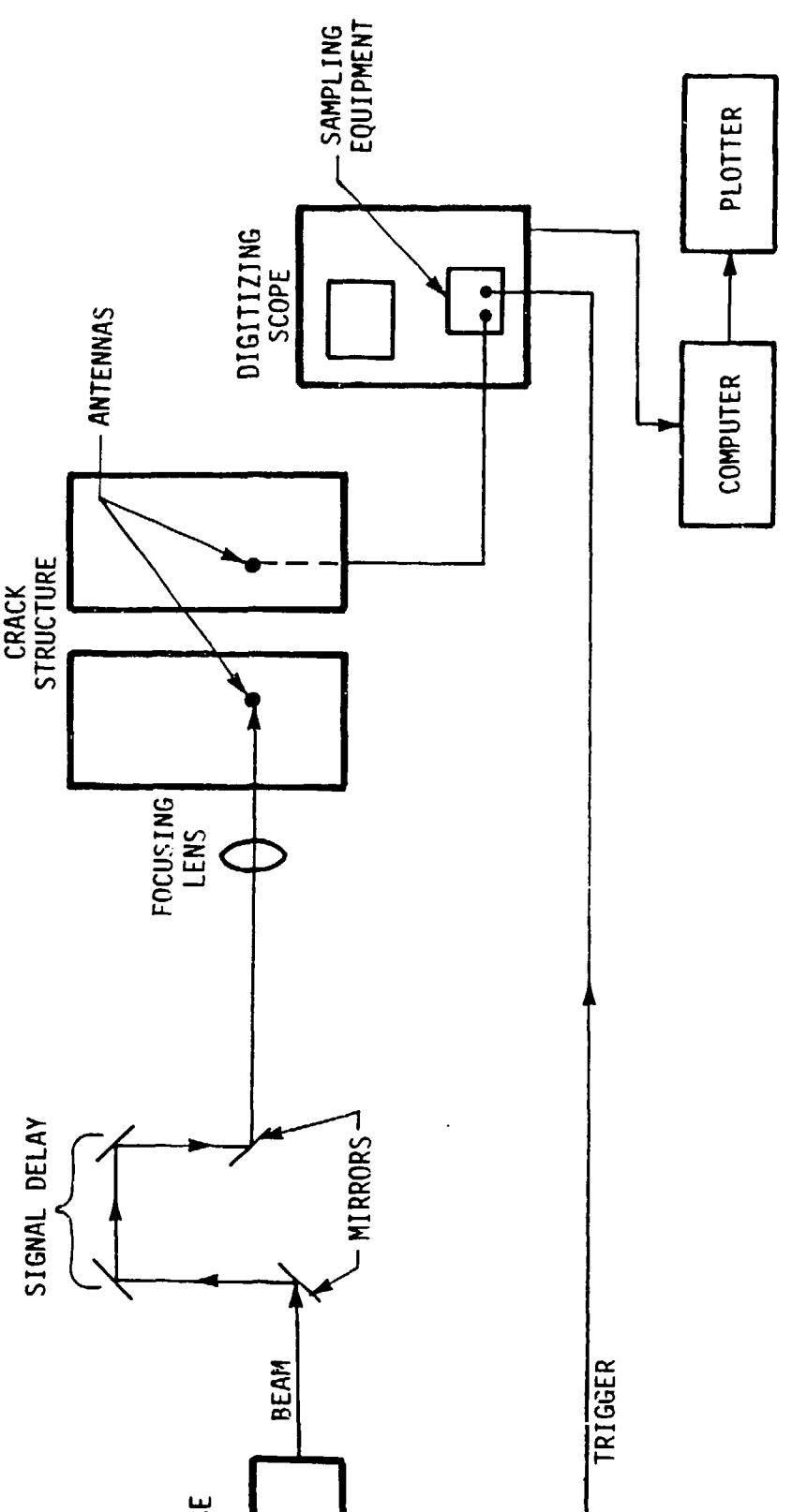

FIGURE 7. TEST GEOMETRY FOR LASER INDUCED MICROWAVE EXCITATION OF CRACK STRUCTURE

other option immediately available was to increase the path length of the laser pulse leaving the laser and striking the target. This additional delay was implemented by bouncing the laser beam between mirrors enough times to create the desired signal delay. The beam intensity was decreased somewhat because of reflection losses and beam divergence but sufficient energy still reached the switch or the target (whichever was being measured) to allow meaningful measurements.

The Tektronix sampling equipment was extremely useful to this program but its application has major limitations when it is employed in conjunction with the short-pulse laser. The problem centered on the requirement of the sampling equipment for a large number of repetitive inputs, each of which should be identical. The microwave measurements with the laser have three disadvantages with regard to this requirement; the laser pulse amplitude stability is worse than 5 percent, the plasma formed when the laser excites the tip of the antenna varies from shot to shot, and the laser has a very slow repetition rate of 10 Hz. The two instabilities caused by laser variation and plasma variation introduce noise in the measured waveform. This noise could be reduced greatly through signal processing by way of averaging many waveforms, but the low repetition rate of the laser rendered this solution impractical because it was time consuming. For example, the time required to take 200 waveforms with 512 points per waveform (with averaging to increase signal to noise) would take 2.8 hours with the 10 Hz repetition rate of the laser. Long term instability problems such as target movement or long term laser degradation could become more important factors.

Because of the advantages of taking the measurements in the time-domain an alternate short pulse source, which did not have the instability problems of the laser, was used. An avalanche diode pulser from Avtech (Model AVH-S-1-C-N) was connected directly to the antenna which had been illuminated by the laser. The output from the receive antenna was connected to the sampling equipment as with the laser experiments. This solid state pulser had a much better amplitude stability than the laser. (less than 1 percent variation), no plasma was formed, and the 10 kHz repetition rate allowed faster data acquisition and processing. The averaging of 200 waveforms referred to in the above paragraph would take less than 3 minutes. Data generated by this pulser was extremely useful in the analysis of geometry changes of the test structure. A disadvantage of the pulser with respect to the laser is the pulser's requirement of a direct electrical connection on the target being excited. This requirement also implies that when it is desired to move the transmit antenna to a different location, a new hole must be created and the proper connections made. The laser excites the short monopole while isolated electrically from the target of interest. This isolation simplifies geometrical changes.

Waveform processing in these time-domain experiments was done mostly in the form of averaging on a point by point basis in the Tektronix 7854 Digitizing Oscilloscope. The actual signal to noise improvement cannot be quantified because of the nature of the algorithms used in this oscilloscope. As stated above, the low repetition rate of the laser made averaging over a large number of waveforms impractical but

improvement was seen when five to ten waveforms were averaged. When the pulser was used as the excitation source, 200 waveforms could be averaged. The effect of the averaging was displayed in real time on the oscilloscope to allow observation of when further data averaging was unnecessary. Another form of signal processing used with the laser experiments involved filtering in the frequency-domain. The data were taken in the time-domain and transferred to the computer where it was transformed to the frequency-domain using a Fast Fourier Transform (FFT) algorithm. The high frequency components were truncated and the data were inverse transformed (IFT) back to the time-domain. The effect was to filter out the high frequency noise. An example of this process is given in Figure 8. Figure 8(a) shows a raw time waveform. Figure 8(b) shows the plot of the FFT result. Frequencies higher than 10.5 GHz were set to zero and the IFT was performed with the result shown as Figure 8(c).

Frequency-Domain Instrumentation

Frequency-domain measurements were made directly with a Hewlett-Packard 8410B Network Analyzer system under computer control. The microwave source was a Hewlett-Packard 8350A Sweep Oscillator with an HP 83592A 0.01-20 GHz RF plug-in. The other essential parts of the system were an 8411A Harmonic Frequency Converter and an 8743B Reflection and Transmission Test Set. The network analyzer operated in two modes. One mode displayed the results of a real time sweep through a given frequency range on an 8412B Phase-Magnitude Display; the other mode

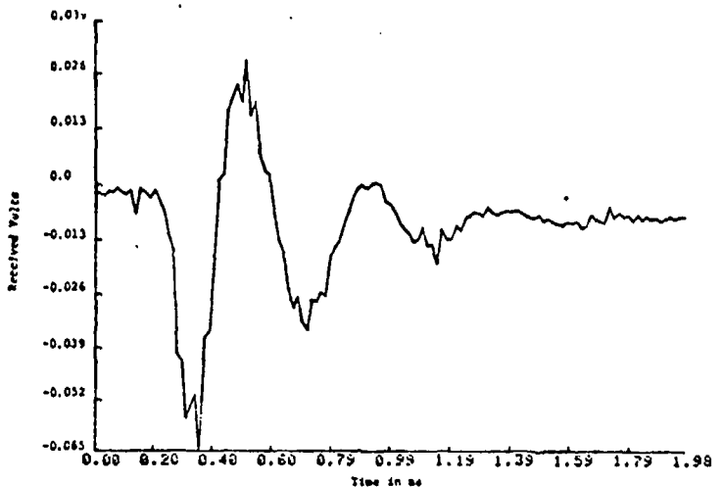

FIGURE 8a. EXAMPLE OF SIGNAL PROCESSING WITH RAW WAVEFORM

FAST FOURIER TRANSFORM (FFT)

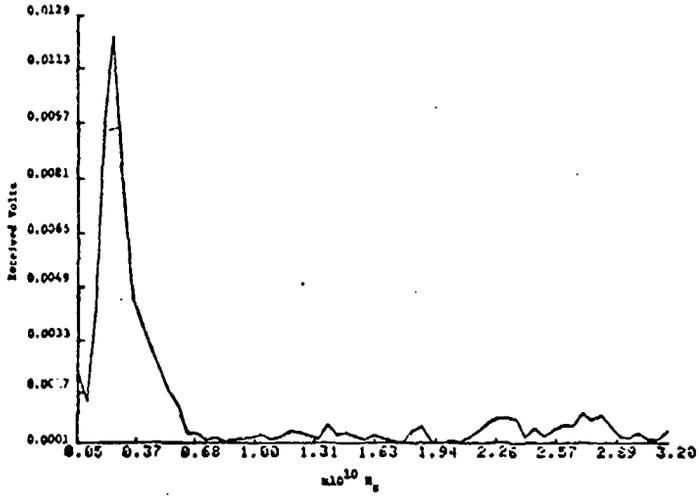

FIGURE 8b. EXAMPLE OF SIGNAL PROCESSING WITH FAST FOURIER TRANSFORM

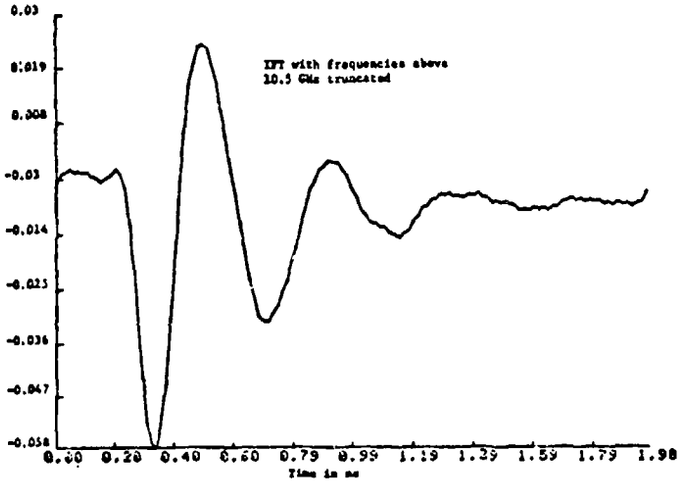

FIGURE 8c. EXAMPLE OF SIGNAL PROCESSING WITH INVERSE FOURIER TRANSFORM TRUNCATED ABOVE 10.5 GHz.

involved computer control of the sweeping source with the result sent to the computer for processing and display.

The transmitting antenna was connected to the "unknown" port of the test set and the receiving antenna was connected to the "transmission return" port. The network analyzer by its nature calibrated out changes in power levels in the source. In general, however, calibration was performed in the computer. A typical measurement is depicted in Figure 9 where, for a given crack width, a swept frequency data set (2 to 18 GHz) was acquired with conducting tape over the crack (to simulate the "no-crack" situation). The tape was then removed and another data set was taken. The computer would then divide the "no-crack" voltage value at each frequency by the corresponding "crack" voltage value and plot the result in dB. A typical output curve is shown in Figure 10. The "no-crack" value can be thought of as the incident field, i.e., the field which would occur if no crack were present. With the tape removed the total field (incident plus scattered) is measured. The division of these two values gives an indication of the behavior of the scattered field with factors such as the antennas and cables normalized out. The scattered field was so many dB below the incident field that any attempt to subtract the incident field from the total field was in vain. The result appeared as noise because the resolution of the measurement equipment was exceeded. The division of the two quantities normalized out the noise sources common to both measurements so that accurate, repeatable measurements were obtained. These measurements were also easily comparable to the results of the calculated theoretical values

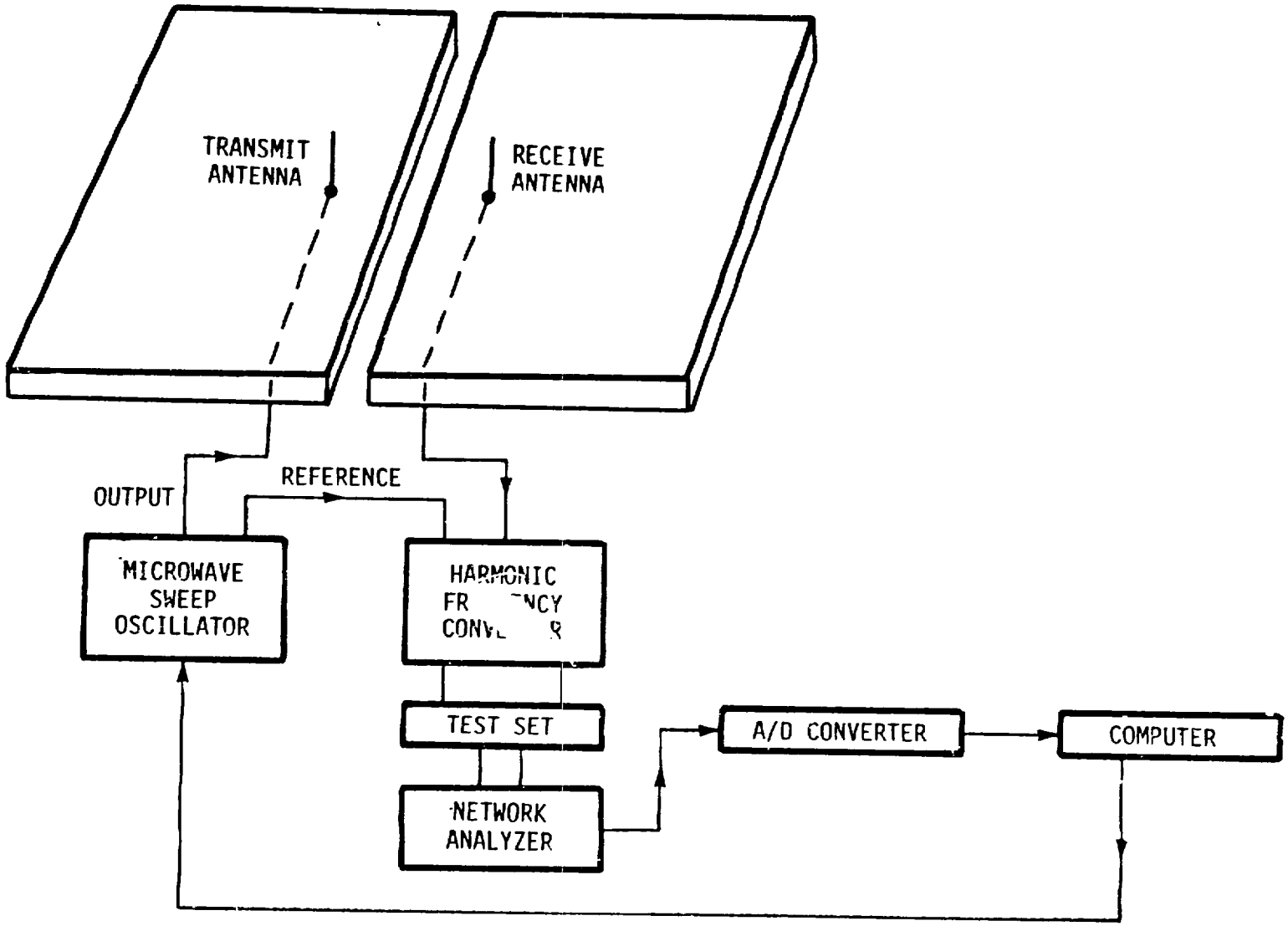

FIGURE 9. TEST GEOMETRY AND INSTRUMENTATION FOR FREQUENCY-DOMAIN TRANSMISSION MEASUREMENTS

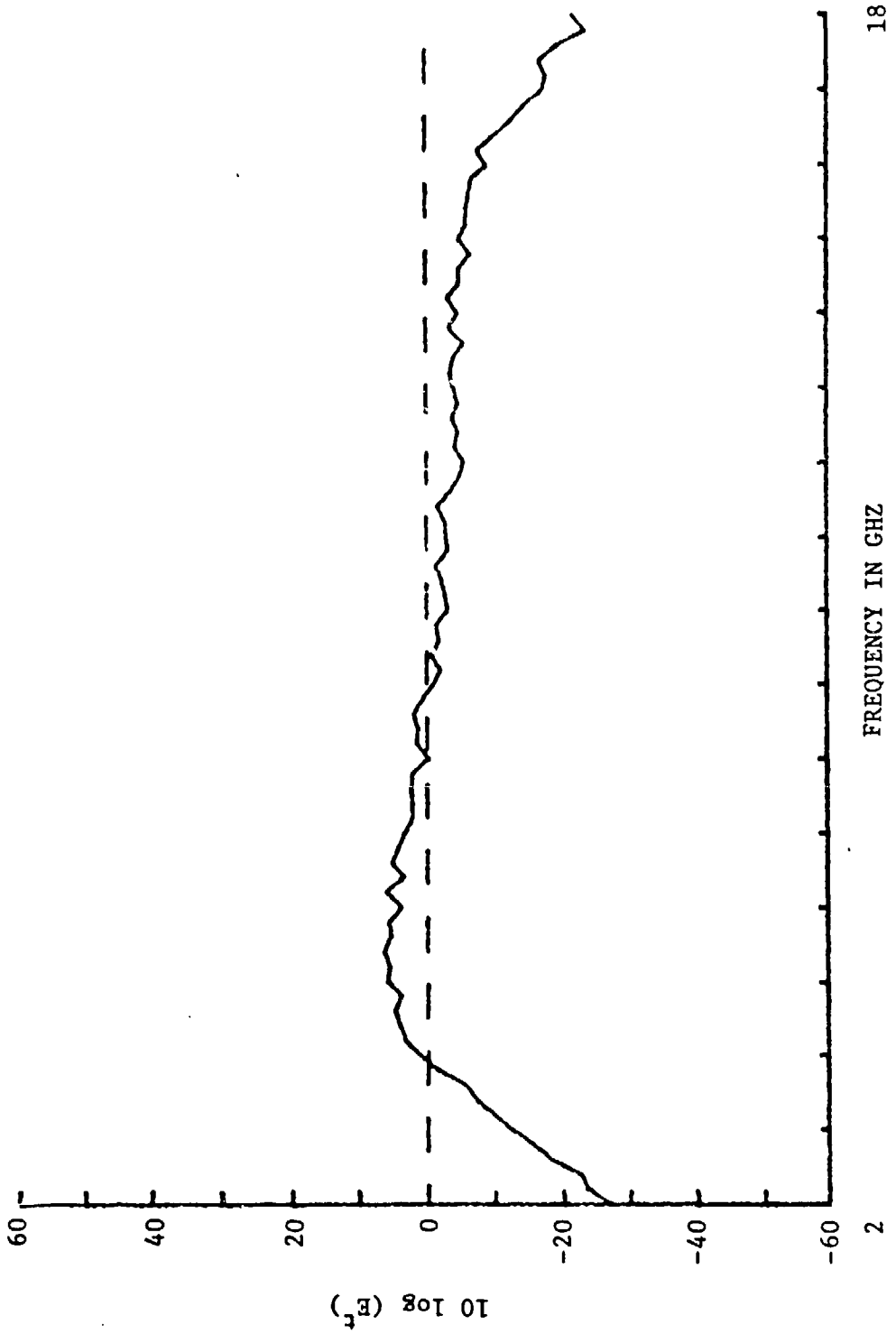

FIGURE 10. TYPICAL OUTPUT CURVE FROM THE NETWORK ANALYZER SYSTEM

discussed above. These comparisons are contained in the findings section of this report.

An example of this normalization procedure is shown in Figure 11. Figure 11(a) shows the incident field, i.e., the field measured with the conducting tape on the crack, "no-crack". Figure 11(b) shows the total field, the field acquired with the tape removed and the crack exposed. All other geometrical aspects were identical. Figure 11(c) shows the incident field divided by the total field, plotted in dB. The appearance of resonance is due to the thickness of the ground plane but its behavior is a function of the crack width.

Optical Switch Design And Fabrication

The optically sensitive photoconductive switches were needed for the fabrication of an ultra-fast single shot transient sampler. The switch was fabricated by depositing a photoconductive switching semiconductor material on a glass substrate. Next, a layer of conducting metal was deposited on the semiconductor and finally this metal was etched to form the contacts of the switch. The semiconductor materials used to fabricate switches were: amorphous silicon (a-Si), gallium antimonide (GaSb), chromium doped gallium arsenide (GaAs) and iron doped indium phosphide. The basic switch configuration is shown in Figure 12. Channel widths between 10 microns and 150 microns were used.

The a-Si and GaSb materials were used to fabricate switches in a similar

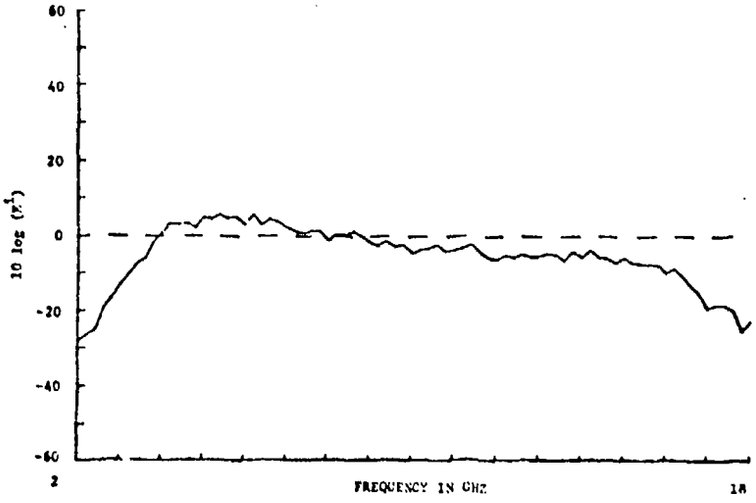

FIGURE 11a. EXAMPLE OF FREQUENCY DOMAIN NORMALIZATION PROCEDURE WITH THE INCIDENT FIELD (NO CRACK PRESENT)

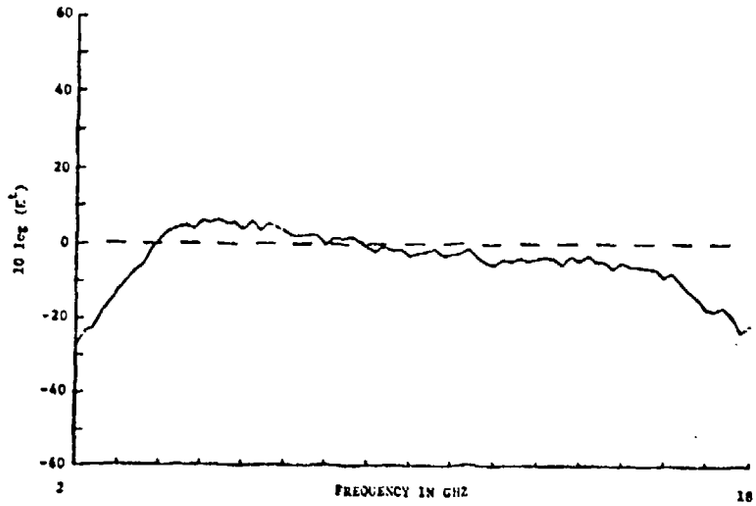

FIGURE 11b. EXAMPLE OF FREQUENCY DOMAIN NORMALIZATION PROCEDURE WITH THE TOTAL FIELD (CRACK PRESENT)

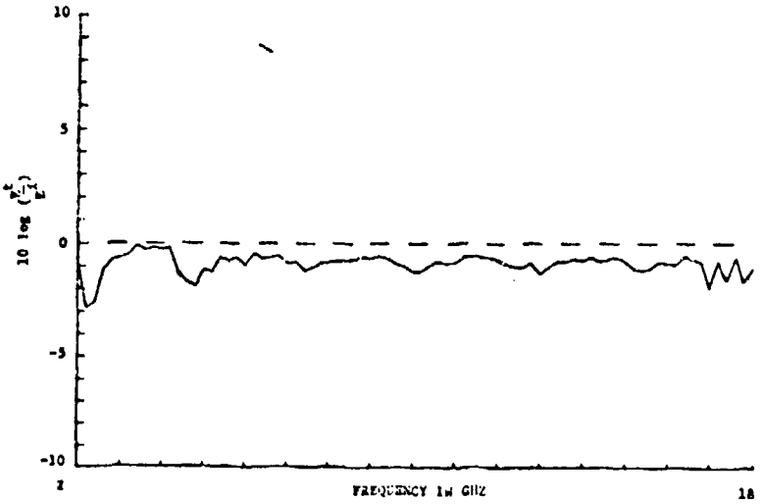

FIGURE 11c. EXAMPLE OF FREQUENCY DOMAIN NORMALIZATION PROCEDURE WITH INCIDENT FIELD DIVIDED BY THE TOTAL FIELD PLOTTED IN dB

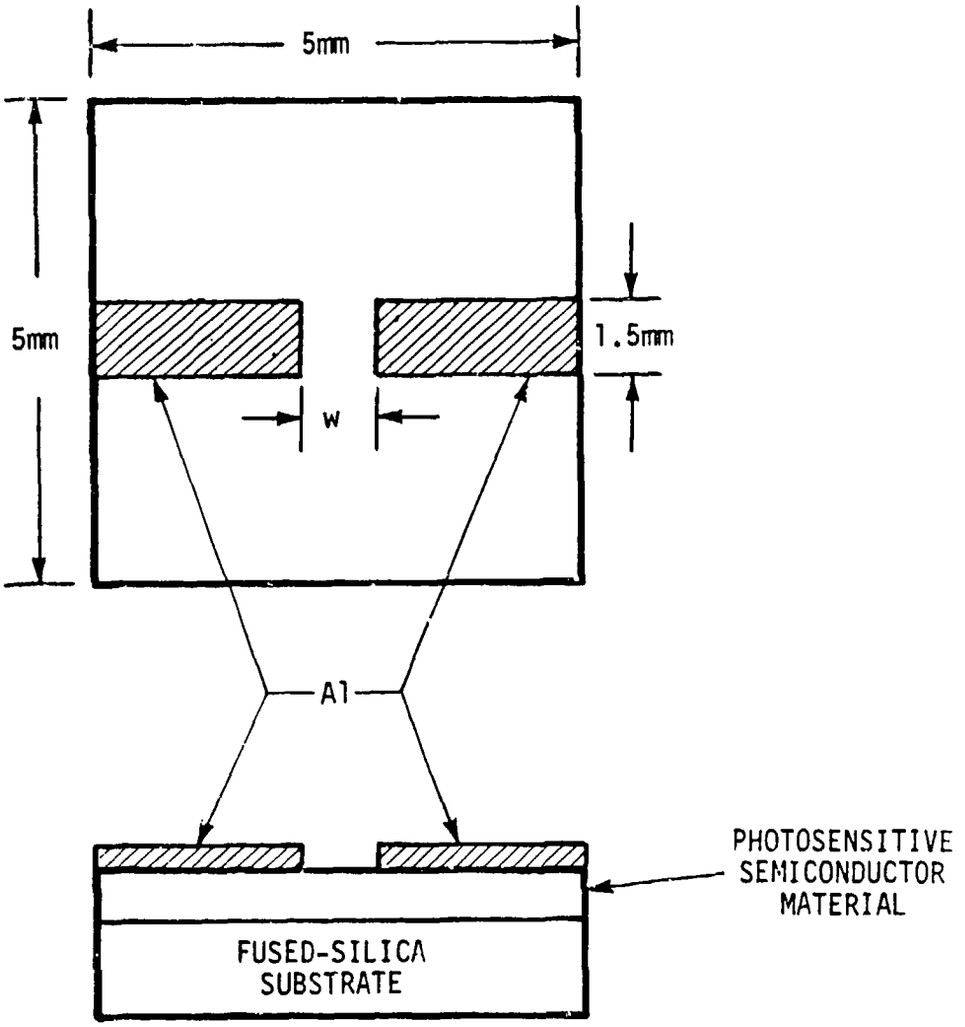

FIGURE 12. BASIC SWITCH CONFIGURATION

manner. The semiconductor films were deposited by RF sputtering using a chamber which was evacuated with a 450 L/sec turbomolecular pump to base pressures in the low microtorr range. High purity 7.6 cm diameter silicon (99.999%), GaSb (99.999%) and aluminum (99.99%) sputtering targets were used as sources for the silicon and GaSb active layers and the aluminum electrodes, respectively. Ultra high purity argon (99.9995%) and hydrogen (99.999%) were used as the sputtering gases. Argon and hydrogen partial pressures were measured with a capacitance manometer.

The glass substrates were inserted and removed from the vacuum chamber through an air lock, which greatly increased productivity since only the small air lock volume had to be evacuated. The source-substrate separation was 7 cm. Prior to inserting the alumino-borosilicate glass substrates into the coating chamber, they were cleaned by ultrasonic agitation in a heated solution of micro© and water for 1 hour, rinsed in hot distilled water for 30 minutes, and then rinsed in methanol for 2 hours with periodic changes of solution.

Two different electrode configurations were used. In the first case aluminum was deposited over the amorphous semiconductor layer and then etched to form the desired pattern. This approach was used with the silicon samples, but it was discovered that the GaSb samples crystallized during the etch process. The GaSb samples were therefore prepared by first depositing aluminum, etching to form the electrode pattern, and then depositing the GaSb layer over the aluminum

electrodes. The aluminum was magnetron sputter deposited with 400 watts applied power and 4 micron argon pressure. Under these conditions the aluminum coating rate was 3000 angstroms/minute.

The iron doped indium phosphide switches were fabricated by depositing a layer of gold on the indium phosphide substrate. This gold layer was then etched away to form the electrode pattern of the switch. The gold was deposited using the same vacuum chamber and process described above.

The chromium dope GaAs switches were fabricated using two different techniques. The GaAs switch presented a special problem in that a ohmic contact cannot be formed by simply depositing metal on the semiconductor. The formation of the ohmic contact required special processing and a detailed description of this fabrication process is given in Appendix F.

FINDINGS

The Findings section contains a discussion of three main topics: the detection and measurement of crack structures, laser induced transient signals, and optical switch characteristics.

Crack Measurements

The detection of small structural openings has been demonstrated using electromagnetic fields. The smallest crack that was reliably detected was 0.040 inches using frequency-domain techniques and 0.020 inches using time-domain techniques. Three different EM sources were used to investigate the crack structure: a laser induced source, a solid state pulser, and a frequency-domain continous wave (CW) source. The fields generated by the different sources were used to interrogate the crack structure. The received signals were then examined in both the time-domain and frequency-domain when applicable.

Time-Domain Measurements

The time-domain measurements involved using a short transient signal to excite a transmit antenna. This signal was produced by two methods: a laser induced source and a solid state electronic pulser. The induced pulse duration was less then the propagation time required for the signal to travel from the transmit antenna to the crack. By keeping the pulse

duration short with respect to this propagation time, the reflected signal from the crack structure was separated from the incident signal. The reflected signal was then compared to the incident signal to evaluate the crack structure under test. This type of measurement can be made using the set up shown in Figure 1. A transient signal was induced at the transmit antenna. The incident signal propagated across the crack and was received by the second antenna. The measured time delay was used to determine if the crack had widened (i.e. if the measured time delay increased by 20 picoseconds its was concluded that the crack had widened by 0.250 inches).

The time-domain measurement was useful if the crack was simply to be monitored for changes in the width. Accurate measurements were obtained for cracks as small as 0.020 inches with the solid state pulser as the source. Table 1 gives the actual versus measured crack sizes. The measurement accuracy was limited by the rise time and pulse duration of the pulser (which are directly related to bandwidth) and by the bandwidth and triggering jitter of the sampling equipment. The trigger jitter inaccuracies were greatly reduced by averaging the received waveform 1024 times. A similar measurement was made using the laser induced transient signals. Accurate measurements were obtained for cracks as small as 0.50 inches when the laser was used. The laser induced signal had the same triggering jitter and bandwidth limitations. The laser was able to generate larger bandwidth signals than the solid state pulser, however, it had two additional sources of errors that more than offset the benefit of the increased bandwidth. The two sources of errors were those caused by the laser pulse amplitude instability (greater then 5%) and the random noise

introduced by the plasma that is formed when the laser strikes the transmit antenna.

Table 1

Actual Crack Dimension (Inches)	Measured Crack Dimension (Inches)
0.025	0.035
0.050	0.047
0.075	0.083
0.100	0.106
0.150	0.154
0.200	0.201
0.250	0.248

The measurement accuracy could be improved by a factor of two by changing the test configuration to that shown in Figure 13. This setup was used to make time domain reflectrometry (TDR) measurements. With this test arrangement the signal propagated across the crack twice since the signal was reflected by the shorting block as shown. When the crack dimension was varied, the change in the time required for the signal to propagate from the transmit antenna to the receive antenna was twice the change that would be measured with the configuration shown in Figure 1. The technique of

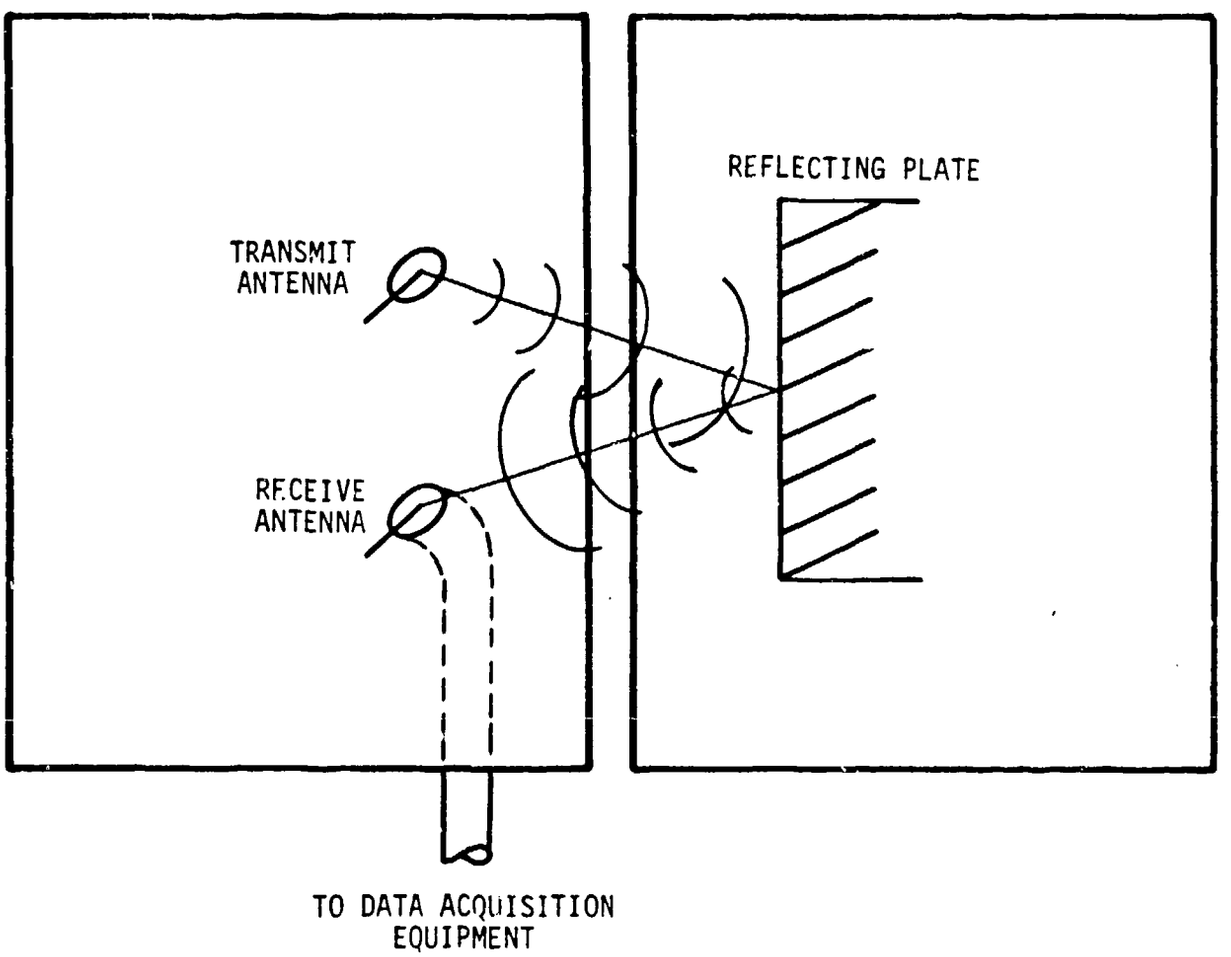

FIGURE 13. TIME DOMAIN REFLECTOMETRY CRACK MEASUREMENT

increasing the measurement accuracy by increasing the number of times the signal propagated across the crack was limited because the signal strength decreased with increased path length between the transmit and receive antennas. When the spacing became too large the signal-to-noise ratio was small, making accurate measurements difficult.

Frequency-Domain Measurements

The frequency-domain measurements were done by exciting the transmit antenna with a swept CW source and acquiring the signal at the receive antenna. The received signal was then examined in the frequency-domain for any differences that were attributed to the presence of the crack. This measurement technique was advantagous in that some information about the crack structure could be determined; however, it did not allow calculation of the crack width. An example is the crack structure shown in Figure 2 and the corresponding data in Figure 14. The data exhibit a resonance behavior every 2.6 GHz. This structure is related to the thickness of the ground plane (the ground plane is one-half wavelength at the first resonance). The data very clearly demonstrate that the EM fields are penetrating the crack structure and that the depth of the crack can be measured.

A simple algorithim was developed which used the frequency-domain data to generate an indicator to determine if the crack structure had changed from the calibrate position. The frequency-domain data were first taken with the crack in the nominal position (calibrate position). These data were then stored and used as a reference against which future measurements could be

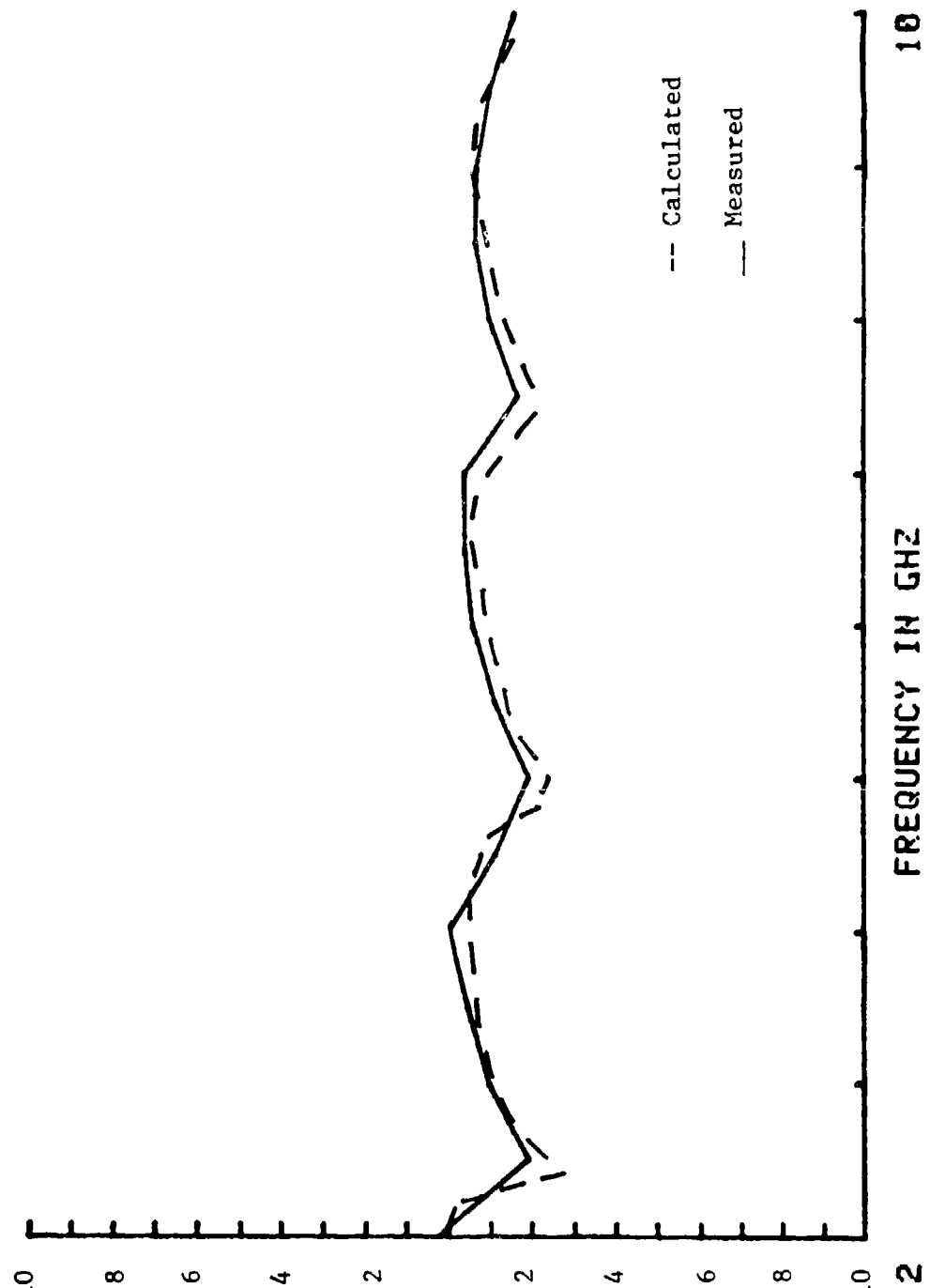

Figure 14. Scattered Plus Incident Field With the Crack Divided by Incident Field Without the Crack

compared. The future measurements were divided by the calibrate data. The resulting quotient was then processed to calculate a figure of merit, which could be used to determine if the crack had changed. The processing was done using two different techniques. The first technique was to calculate the root mean square (RMS) of the data difference and the second was to calculate the mean of the absoulute value (MAV) of the data difference. These two figures of merit values could be used to indicate the presence of a crack if the value exceeded a predetermined threshold. This would allow an automated system to be built that indicated the presence of a crack or change in a given structure. The selected threshold would be dependent on the type of crack to be monitored and the desired sensitivity. Figures 15 and 16 show the test structure configuration and the results of the measured data where the aforementioned technique was applied. A family of curves were taken for various gaps. The curves were generated by fixing the gap width "w" and varying the spacing "t", then changing the gap width "w" and repeating the measurements. By examining the data, the threshold would be selected based on the minimum crack dimension to be detected. The threshold was set to 1.0 for the MAV of the difference and a threshold of 20.0 was used for the RMS of the difference. From the data it can be deduced that the cracks as narrow as 0.020 inch were detected.

Data measurements in the frequency-domain were made using both the transient sources and the frequency-domain CW source. The CW source was used in conjunction with the HP network analyzer. The network analyzer was used to measure the frequency-domain characteristics directly. As mentioned before this measurement technique had the advantage of producing high accuracy

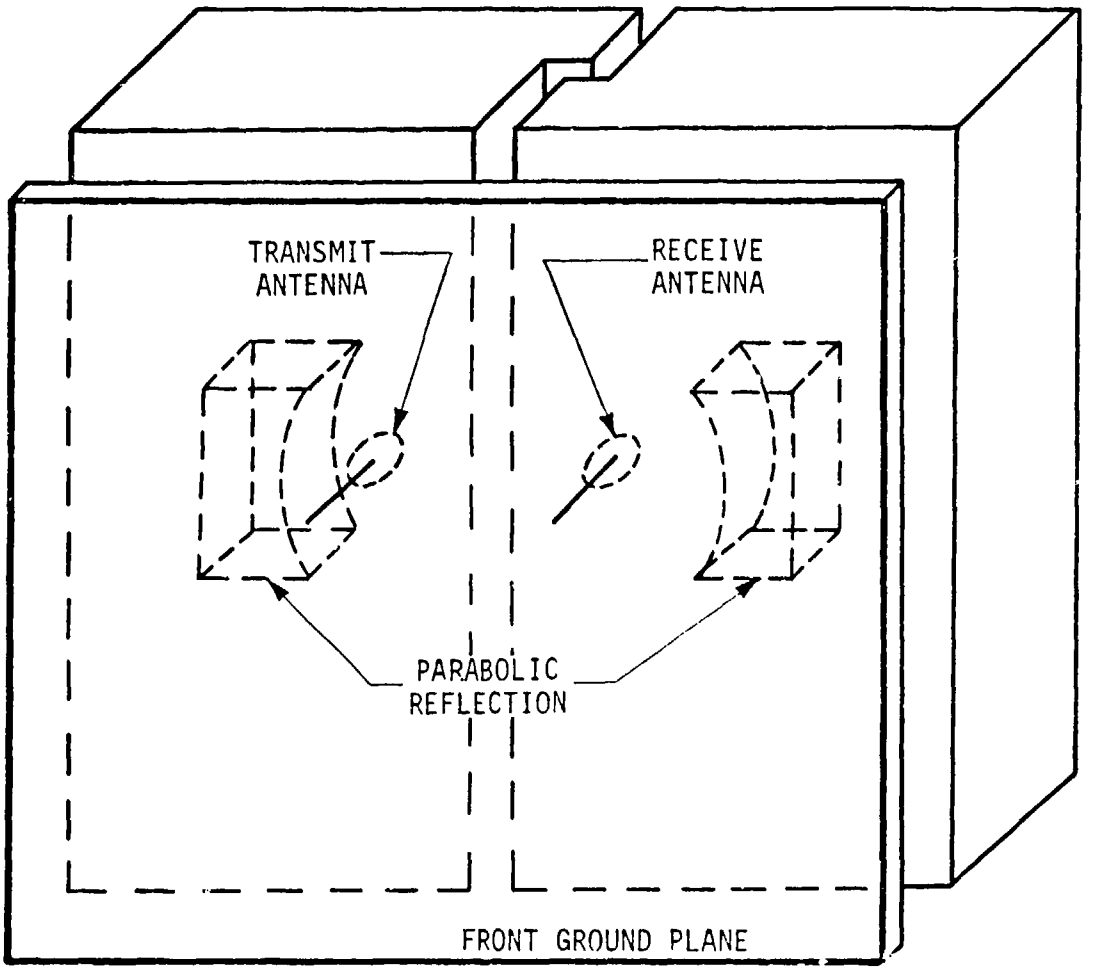

FIGURE 15. FREQUENCY DOMAIN TEST SET WITH TOP GROUND PLANE AND PARABOLIC REFLECTORS

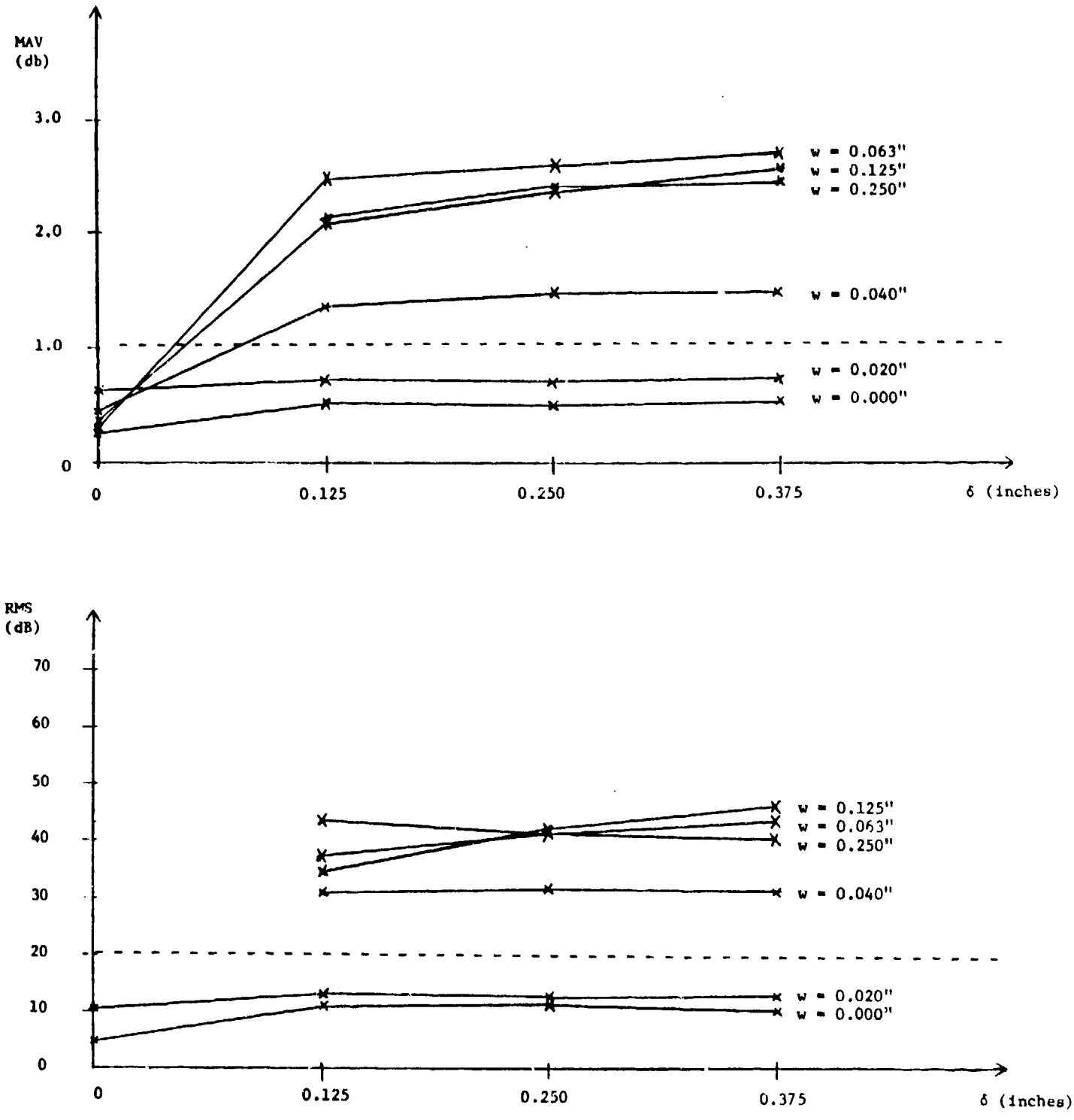

Figure 16. Frequency-Domain Data for Crack Width "w" Varied from 0.0 Inch to 0.25 Inch

measurements; however, the measurements could be time consuming when the frequency step size was small. The transient sources were also used to generate frequency-domain data in the following manner. A voltage transfer measurement between the transmit and receive antennas was made. This time-domain waveform was then converted into the frequency-domain by using a Fast Fourier Transform (FFT) program. Data obtained by the latter technique versus the former technique were less accurate; however, it took much less time to generate. The data obtained by the two techniques did compare very favorably between 3 and 10 GHz. For frequencies below 3 GHz the transmit and receive antennas were a very poor electrical match. This mismatch prevented the source from coupling enough energy to the transmit antenna to make accurate measurements (i.e., the signal-to-noise ratio was too low). The transient signal from the pulser was bandwidth limited for frequncies above 12 GHz and the response began to drop at 10 GHz. It was concluded that the data do not match for frequencies below 3 GHz because of the antenna mismatch and above 10 GHz because of the lack of spectral content of the pulser.

Measured Versus Calculated Data

Two computer codes were generated as part of this program. The goal of each of these programs was to model the fields created by monopoles radiating on a ground plane in the presence of a narrow crack. The first program used a moment method type of solution, but it was limited to the case of an infinitesimally thin ground plane. The second program used a traveling wave source to model the transmit antenna which allowed the program to model the

finite thickness of the ground plane without encountering theoretical and numerical problems.

The moment method program was used to calculate the effects of finite length monopole antennas mounted on an infinite ground plane. As part of this analysis the input impedance of the monopoles was calculated. The resulting impedances were used to enhance the calculations of the program that used the traveling wave sources. The resulting input impedances from the moment method solution were compared against measured data with the results shown in Figure 17. The data matched very well, with the exception of a shift in the resonance frequency. This shift was most severe for short antennas (0.250 inches or less). It was concluded that secondary effects, which were not modeled, were becoming important for the short antenna (i.e., length to diamater ratio was no longer large).

The moment method solution was expanded to calculate the voltage transfer characteristic between two monopoles mounted above a ground plane without the presence of a slit. The voltage transfer data matched the measured data when no crack was present as shown in Figure 18. The limitation of the moment method solution was the restriction that the ground plane be infinitesimally thin.

The program that used the traveling wave solution was able to correctly model the effects of a finite thickness ground plane. However, the solution assumed that the transmit and receive antennas had an infinitesimal length. The program was modified to allow antenna lengths that were less then

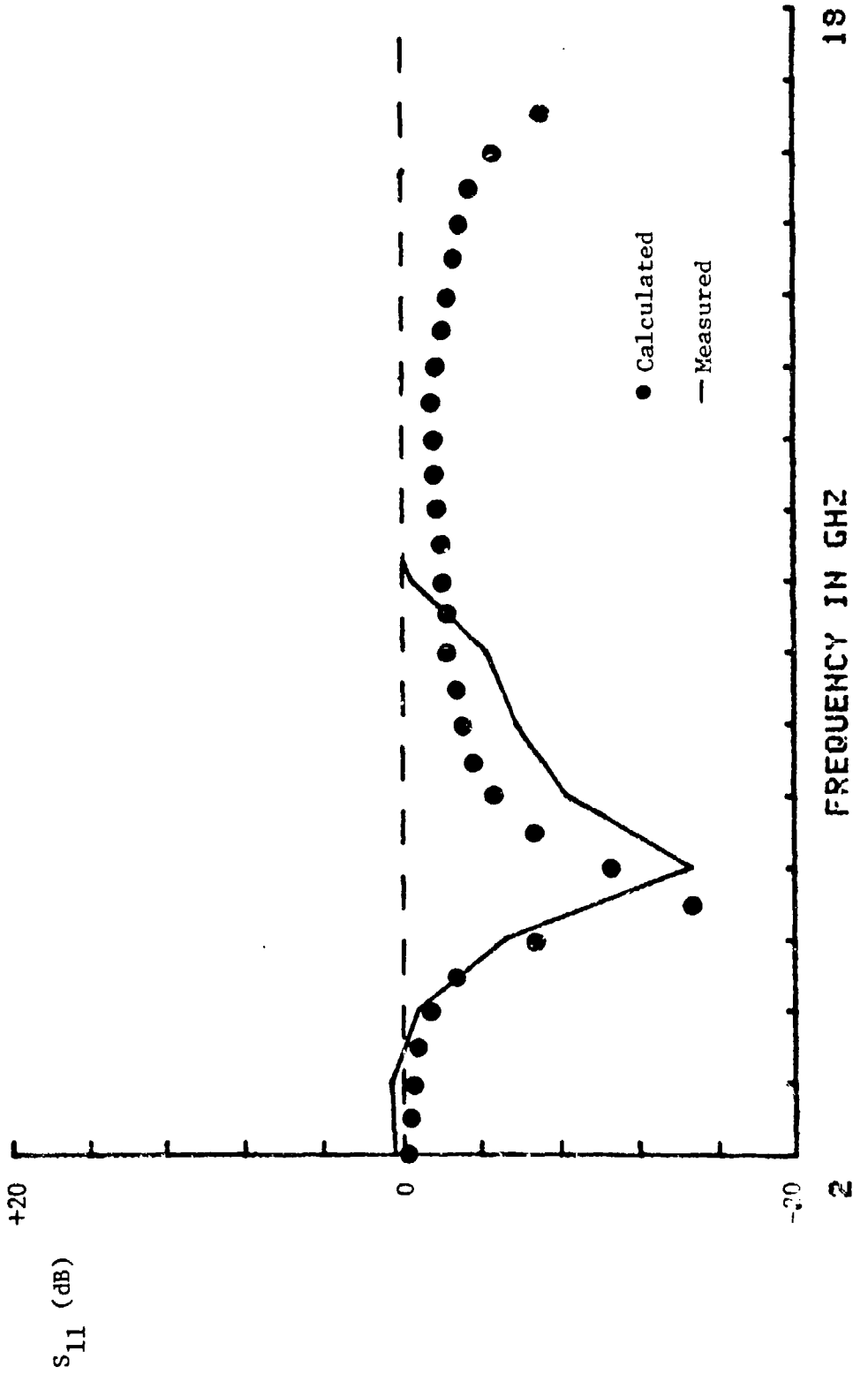

Figure 17. Input Scattering Coefficient as a Function of Frequency

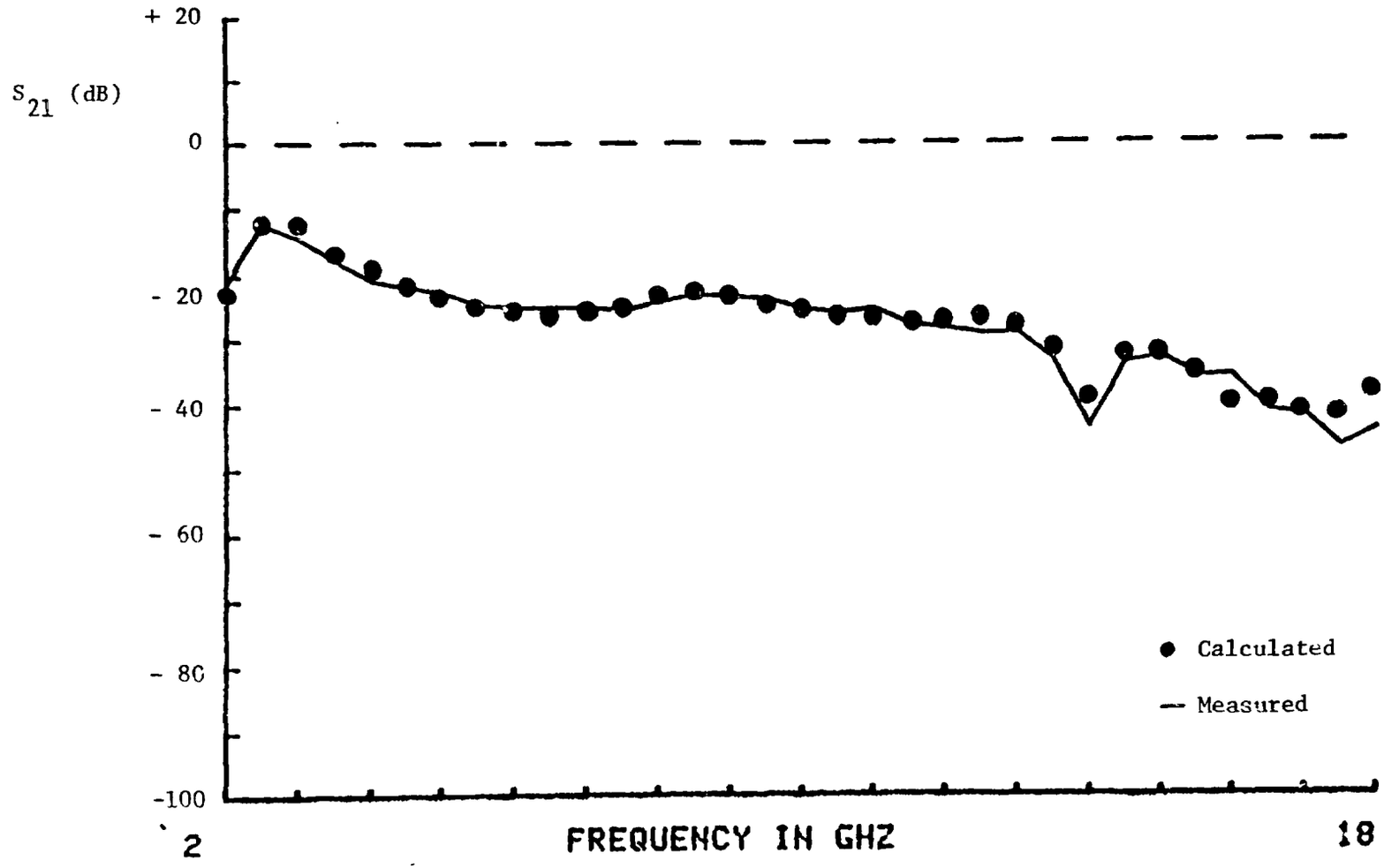

Figure 18. Transfer Characteristics Between Two Monopoles Mounted on a Ground Plane

one-half wavelength by incorporating the result from the moment method solution. The program results were compared with measured data by using the ratio of the calculated fields with a crack to the fields without a crack. Figure 14 shows the excellent agreement between theory and experiment.

Laser Induced Transient

The laser was used to generate a transient microwave signal on an antenna by illuminating it with a short duration, high intensity optical beam. This high intensity illumination caused thermionic emission; the effect of the thermionic emission was the same as a transient current monopole at the target surface. In the time-domain, this excitation could be approximated by an impulse which would have a correspondingly broadband excitation in frequency. This transient pulse could be used to find the Green's Function response of a given system.

The laser induced transient source exhibits two very important advantages over conventional transient sources; it is very broadband and it can be used to excite an antenna without requiring physical connection to the antenna. The bandwidth generated by the laser induced transient is approximately proportional to the reciprocal of the pulse width. For the Quantel laser used (YG 402) the laser pulse width was 30 ps, potentially yielding bandwidths as high as 33 GHz. Conventional sources require a direct physical connection between the source and the transmit antenna (i.e. cable or a waveguide). This connection contaminates the feed area of many transmit antennas and disturbs the radiation pattern of the antenna. The

laser beam can be used to induce a transient at the feed point of the antenna without a direct connection and therefore not disturb the radiation pattern of the antenna.

When the laser beam hits a target a broadband excitation is produced. The excitation will induce various modes in the illuminated structure. The modes will be attenuated unless that mode is supported by the structure. As an example of structurally dependent modes, if the target were a dipole antenna suspended in free space the supported modes would be those which correspond to the dipole length being an integer multiple of a half wavelength.

The laser induced bandwidth was measured to be greater than 14 GHz using the Tektronix sampling equipment as described in the Procedure section of this report. The bandwidth of the sampling equipment begins to roll off at 14 GHz; however, frequencies as high as 20 GHz can be measured with a large attenuation factor. As shown in Figure 19 the frequency spectrum of the induced signal, when the laser strikes a ground plane, has rolled off 15 dB at 14 GHz. These data were measured by using a 0.250 inch receive monopole mounted 1.75 inches from the target.

The amplitude of the laser induced signal was dependent on the medium surrounding the target area and the intensity of the optical beam illuminating the target. The illumination of the target caused thermionic emmission to occur at the surface leading to the flow of electrons from the target. The mean free path of the electrons is related to the induced

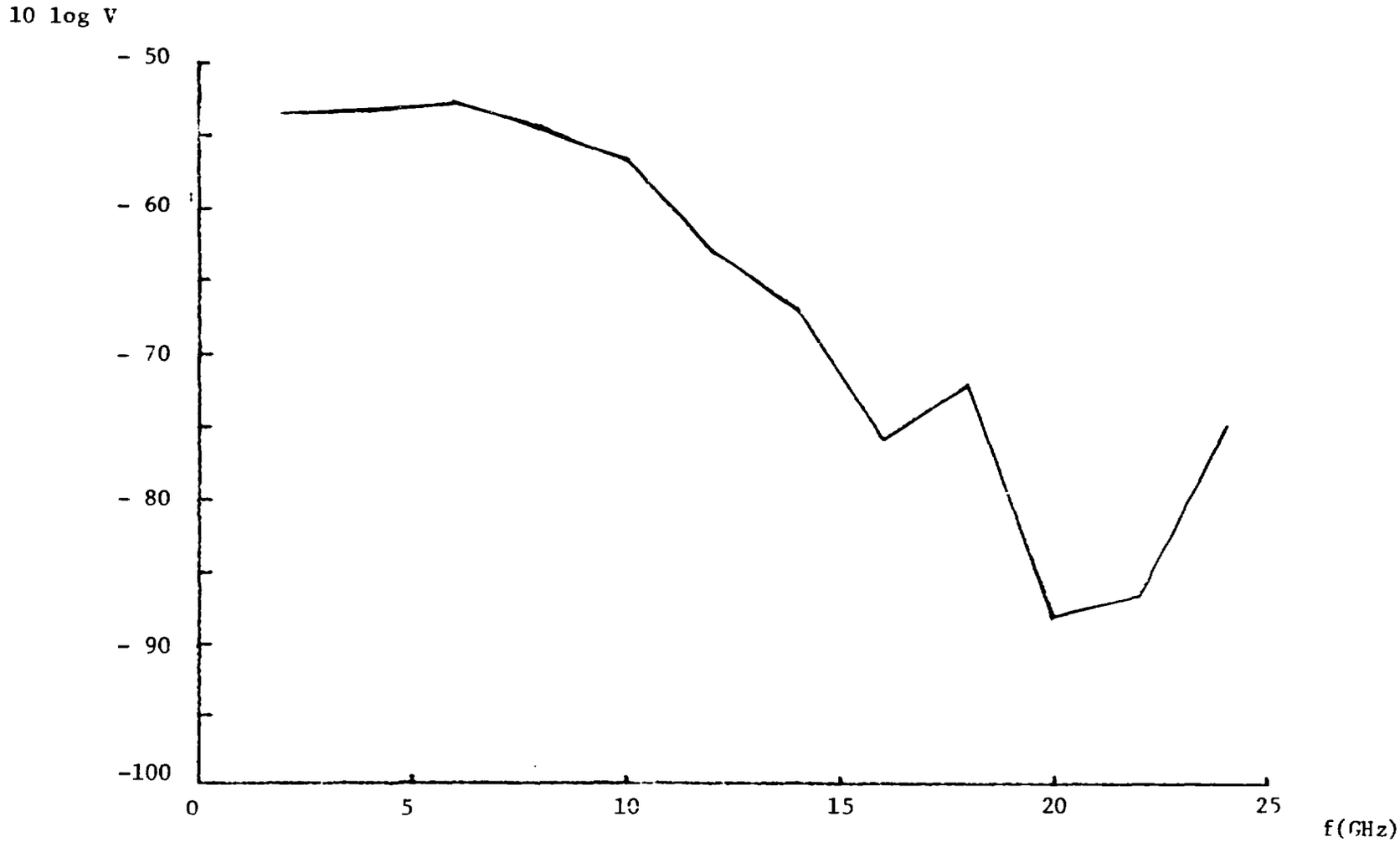

Figure 19. Frequency Spectrum of Laser Induced Transient

signal strength; specifically, the larger the mean free path length the larger the induced signal. Since the mean free path length of electrons in air is exceedingly short, the induced signal strength was increased. By evacuating the atmosphere surrounding the target or replacing it with an inert gas (such as helium) the mean free path length and the induced signal strength were increased.

Optical Switch Data

The switch parameters of most interest to this program were as follows: the switching speed, the ratio of the "off-resistance" to the "on-resistance", and the optical sensitivity. The switching speed was measured using the technique described in the Procedure section of this report.

Switch speeds for a-Si were measured between 100 ps and 213 ps. There was no obvious correlation between the hydrogen doping and the switching speed or between the semiconductor thickness and the switching speed. This correlation was made more difficult by the limited number of switch samples. The switching speed was marginally acceptable for a sampler with a bandwidth as high as a 5 GHz. However, the optical sensitivity and the ratio of the "off-resistance" to the "on-resistance" were not acceptable. The switches required nearly 30% of the available laser power to obtain these switching speeds. At this power level, the switches had a limited life of at most a few thousand transitions from the "off-resistance" state to the "on-resistance" state. The measured ratio of the "off-resistance" to the "on-resistance" was less then 100. This ratio should be greater than

100,000 for proper operation of the sampler. Because of the limitations encountered with the a-Si, other materials were considered.

The iron doped InP switches were measured to have a switching time on the order of 2 nanoseconds which is much slower than what has been reported in the open literature. These switches were fabricated by depositing a layer of gold on the InP and then etching the desired switch contacts. The switch contacts were the only variable of design that was available in the time frame of this program.

The GaAs switches have been fabricated using two different techniques, as described in Appendix F. The measured switch time was 2 nanoseconds and the optical sensitivity was far superior to that of the a-Si. These switches required less then 1% of the available laser power. The ratio of the "off-resistance" to the "on-resistance" was greater then 750:1. These switches are still not adequate for the sampler application. However, a set of switches that was fabricated using the second fabrication process and a substrate that was designed for ion implantation showed promise of being superior. Preliminary tests indicated that the "off-resistance" was very high and that switching could be induced under room ambient light.

The resistivity of the GaSb films varied significantly with hydrogen partial pressure during deposition. Figure 20 summarizes the resistivity of the GaSb after deposition. An abrupt decrease in film resistivity occurs when the hydrogen partial pressure exceeds 2 millitorr. The abrupt decrease in resistivity appears to be associated with an amorphous to crystalline phase

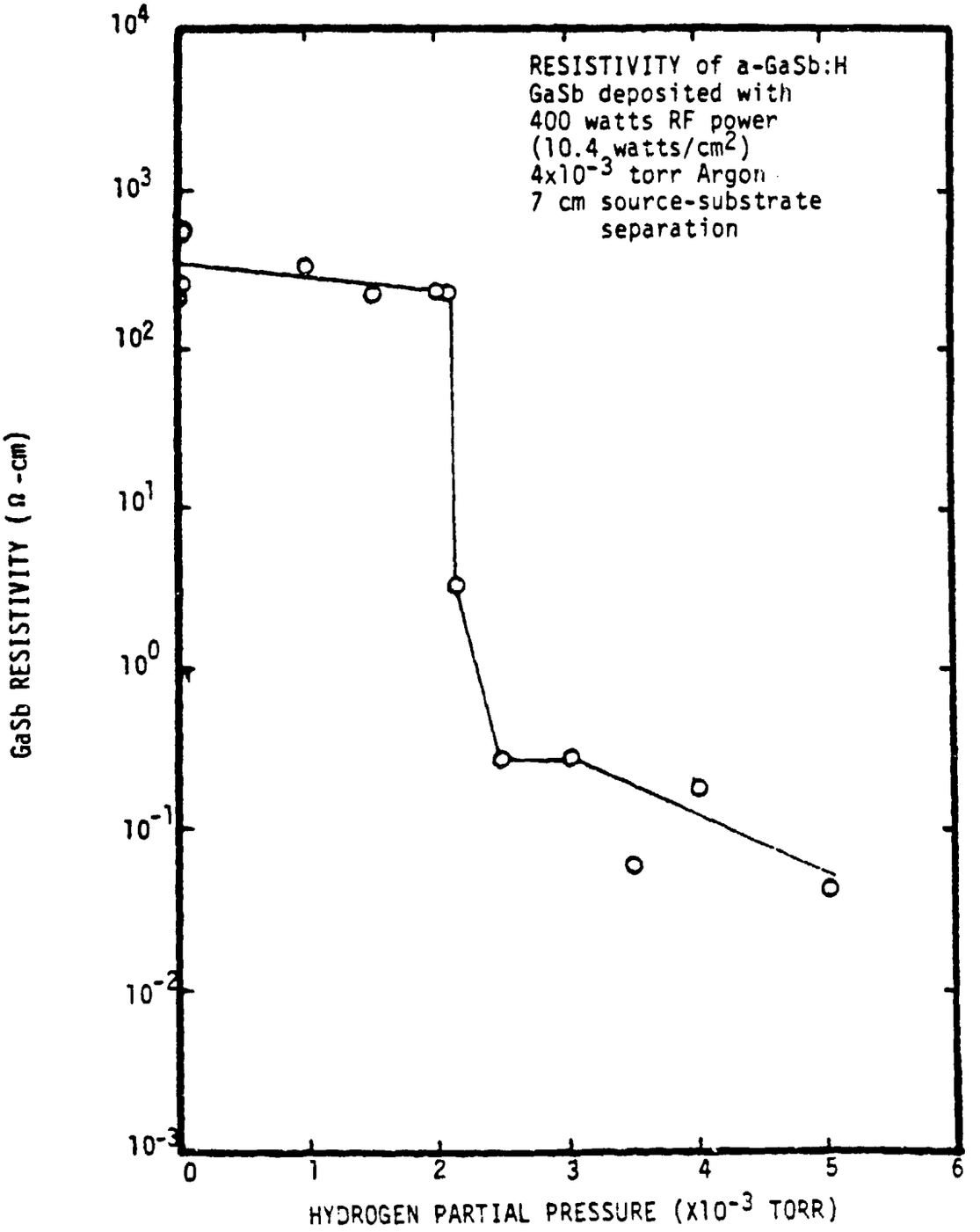

Figure 20. GaSb Resistivity as a Function of Hydrogen Partial Pressure

transformation. GaSb films deposited with hydrogen appear to have a lower crystallization temperature which falls below the deposition temperature at 2 millitorr hydrogen partial pressure.

CONCLUSIONS

The technique of using electromagnetic fields to investigate the characteristics of a structure has been demonstrated to be valid. The laboratory experiments have shown that cracks with dimensions as small as 0.020 inches can be detected and that it was possible to determine simple features of this structure. The detection of smaller cracks may be possible with the existing electronic hardware but the mechnical tolerances of the test structure were inadequate. Repeatability (or resolution) in the crack structure placement prevented finer measurements than 0.020 inches. To detect smaller cracks, improvements will be needed in laboratory instrumentation and EM sources.

The laser was used to generate a very short transient with a measured frequency content as high as 20 GHz. The application of this source was limited by the processing time required to reduce the noise inherent in the laser induced transient signal. The successful development of the single-shot transient sampler, as described in this report, would greatly reduce the required processing time and enhance the usefulness of the laser induced source.

The solid state electronic pulser and frequency-domain CW source were also used to create the EM fields. These sources were applicable depending on the test to be performed. The pulser performed a function very similar to that of the laser induced transient. The CW source was used mainly for the frequency domain measurements.

The development of this single-shot transient sampling device is limited by the availability of optically strobed photoconductive switches that have the required charateristics (high optical sensitivity, high ratio of "off-resistance" to "on-resistance", and fast switching speed). The successful fabrication of the optically sensitive photoconductive switch would have major impact on the advancement of transient sampling devices.

The computer programs that were used to model the electromagnetic geometry have been used to predict the leakage levels of the fields propagating through a small structural crack. The traveling wave line source program can also be used to determine what leakage levels would exist for a given crack structure without requiring laboratory measurements. These programs could be expanded to analyze more complex crack structures without major modifications. The ability to handle a more general crack structure is important for future application of these computer codes.

FUTURE WORK

The laboratory and theoretical demonstrations that electromagnetic energy can be employed to monitor structural characteristics have only set a foundation for further work. Certainly more remains to be done in the area of monitoring structural deformations and changes in narrow slits. The theoretical models should be updated to allow different geometries and constitutive parameters in the cracks. Fundamental research must be done on the photoconductive switches so materials and geometries can be optimized with respect to the required properties uncovered during this program. Measurement techniques and signal processing capabilities must be optimized also to allow maximum information to be obtained from the raw acquired data. Although research must continue, proof-of-principle has been established.

The next iteration on the present problem will require one or two monitoring techniques to be selected as the most likely candidates for achieving the specified goals. After further optimization, a laboratory brassboard system should be designed and fabricated for real-world testing. This initial implementation will identify the technologies required for a totally integrated monitoring system. Concurrent with that development, efforts should continue on the ultra-fast, single-shot transient sampler designed under this phase of the research program. The critical item in this technology is the optically strobed photoconductive switch which allows a digitally processable "photograph" of an extremely fast changing event. The final development of these switches will allow implementation of devices which will have wide applications in existing and emerging technologies. In

addition to this sampler, application of the transmission line and switch combination can be made in receivers and possibly even adaptive phased arrays which could use the device to perform real-time signal processing, a requirement which is critical for maximum exploitation of electronic array technology.

Further research and development of laser induced transient excitation is needed because of its potential application to several major measurement problems. In addition to its ability to monitor structural deformation, its application to radar signal/target interaction research has not been studied. The laser's ability to place a single isolated transient monopole at an arbitrary position on a geometrical shape would allow a system to be designed and built which functioned as a portable radar cross section diagnostic tool capable of high spatial resolution. This application would allow the experimental measurement of a target's theoretical Green's function which is central to rigorous analytical radar cross section studies. This system could be employed to test the contributions of individual geometric features of a complex target tc its overall radar cross section. The combination of the short monopole's isolation, mobility, and wide frequency spectrum leave its potential for innovative applications unlimited.

APPENDIX A

DERIVATION OF THE ELECTRIC FIELDS FOR A FINITE SOURCE NEAR A SLIT IN A GROUND PLANE WITH FINITE THICKNESS

APPENDIX A. DERIVATION OF THE ELECTRIC FIELDS FOR A FINITE SOURCE NEAR A SLIT IN A GROUND PLANE WITH FINITE THICKNESS

This Appendix contains the derivation of the equations used to calculate the electric field radiated by a monopole in the near field of a narrow slit in a ground plane. This derivation is based on a paper by Harrington and Auckland [12] in which they considered a plane wave incident on a ground plane with a narrow crack. This analysis was modified during this research program to allow a more general type incidence to be considered.

The finite length monopole radiating near a slit in a ground plane was first analyzed by modeling it as an infinitesimal length monopole with an effective current moment. The infinitesimal length monopole was, in turn, modeled as a spectrum of traveling wave line sources traveling parallel to the slit in the ground plane. This change was made by taking a spatial Fourier Transform with respect to the z-axis. The traveling wave line source generated a cylindrical wave illumination with a modified propagation constant. The derivation by Harrington and Auckland could then be used with the modified propagation constant substituted for the free space propagation constant.

The inverse spatial Fourier Transform was then calculated to obtain the actual fields from the infinitesimal monopole source. The transformation was accomplished using numerical integration. A singularity, which had to be skirted, was encountered when performing the inverse transformation. The expression for skirting the singularity was integrable with appropriate small argument approximations and solved analytically.

A. TRAVELING WAVE LINE SOURCE

The problem to be solved is the characterization of the electromagnetic fields in and near a crack due to a traveling wave line source

illuminating an electrically thin slit in a ground plane. Figure A-1 shows the geometry. The line source has current

$$\underline{\tilde{J}}^i = -\hat{x}\, e^{j\omega t} \quad , \tag{A-1}$$

that travels in the z-direction and is located at (x,y) = (0, - L). All currents and fields in this Appendix are assumed time harmonic, i.e., $e^{j\omega t}$ time dependence. The $e^{j\omega t}$ factor will henceforth be omitted but implicitly understood to be present in the following field equations. The "~" over a quantity indicates that it is in the spatial transform domain. Ultimately, an integration, which is given below, was performed to return to the standard frequency domain. The slit has width w and is in a ground plane of thickness d. Space is divided into three regions as indicated in Table A-1. To facilitate analysis, the crack of width w and depth d is considered to be electrically small in width.

TABLE A-1. REGIONS OF SPACE

Region	x	k	Comment
a	x<o	$\omega\sqrt{\mu_a \epsilon_a} = k_a$	Illuminated
b	o<x<d	$\omega\sqrt{\mu_b \epsilon_b} = k_b$	Waveguide
c	x>d	$\omega\sqrt{\mu_c \epsilon_c} = k_c$	Shadowed

The solution to this problem has been formulated by Harrington and Auckland. As described in this paper, the fields in all regions can be evaluated in a straightforward manner once the equivalent currents

$$\underline{\tilde{M}}_1 = \hat{x} \times \underline{\tilde{E}} \text{ (in aperture } A_1) \tag{A-2}$$

$$\underline{\tilde{M}}_2 = -\hat{x} \times \underline{\tilde{E}} \text{ (in aperture } A_2) \tag{A-3}$$

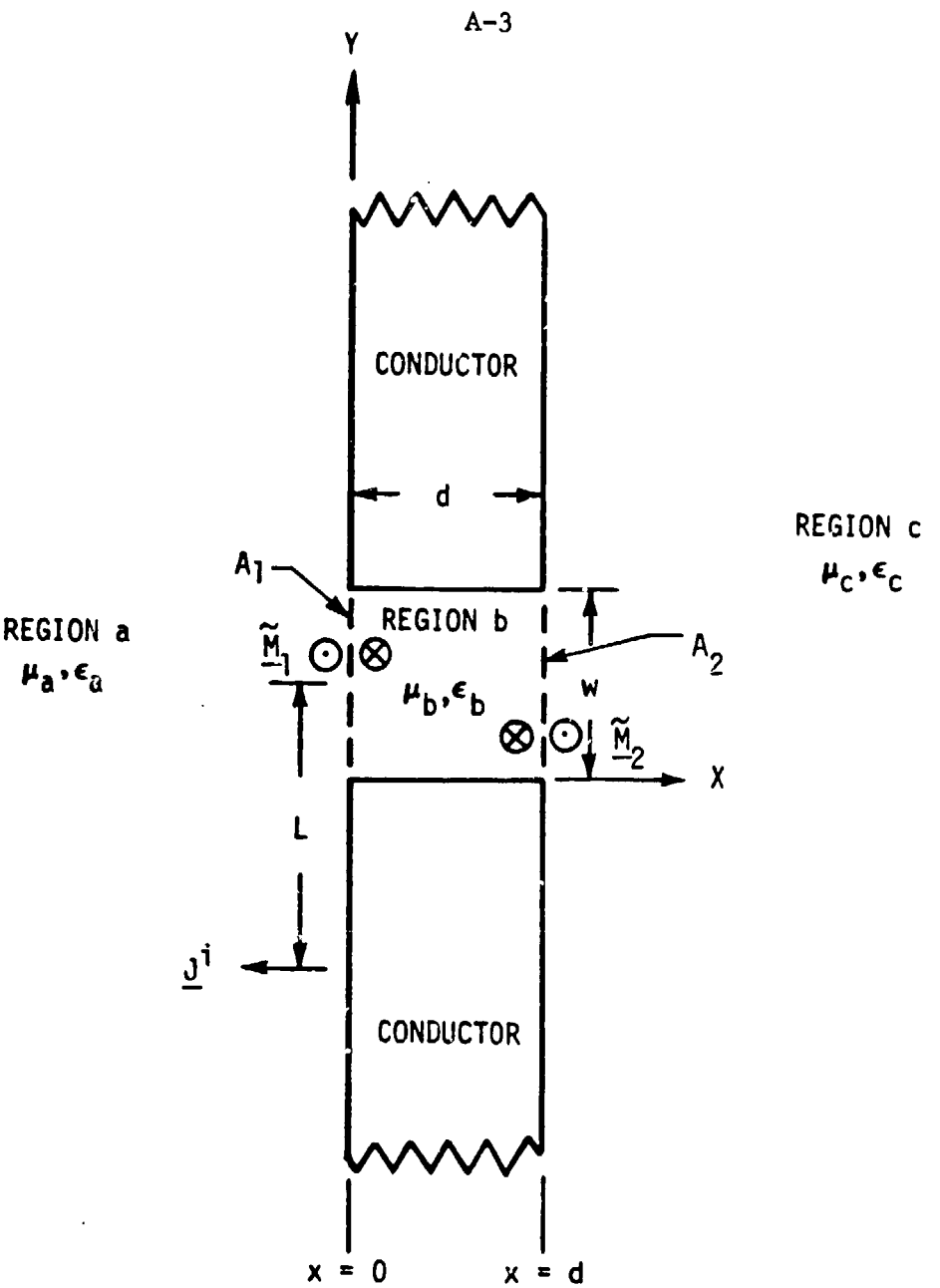

FIGURE A-1. UNIFORM SLIT OF WIDTH w IN PERFECTLY CONDUCTING SCREEN OF THICKNESS d

are known. $\tilde{\underline{E}}$ is the total electric field and consists of the incident field plus the scattered field. The directions of $\tilde{\underline{M}}_1$ and $\tilde{\underline{M}}_2$ are given in Figure A-1.

While Harrington and Auckland presented the specific solution for plane wave exictation of the slit, the solution for the traveling wave line source is of interest to this research. These two solutions are mathematically similar, and this feature will be emphasized through the use of notation paralleling that of Harrington and Auckland.

Since the slit is assumed electrically thin, the following approximations can be made with the TM modes cut-off:

1. In region b and in the apertures, $\tilde{\underline{E}}$ is entirely $\hat{y}$ polarized
2. In region b and in the apertures, $\tilde{\underline{E}}$ is uniform with y.

In this case Equations (A-2) and (A-3) can be written as

$$\tilde{\underline{M}}_1 = V_1 \tilde{\underline{M}} \tag{A-4}$$

$$\tilde{\underline{M}}_2 = V_2 \tilde{\underline{M}} \tag{A-5}$$

where V_1 and V_2 are unknown constants and

$$\tilde{\underline{M}} = \hat{z}/w \ . \tag{A-6}$$

Using a moment method (MM) solution with test modes identical to the expansion modes in Equations (A-4) and (A-5), V_1 and V_2 are solutions of

$$\begin{aligned} \tilde{Y}^a V_1 + \tilde{Y}^b_{11} V_1 + \tilde{Y}^b_{12} V_2 &= \tilde{I}^i \\ \tilde{Y}^b_{21} V_1 + \tilde{Y}^b_{22} V_2 + \tilde{Y}^c V_2 &= 0 \ . \end{aligned} \tag{A-7}$$

$\tilde{Y}^a$ is the admittance of aperture A_1 looking into region "a" and is computationally given by

$$\tilde{Y}^a = -\frac{1}{w} \int_0^w \hat{z} \cdot \tilde{\underline{H}}^a_t (\tilde{\underline{M}}) \, dy \ . \tag{A-8}$$

$\underline{\tilde{H}}_t^a(\underline{\tilde{M}})$ is the tangential magnetic field of $\underline{\tilde{M}}$ located in aperture A_1 radiating into region "a" with aperture A_1 shorted.

Similarly,

$$\tilde{Y}^c = -\frac{1}{w}\int_0^w \hat{z} \cdot \underline{\tilde{H}}_t^c(\underline{\tilde{M}})\, dy \qquad \text{(A-9)}$$

is the admittance of aperture A_2 looking into region "c" with $\underline{\tilde{H}}_t^c(\underline{\tilde{M}})$ corresponding to the tangential magnetic field of $\underline{\tilde{M}}$ located in aperture A_2 radiating into region "c" with aperture A_2 shorted. The admittances

$$\begin{aligned} \tilde{Y}_{11}^b &= \tilde{Y}_{22}^b = \tilde{Y}_o \coth \gamma_b d \\ \tilde{Y}_{12}^b &= \tilde{Y}_{21}^b = \tilde{Y}_o/\sinh \gamma_b d \end{aligned} \qquad \text{(A-10)}$$

are the two-port parameters for a transmission line of length d with propagation constant

$$\gamma_b = +\, j\sqrt{k_b^2 - \beta^2} \qquad \text{(A-11)}$$

and characteristic admittance

$$\tilde{Y}_o = \frac{\gamma_b}{j\omega w \mu_b} \quad . \qquad \text{(A-12)}$$

The impressed current, $\tilde{I}^i$, is given by

$$\tilde{I}^i = \frac{1}{w}\int_0^w \tilde{H}_z^{sc}(\underline{\tilde{J}}^i)\, dy \qquad \text{(A-13)}$$

where $\tilde{H}_z^{sc}(\underline{\tilde{J}}^i)$ is the z component of the magnetic field of $\tilde{J}^i$ with aperture A_1 shorted.

The aperture admittances of Equation (A-8) can now be evaluated. The field of a traveling wave, $\hat{z}$-polarized magnetic line source located at (x'=0, y') and radiating into region "a" is

$$d\tilde{H}_z^a = \begin{cases} \dfrac{-1}{4\omega\mu_a} h_a^2 H_o^{(2)}(h_a\rho)\, \dfrac{dy'}{w} & \beta < k_a \\[2ex] \dfrac{1}{4\omega\mu_a} \alpha_a^2\, j\, \dfrac{2}{\pi} K_o(\alpha_a\rho)\, \dfrac{dy'}{w} & \beta > k_a \end{cases} \qquad \text{(A-14)}$$

where K_o is a modified Bessel function of zeroeth order, $H_o^{(2)}$ is the zeroeth order Hankel function of the second kind,

$$\rho = \sqrt{(x-x')^2 + (y-y')^2} \quad , \tag{A-15}$$

$$h_a = + \sqrt{k_a^2 - \beta^2} \qquad \beta<k_a \text{ , and} \tag{A-16}$$

$$\alpha_a = + \sqrt{\beta^2 - k_a^2} \qquad \beta>k_a \tag{A-17}$$

where

$$\alpha_a = jh_a \quad . \tag{A-18}$$

For field points in aperture A_1, $\rho = |y-y'| \leq w$, $h_a\rho << 1$, and $\alpha_a\rho << 1$ (provided β is not $>>k_a$). Thus the following approximations are valid

$$H_o^{(2)}(h_a\rho) \sim 1 - j\frac{2}{\pi}\ln(h_a\rho) \qquad \beta<k_a \tag{A-19}$$

$$K_o(\alpha_a\rho) \sim -\ln(\alpha_a\rho) \; . \qquad \beta>k_a \tag{A-20}$$

Using these small argument approximations, the magnetic field of $\tilde{\underline{M}}$ is given by

$$\hat{z} \cdot \tilde{\underline{H}}_t^a(\tilde{\underline{M}}) = 2 \int_o^w d\tilde{H}_z^a$$

$$= \begin{cases} \frac{-1}{2\pi\omega w\mu_a} h_a^2 \left[\pi w + j\,2\left(-y\ln\{h_a y\} - (w-y)\ln\{h_a(w-y)\} + w\right)\right] & \beta<k_a \\ \frac{1}{2\pi\omega w\mu_a} \alpha_a^2 \left[j\,2\left(-y\ln\{\alpha_a y\} - (w-y)\ln\{\alpha_a(w-y)\} + w\right)\right] \; . & \beta>k_a \end{cases} \tag{A-21}$$

Note that the factor of 2 in the top Equation (A-21) accounts for the image of $\tilde{\underline{M}}$ into the ground plane. Inserting Equation (A-21) into (A-8) and integrating yields

$$\tilde{Y}^a = \begin{cases} \dfrac{h_a^2}{2\pi\omega\mu_a} \left[\pi + j\,(3-2\ln\{h_a w\})\right] & \beta<k_a \\ \dfrac{-\alpha_a^2}{2\pi\omega\mu_a} \left[j\,(3-2\ln\{\alpha_a w\})\right] & \beta>k_a \,. \end{cases} \tag{A-22}$$

$\tilde{Y}^c$ can be obtained from $\tilde{Y}^a$ by simply changing the subscript "a" to "c".

As seen by Equation (A-13), $\tilde{I}^i$ is simply the average value of $\tilde{H}_z^{sc}$ ($\tilde{J}^i$) over aperture A_1. If L>>w, the impressed current is simply

$$\tilde{I}^i = \begin{cases} + j\,\dfrac{h_a}{2} H_1^{(2)}(h_a L) & \beta<k_a \\ - \dfrac{\alpha_a}{\pi} K_1(\alpha_a L) & \beta>k_a \,. \end{cases} \tag{A-23}$$

$H_1^{(2)}$ denotes the first order Hankel function of the second kind, and K_1 is the first order modified Bessel function.

Using the transmission line model presented by Harrington and Auckland, the aperture amplitudes are

$$V_2 = \tilde{I}^i/\tilde{Y}_{12} \quad , \text{ and} \tag{A-24}$$

$$V_1 = - V_2[\cosh \gamma_b d + (\tilde{Y}^c/\tilde{Y}_o) \sinh \gamma_b d] \quad , \tag{A-25}$$

where the transfer admittance

$$\tilde{Y}_{12} = -\left\{(\tilde{Y}^a + \tilde{Y}^c) \cosh \gamma_b d + [\tilde{Y}_o + (\tilde{Y}^a\tilde{Y}^c/\tilde{Y}_o)] \sinh \gamma_b d\right\}. \tag{A-26}$$

Since the crack of width w is electrically small, the scattered field in region "a" or the transmitted field in region "c" is radiated by a traveling wave magnetic line source: $V_1\tilde{M}$ located in the center of aperture A_1 or $V_2\tilde{M}$ located in the center of aperture A_2, respectively, with the apertures shorted. For example, the electric field in region "a" is

$$\tilde{\underline{E}} = \begin{cases} j \frac{V_1}{2} h_a H_1^{(2)}(h_a\rho) \hat{\phi}_{M1} & \beta<k_a \\ -\frac{V_1}{\pi} \alpha_a K_1(\alpha_a\rho) \hat{\phi}_{M1} & \beta>k_a \end{cases} \qquad \text{(A-27)}$$

where ρ is the distance from the center line of aperture A_1 to the field point. A factor of two is included in Equation (A-27) to account for the image of $V_1\tilde{\underline{M}}$ in the ground plane. The directions of $\hat{\phi}_{M1}$ and $\hat{\phi}_{M2}$, as defined by the magnetic current sources, are shown in Figure A-2.

B. INFINITESIMAL CURRENT ELEMENT

In the previous section the fields of a traveling wave line source illuminating an electrically thin slit in a ground plane were found. In this section the fields of an infinitesimal current element are computed by inverse transforming the fields of the traveling wave line source. The impressed source is now the infinitesimal current element

$$\underline{J}^i = -\hat{x} \qquad \text{(A-28)}$$

and is located at $(x,y,z) = (0, -L, 0)$. If $\tilde{\underline{E}}(\beta)$ denotes the fields of the traveling wave line source of Equation (A-1) and $\underline{E}$ represents the fields of the current element of Equation (A-28), then

$$\underline{E} = \frac{1}{2\pi} \int_{-\infty}^{\infty} \tilde{\underline{E}}(\beta) e^{j\beta z} \, d\beta \, . \qquad \text{(A-29)}$$

Since $\tilde{\underline{E}}(\beta)$ is an even function of β, Equation (A-29) becomes

$$\underline{E} = \frac{1}{\pi} \int_{0}^{\infty} \tilde{\underline{E}}(\beta) \cos \beta z \, d\beta \, . \qquad \text{(A-30)}$$

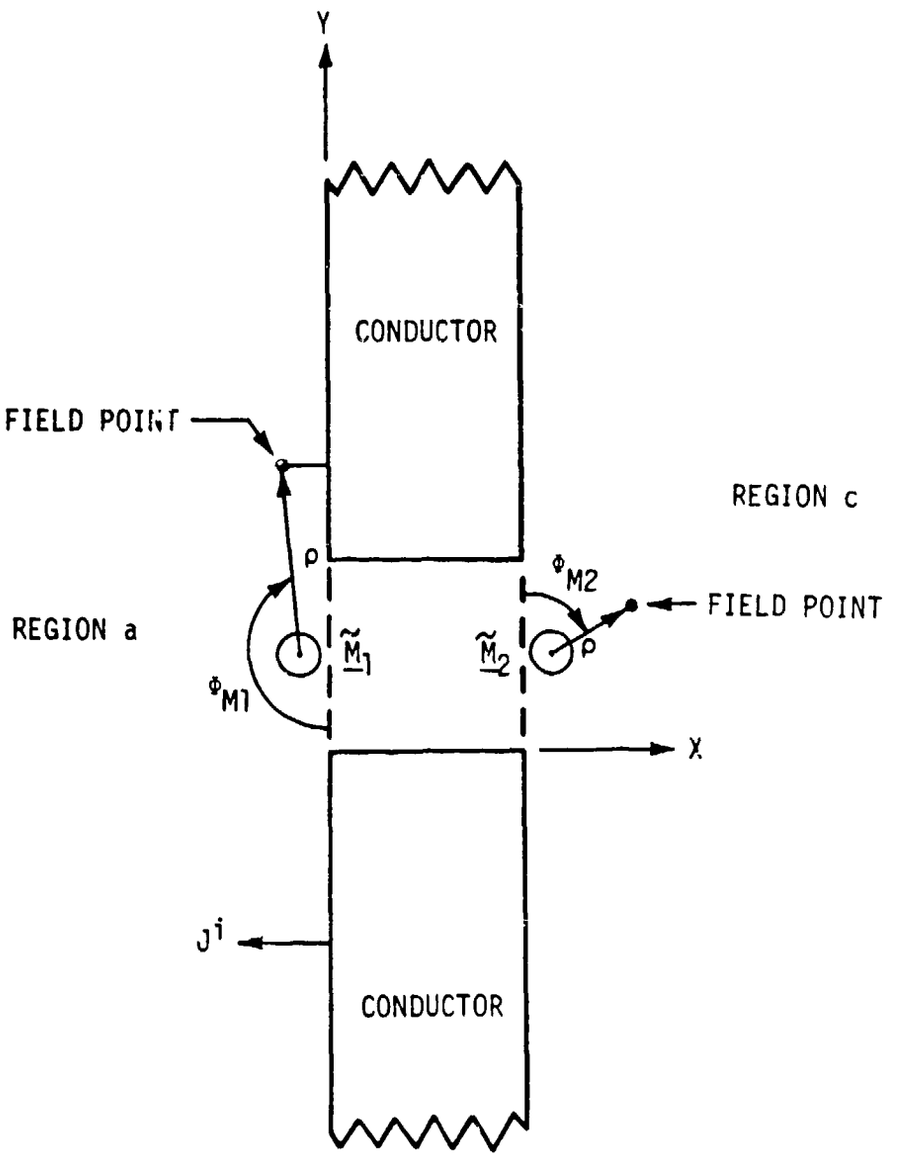

FIGURE A-2. DIRECTIONS OF Φ_{M1} AND Φ_{M2} AS DEFINED BY THE MAGNETIC CURRENT SOURCES

The integral in Equation (A-30) must be evaluated numerically. One difficulty in this numerical integration is that the integrand can have a singularity. Consider the simple situation where regions a, b, and c are composed of the same medium with parameters (μ, ε). The notation for this example becomes

k = medium wavenumber = $\omega\sqrt{\mu\varepsilon}$,

γ = waveguide propagation constant = $\sqrt{\beta^2-k^2}$,

$h = +\sqrt{k^2 - \beta^2}$, $\alpha = \sqrt{\beta^2 - k^2}$, and

$\tilde{Y}$ = admittance of aperture A_1 or aperture A_2 .

In this case, the transfer admittance of Equation (A-) becomes

$$\tilde{Y}_{12} = 2\tilde{Y} \cosh \gamma d + \tilde{Y}_o \left(1 + \frac{\tilde{Y}^2}{\tilde{Y}_o^2}\right) \sinh \gamma d \ . \qquad \text{(A-31)}$$

If $\beta = k$, then $\gamma = h = \alpha = 0$, and thus $\tilde{Y}$ and $\tilde{Y}_{12} = 0$. In this case, V_2 of Equation (A-24), V_1 of Equation (A-25), and $\underline{\tilde{E}}(\beta)$ of Equation (A-27) and (A-30) will be infinite. The singularity can be avoided by deforming the path of integration in the β plane from the positive real axis to the path shown in Figure A-3. In this situation the integral of Equation (A-30) can symbolically be written as

$$\int_o^\infty (\ ) \, d\beta = \int_o^{k-\delta} (\ ) \, d\beta + \int_C (\ ) \, d\beta + \int_{k+\delta}^\infty (\ ) \, d\beta \ . \qquad \text{(A-32)}$$

The integrals from 0 to $k-\delta$ and $k+\delta$ to infinity are sufficiently well behaved to be integrated numerically, say via Simpson's rule. The integral over the half circle C will be done analytically, employing small argument approximations.

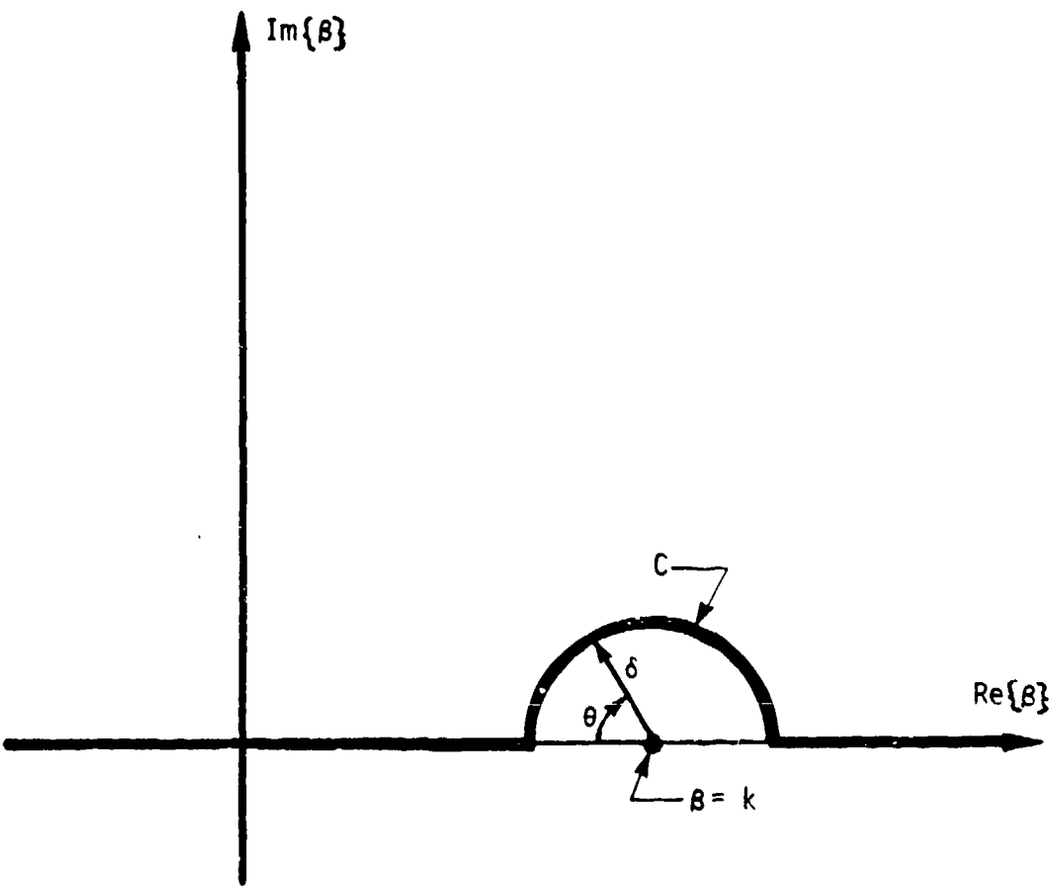

FIGURE A-3. PATH OF INTEGRATION IN THE β PLANE

The aperture admittance can be written as

$$\tilde{Y} = Ch^2(\pi - j2\ \ln[ahw]) \tag{A-33}$$

where $C = 1/(2\ \omega\mu\pi)$ and $a = 0.223$. On the contour C

$$\beta = k + \delta e^{j(\pi-\theta)} = k - \delta e^{-j\theta} \qquad 0 \leq \theta \leq \pi\ . \tag{A-34}$$

Note that h can be written as

$$h = \sqrt{k^2 - \beta^2} = \sqrt{(k + \beta)(k - \beta)}\ . \tag{A-35}$$

On C, if $\delta << k$,

$$\begin{aligned} k + \beta &\simeq 2k \\ k - \beta &\simeq \delta e^{-j\theta} \quad \text{and} \end{aligned} \tag{A-36}$$

$$h = \sqrt{(2k)(\delta e^{-j\theta})} = \sqrt{2k\delta}\ e^{-j\theta/2}\ . \tag{A-37}$$

Substitution of Equation (A-37) into Equation (A-33) yields

$$\tilde{Y} = 2Ck\delta\ e^{-j\theta}\ \left[\pi - \theta - j2\ \ln\left\{aw\sqrt{2k\delta}\right\}\right] \tag{A-38}$$

Upon substitution of Equation (A-38) into Equation (A-31) with small argument assumptions, the following results are obtained

$$\tilde{Y}_{12} = Ae^{-j\theta}\ [\theta + B] \quad \text{where} \tag{A-39}$$

$$\begin{aligned} A &= -2\xi\delta/\pi \\ B &= -\pi + j\left(2\ \ln\left\{aw\sqrt{2k\delta}\right\} - \frac{\pi d}{w}\right) \\ \xi &= k/\omega\mu\ . \end{aligned} \tag{A-40}$$

In obtaining Equation (A-39) we dropped terms of order δ^2 and used the approximations $\sinh\gamma d \simeq \gamma d$ and $\cosh\gamma d \simeq 1$ for $\gamma d << 1$, and $\gamma \simeq j\sqrt{2k\delta}\ e^{-j\theta/2}$.

Using the small argument approximation

$$H_1^{(2)}(z) \sim \frac{j2}{\pi z} \quad \text{as } z \to 0 , \quad \text{and} \tag{A-41}$$

$\tilde{I}^i$ of Equation (A-23) becomes

$$\tilde{I}^i \simeq -1/\pi L . \tag{A-42}$$

In this case, V_2 of Equation (A-23) becomes

$$V_2 = \frac{\tilde{I}^i}{\tilde{Y}_{12}} \simeq \frac{(-1/\pi L)}{\tilde{Y}_{12}} . \tag{A-43}$$

Inserting Equation (A-43) into (A-27) and using Equation (A-41) for the Hankel function yields

$$\underline{\tilde{E}} = \frac{1}{\pi^2 \rho L \tilde{Y}_{12}} \hat{\phi} \quad \text{or} \tag{A-44}$$

$$\underline{\tilde{E}} = \frac{De^{j\theta}}{\theta+B} \hat{\phi} \tag{A-45}$$

where

$$D = -\frac{1}{\pi^2 \rho L A} = -1/(2\pi\rho L \xi \delta) . \tag{A-46}$$

Inserting Equation (A-45) into A-30), but considering only that portion of the integral over the contour C yields

$$\underline{E}^C = \frac{\hat{\phi}_{\text{MI}}}{\pi} \int_C \frac{De^{j\theta}}{\theta+B} \cos\beta z \, d\beta \tag{A-47}$$

where

$$\beta = k - \delta e^{-j\theta} \rightarrow d\beta = j\delta e^{-j\theta} \, d\theta . \tag{A-48}$$

Since $\cos \beta z \approx \cos kz$, Equation (A-47) can be written as the θ integration

$$\underline{E}_c = \frac{D \cos kz}{\pi} \hat{\phi}_{M1} \int_0^{\pi} \frac{e^{j\theta}}{\theta+B} j\delta e^{-j\theta} \, d\theta \quad , \tag{A-49}$$

$$\underline{E}_c = j \frac{\delta D}{\pi} \cos kz \, \hat{\phi}_{M1} \int_0^{\pi} \frac{d\theta}{\theta+B} \, . \tag{A-50}$$

Equation (A-48) can now be integrated to yield

$$\underline{E}^c = E\hat{\phi}_{M1} [\ln\{\pi+B\} - \ln\{B\}] \quad , \tag{A-51}$$

where

$$E = - \frac{j \cos kz}{2\rho L \xi \pi^2} \, . \tag{A-52}$$

APPENDIX B.

MOMENT METHOD ANALYSIS OF TWO MONOPOLES NEAR A SLIT IN A GROUND PLANE

APPENDIX B. MOMENT METHOD ANALYSIS OF TWO MONOPOLES NEAR A SLIT IN A GROUND PLANE

The purpose of the moment method program was to determine the transfer characteristic of two monopoles positioned normal to a thin ground plane, as shown in Figure B-1. The ground plane contained a crack perpendicular to the line connecting the two monopoles. The monopoles had a length of L_o and radius of a, where $a<<\lambda$. The monopoles and the ground plane were modeled as two dipoles of length $L = 2L_o$ radiating into free space. The distance between the dipoles was d, where $d>\lambda$. The first dipole was driven by a 1-volt magnetic frill of radius b located at its center. The program used the method of moments with point matching and pulse basis functions to find the current at discrete points on the axis of both dipoles and the crack. The currents at the center of each dipole were used to find the transfer characteristic of the dipoles.

The dipoles were assumed to have a large length to diameter ratio and to be perfect conductors. Since $a<<\lambda$, only currents in the $\hat{z}$ direction were present. The field at each dipole was equal to the sum of the scattered component, E_z^s, and the incident component, E_z^i, where the scattered component was the field scattered from the wires and the incident component was the field from the magnetic frill. Since the total field must be zero on the surface and in the interior of a perfectly conducting wire,

$$E_z^s = - E_z^i$$

or

$$\int_{-L/2}^{+L/2} I(z')K(z,z')dz' = - E_z^i \quad , \tag{B-1}$$

where $K(z,z')$ is the kernel given by

$$K(z,z') = \frac{1}{j\omega\varepsilon_o} \frac{e^{-jkR}}{4\pi R^5} [(1+jkR)(2R^2-3a^2) + (kaR)^2]$$

$$R = \sqrt{(x-x')^2 + (y-y')^2 + (z-z')^2}$$

according to Pocklington's equation[13]. $K(z,z')$ gives the scattered field at a point z due to a unit basis current element at the point z'.

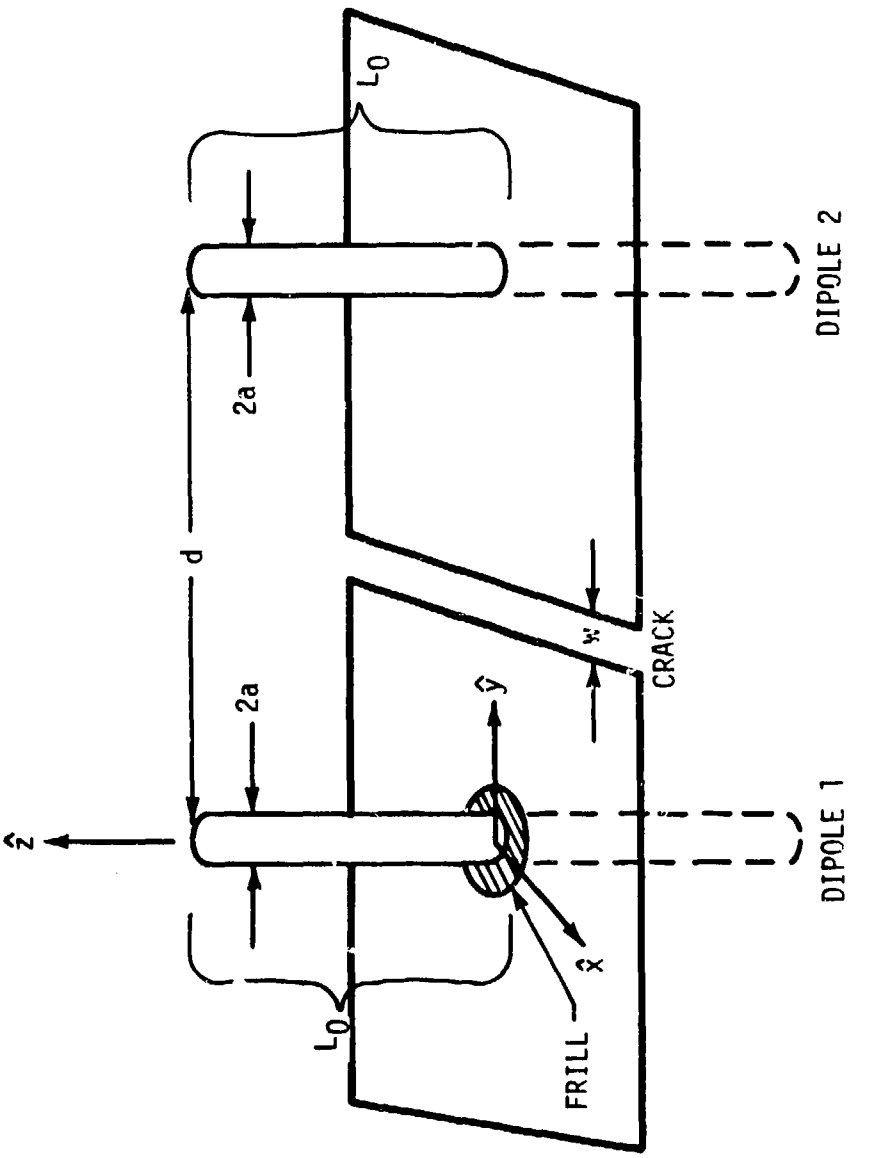

FIGURE B-1. TWO MONOPOLES NEAR A SLIT IN A GROUND PLANE

The program first calculated the current distribution on dipole 1. The method of moments was used to change Equation (B-1) to a system of simultaneous linear algebraic equations, where the I_n's were the unknowns. The dipole was divided into N segments which were each $\Delta z'_n$ long, and the current was given by

$$I(z') = \sum_{n=1}^{N} I_n g_n(z'_n),$$

where $g_n(z')$ are the unit basis functions:

$$g_n(z') = \begin{cases} 1 & z' \text{ in } \Delta z'_n \\ 0 & \text{elsewhere} \end{cases}.$$

Equation (1) then became:

$$\int_{-L/2}^{L/2} I(z')K(z,z')\,dz' = \int_{-L/2}^{L/2} \sum_{n=1}^{N} I_n g_n(z')K(z_m,z')\,dz'$$

$$= \sum_{n=1}^{N} I_n \int_{\Delta z'_n} K(z_m,z)\,dz = -E_z^i(z_m) . \qquad \text{(B-2)}$$

Point matching was used to enforce Equation (B-2) at N points, z_m, on the surface of the dipole. The result was a system of equations of the form:

$$[Z_{mn}][I_n] = [V_m]$$

$[Z_{mn}]$ was an N by N Toeplitz matrix given by:

$$Z_{mn} = \int_{\Delta z'_n} \frac{e^{-jkR}}{(j\omega\varepsilon_o)(4\pi R^5)} [(1+jkR)(2R^2-3a^2) + (kaR)^2]\,dz' \qquad \text{(B-3)}$$

where

$$R = \sqrt{(z_m-z'_n)^2 + a^2}$$

$\Delta z'_n$ = length of segment containing z'_n.

Simpson's Rule was used to perform all the required integrations. The vector $[I_n]$ contained the amplitudes of the current basis functions at each point z_n. The vector $[V_m]$ was equal to $[-E^i_{z_m}]$, where $E^i_{z_m}$ was the incident field at z_m due to the disk-shaped magnetic frill of radius b around the middle of dipole 1.

$$E^i_{z_m} = \frac{1}{2\ln(b/a)} \left[\frac{e^{-jkR_1}}{R_1} - \frac{e^{-jkR_2}}{R_2} \right] . \qquad (B-4)$$

where

$$R_1 = \sqrt{a^2 + z_m^2}$$

$$R_2 = \sqrt{b^2 + z_m^2} \quad .$$

Once the program calculated $[Z_{mn}]$ and $[V_m]$, the currents were found using a program from Stutzman and Thiele[14] to invert the matrix $[Z_{mn}]$ and calculate $[I_n] = [Z_{mn}]^{-1} [V_m]$. If the two dipoles were not identical, the impedance matrix of dipole 2 and the currents on dipole 2 due to a 1 volt magnetic frill at its center were calculated in the same manner as for dipole 1.

In order to find the currents $[I_p]$ on the second dipole due to a frill on dipole 1, dipole 1, and the crack, the method of moments was used again to get an equation of the form $[Z_{mp}][I_p] = [V_m]$. $[Z_{mp}]$ was the impedance matrix for dipole 2. The vector $[V_m]$ was equal to $[-E^{i'}_{z_m}]$, where $E^{i'}_{z_m}$ was the incident field at the mth point on the axis of dipole 2 due to the first dipole, the magnetic frill, and the crack.

The field at a point on the axis of dipole 2 due to segment Δz_n of dipole 1 was equal to $d\vec{E}_n$.

$$\vec{dE}_n = \left\{ \frac{60 I_n \Delta z_n}{R^2} \left(\frac{z-z_n}{R}\right) \left[1 + \frac{1}{jkR}\right] e^{-jkR} \right\} \hat{r} + \left\{ \frac{j60\pi I_n \Delta z_n}{R} \left(\frac{y-y_n}{R}\right) \left[1 + \frac{1}{j2\pi R} - \frac{1}{(2\pi R)^2}\right] e^{-jkR} \right\} \hat{\theta} \quad \text{(B-5)}$$

where

$$R = \sqrt{(x-x_n)^2+(y-y_n)^2+(z-z_n)^2}$$

$$\theta = \tan^{-1}\left(\frac{y-y_n}{z-z_n}\right).$$

(x,y,z) was a point on dipole 2 and (x_n, y_n, z_n) was a point in the center of the nth segment of dipole 1. The $\hat{z}$ component was $dE_{n_z} = dE_{n_r} \cos\theta - dE_{n_\theta} \sin\theta$. Therefore the field due to all N segments of dipole equaled $\sum_{n=1}^{N} dE_{n_z}$.

The field at a point (x,y,z) due to the magnetic frill was derived using standard equations given by Harrington [15] and was found to be

$$\vec{E}' = \left\{ \frac{jk(b^2-a^2)}{4R^2 \ln(b/a)} \left(\frac{z}{R}\right) \left[1 + \frac{1}{kR}\right] e^{-jkR} \right\} \hat{r} + \left\{ \frac{-k^2(b^2-a^2)}{8R\ln(b/a)} \left(\frac{y}{R}\right) \left[1 + \frac{1}{jkR} - \frac{1}{(kR)^2}\right] e^{-jkR} \right\} \hat{\theta}, \quad \text{(B-6)}$$

where

$$R = \sqrt{x^2+y^2+z^2}$$

$$\theta = \tan^{-1}\left(\frac{y}{z}\right).$$

Only the $\hat{z}$ component, $E'_z = E'_r \cos\theta - E'_\theta \sin\theta$, was needed, so the total field at a point (x,y,z) due to dipole 1 and the frill was

$$E_z = \sum_{n=1}^{N} dE_{n_z} + E'_z .$$

Using this definition for the $\hat{z}$ component of the field, dipole 2 was divided into N segments of length Δz_m and E_z was evaluated at each point z_m at the center of each segment of dipole 2 to get $\left[E_{z_m}\right]$.

The crack was modeled by placing a magnetic surface current in the aperture. The crack structure divided space into two half spaces (i.e., $z>0$ and $z<0$). For $z>0$, a surface current $\vec{M}$ was assumed to exist in the crack aperture, and the surface current radiated in the presence of an infinite ground plane. For $z<0$, a surface current $-\vec{M}$ was assumed. By using $\vec{M}$ for $z>0$ and $-\vec{M}$ for $z<0$, the tangential $\vec{E}$ field was forced to be continuous. The amplitude and distribution of $\vec{M}$ were unknowns and were determined by enforcing the boundary condition that tangential $\vec{H}$ must be continuous in the aperture.

The crack width was assumed to be small with respect to a wavelength. This assumption implied that the surface current $\vec{M}$ was entirely in the $\hat{x}$ direction. The magnetic current $\vec{M} = M(x)\hat{x}$ inside the crack was divided into N segments of length Δx_n. Then

$$M(x) = \sum_{n=1}^{N} M_n g_n(x) ,$$

where

$$g_n(x) = \begin{cases} 1 & x \text{ in } \Delta x_n \\ 0 & \text{elsewhere.} \end{cases}$$

The method of moments and point matching were used to find the amplitudes M_n of the pulse basis functions $g_n(x)$. After imposing the boundary condition that H_{tan} is continuous from $z = 0^+$ to $z = 0^-$ in the aperture, the resulting system of equations was

$$[H_{mn}][M_n] = [-1/2\ H^i_{x_m}] .$$

$[H_{mn}]$ was an N by N Toeplitz matrix given by:

$$H_{mn} = \frac{M_n \Delta x_n}{2\pi\eta} \int_{-w/2}^{w/2} e^{-jkR} \left[\left(\frac{1}{R^2} + \frac{1}{jkR^3} \right) \cos^2\theta - \frac{1}{2} \left(\frac{jk}{R} + \frac{1}{R^2} + \frac{1}{jkR^3} \right) \sin^2\theta \right] dy$$

for $m \neq n$

$$H_{mn} = \frac{jM_n}{\pi\eta} \left[\frac{1}{k} \frac{b}{a\sqrt{b^2+a^2}} - k \left(a \ln \left(\frac{b+\sqrt{b^2+a^2}}{a} \right) + b \ln \left(\frac{a+\sqrt{b^2+a^2}}{b} \right) \right) \right] \qquad \text{(B-7)}$$

for $m=n$

where $R = \sqrt{(x_m-x_n)^2+y^2}$

$\theta = \tan^{-1} \frac{y}{x_m-x_n}$

$2b$ = length of crack

$2a = w$ = width of crack.

$H^i_{x_m}$ was the $\hat{x}$ component of the incident field at the point x_m in the crack due to dipole 1.

$$H^i_{x_m} = \sum_{n=1}^{N} \frac{I_n \Delta z_n}{4\pi} e^{-jkR} \left(\frac{jk}{R} + \frac{1}{R^2} \right) \frac{D+w/2}{R} , \qquad \text{(B-8)}$$

where

(x_m, y_m, z_m) = point in center of mth segment of crack

(x_n, y_n, z_n) = point in center of nth segment of dipole 1

D = distance from dipole 1 to crack

w = width of crack

$R = \sqrt{(x_m-x_n)^2 + (y_m-y_n)^2 + (z_m-z_n)^2}$.

The program calculated $[H_{mn}]$ and $[-1/2\ H^{i}_{x_m}]$ and solved the system of equations $[H_{mn}][M_n] = [-1/2\ H^{i}_{x_m}]$ for $[M_n]$ using the same routine it used to solve for $[I_n]$ of dipole 1.

The program then used the magnetic currents $[M_n]$ in the crack to find the field on the axis of dipole 2 due to the crack. The z component of the field at any point (x,y,z) due to the nth segment of the crack was

$$E_{\phi_{z_n}} = \int_{-w/2}^{w/2} \frac{-jkM_n\,dy\Delta x_n}{4\pi R} \left(\frac{y-y_n}{R}\right) \left[1+\frac{1}{jkR}\right] e^{-jkR}\,, \qquad \text{(B-9)}$$

where

Δx_n = length of nth segment of crack

$R = \sqrt{(x-x_n)^2 + (y-y_n)^2 + (z-z_n)^2}$.

The total field at (x,y,z) due to the crack was $E_z'' = \sum_{n=1}^{N} E_{\phi_{z_n}}$.

Finally, the total incident field at a point z_m on the axis of dipole 2 was

$$E^{i'}_{z_m} = E_{z_m}'' + E_{z_m} .$$

Setting $[V_m] = [-E^{i'}_{z_m}]$, the program solved the system of equations $[Z_{mp}][I_p] = [V_m]$ for $[I_p]$.

With the currents on dipole 1 and dipole 2 known for a 1-volt source, the transfer characteristic was calculated.

MEASURED VERSUS PREDICTED TIME DOMAIN RESPONSE

The time domain response of one antenna due to a voltage pulse on another antenna was measured and predicted. The input pulse applied to the transmitting antenna and the output pulse at the receiving antenna were both measured with an oscilloscope (see Figures B-2 and B-4). The shape of the output pulse was predicted by calculating the transfer coefficient S_{21} of the two antennas for each frequency used in a Fourier series of the input pulse function. The shape of the input pulse was approximated by a combination of triangular and square pulses to get the input pulse function f(t). To predict the output pulse the input pulse function f(t) was expressed as the real part of a sum of functions $e^{j\omega_n t}$ with coefficients a_n, i.e.,

$$f(t) = \mathrm{Re}\left[\sum_{n=o}^{N} a_n e^{j\omega_n t}\right] \quad , \tag{B-10}$$

where

$$\omega_n = 2\pi f_n = \frac{2\pi n}{T}$$

T = period

$n = 0,1,2...N$.

Since

$$\mathrm{Re}\left[\sum_{n=o}^{N} a_n e^{j\omega_n t}\right] = \sum_{n=o}^{N} a_n \cos\omega_n t \quad ,$$

the coefficients a_n are the Fourier coefficients:

$$a_n = \frac{2}{T}\int_o^T f(t)\cos\omega_n t\,dt \quad .$$

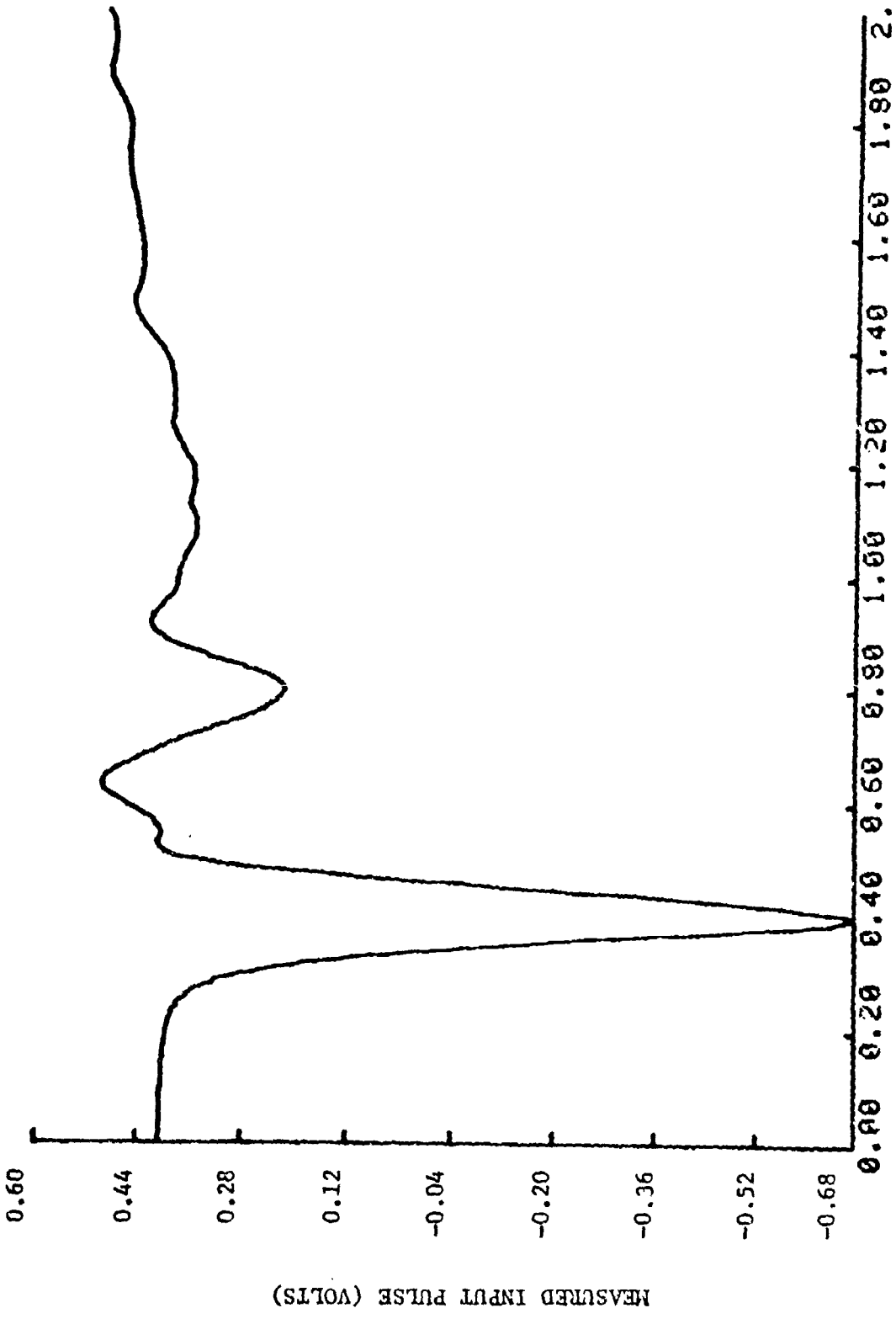

FIGURE B-2. MEASURED INPUT PULSE
T = 1.5 ns, N = 30

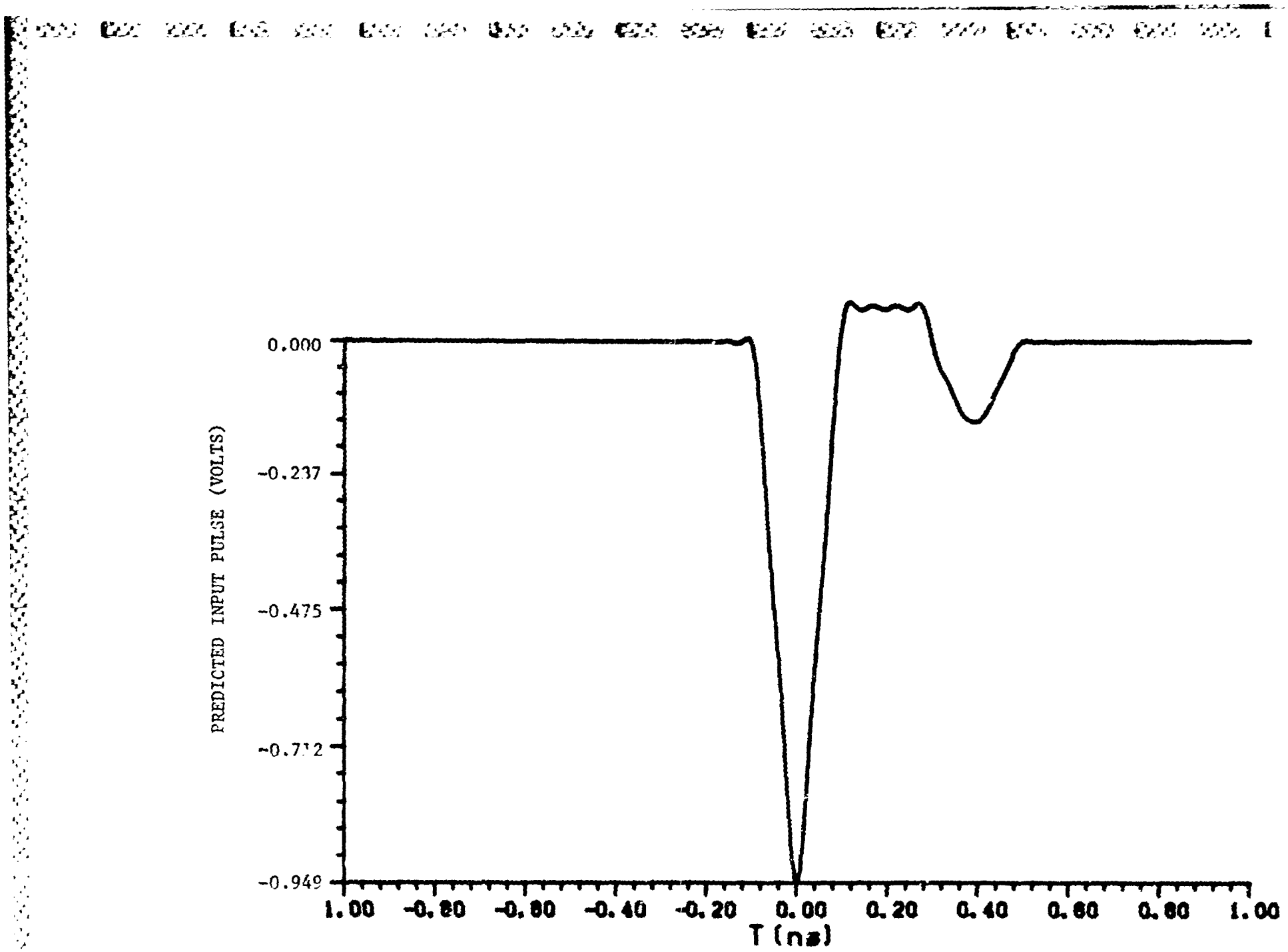

FIGURE B-3. PREDICTED INPUT PULSE
T = 1.5 ns, N = 30

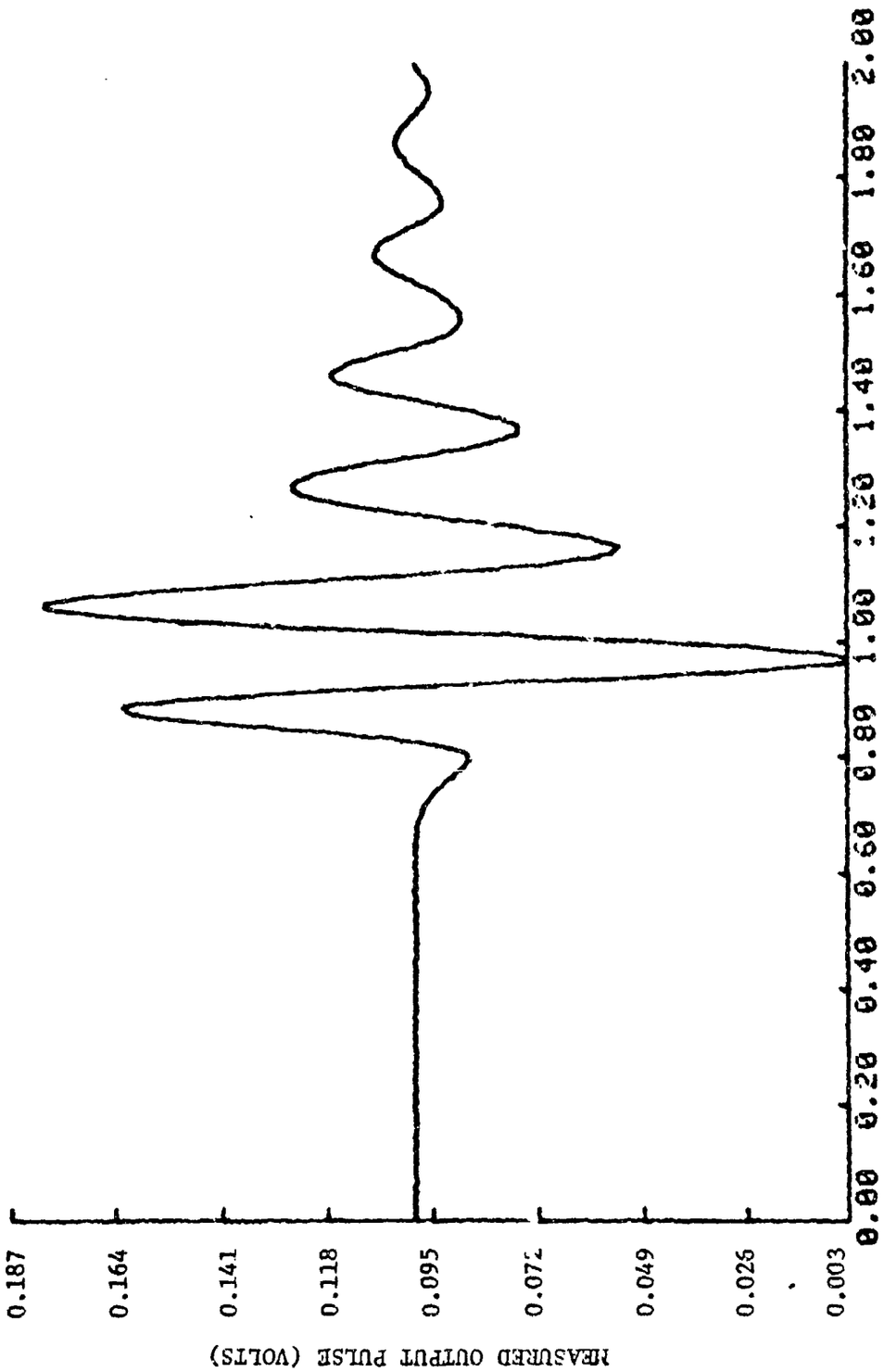

FIGURE B-4. MEASURED OUTPUT PULSE FOR TWO ONE-HALF INCH ANTENNAS

Once the input pulse was expressed as a Fourier series, the transfer coefficients S_{21_n} were calculated for the two antennas according to the moment method for each frequency f_n. The output pulse function was calculated by multiplying each Fourier coefficient of the input pulse function by the transfer coefficient S_{21_n}, summing the series, and taking the real part, i.e.,

$$f_{out}(t) = \mathrm{Re}\left[\sum_{n=1}^{N} \left| S_{21_n} \right| a_n e^{j(\omega_n t + \theta_n)}\right] , \qquad \text{(B-11)}$$

where

$$S_{21_n} = \left| S_{21_n} \right| e^{j\theta n} .$$

The time domain response was measured for two cases. In Case 1 the two antennas were both 1/2-inch long. In Case 2, one antenna was 1/2-inch long and the other was 1 inch long. The input pulse for both cases was modeled with a 1.5 ns period and 30 terms of the Fourier series (see Figure B-3). The measured and predicted output pulses for both cases showed good agreement (see Figures B-4 through B-7).

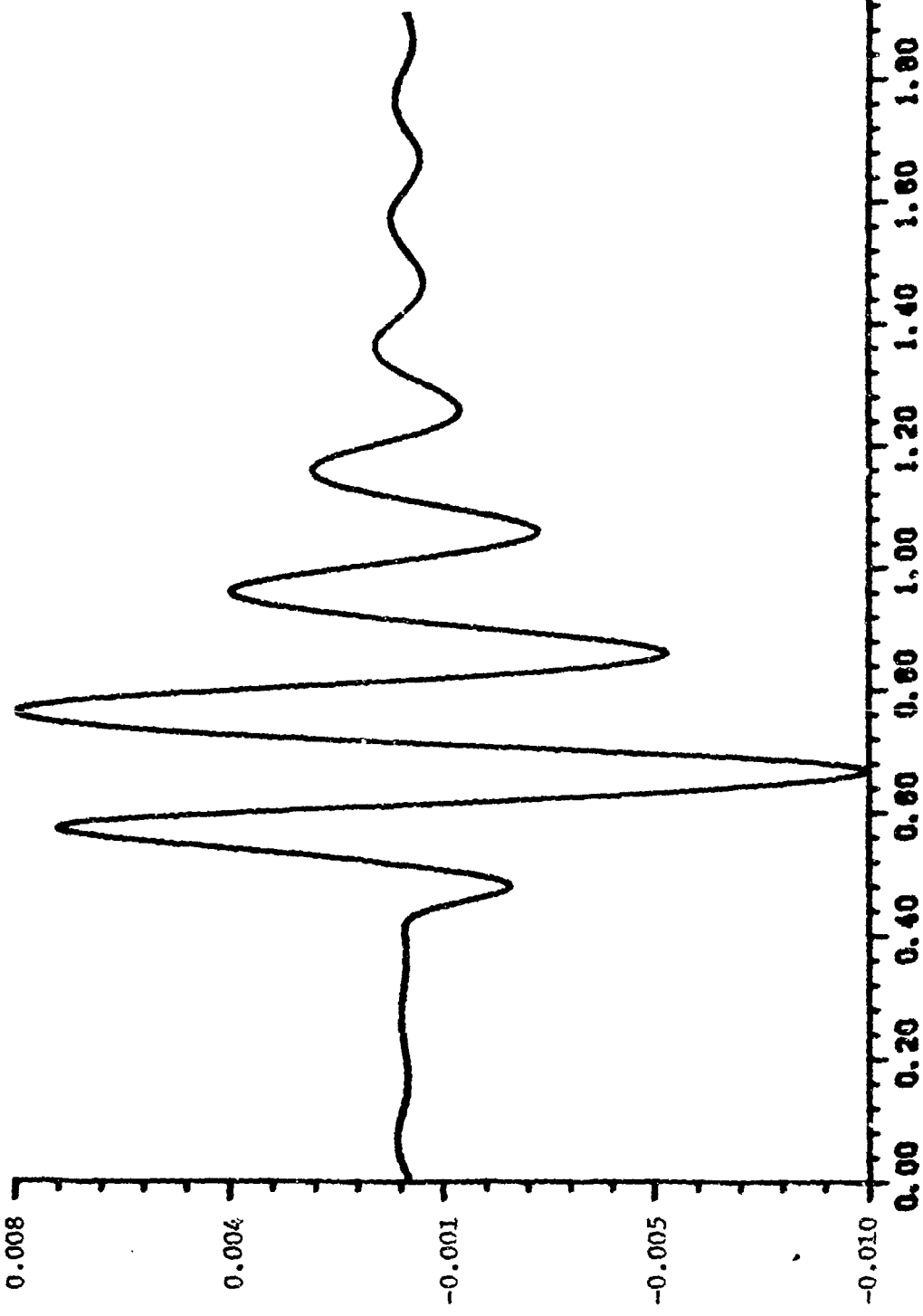

FIGURE B-5. PREDICTED OUTPUT PULSE FOR TWO ONE-HALF INCH ANTENNAS

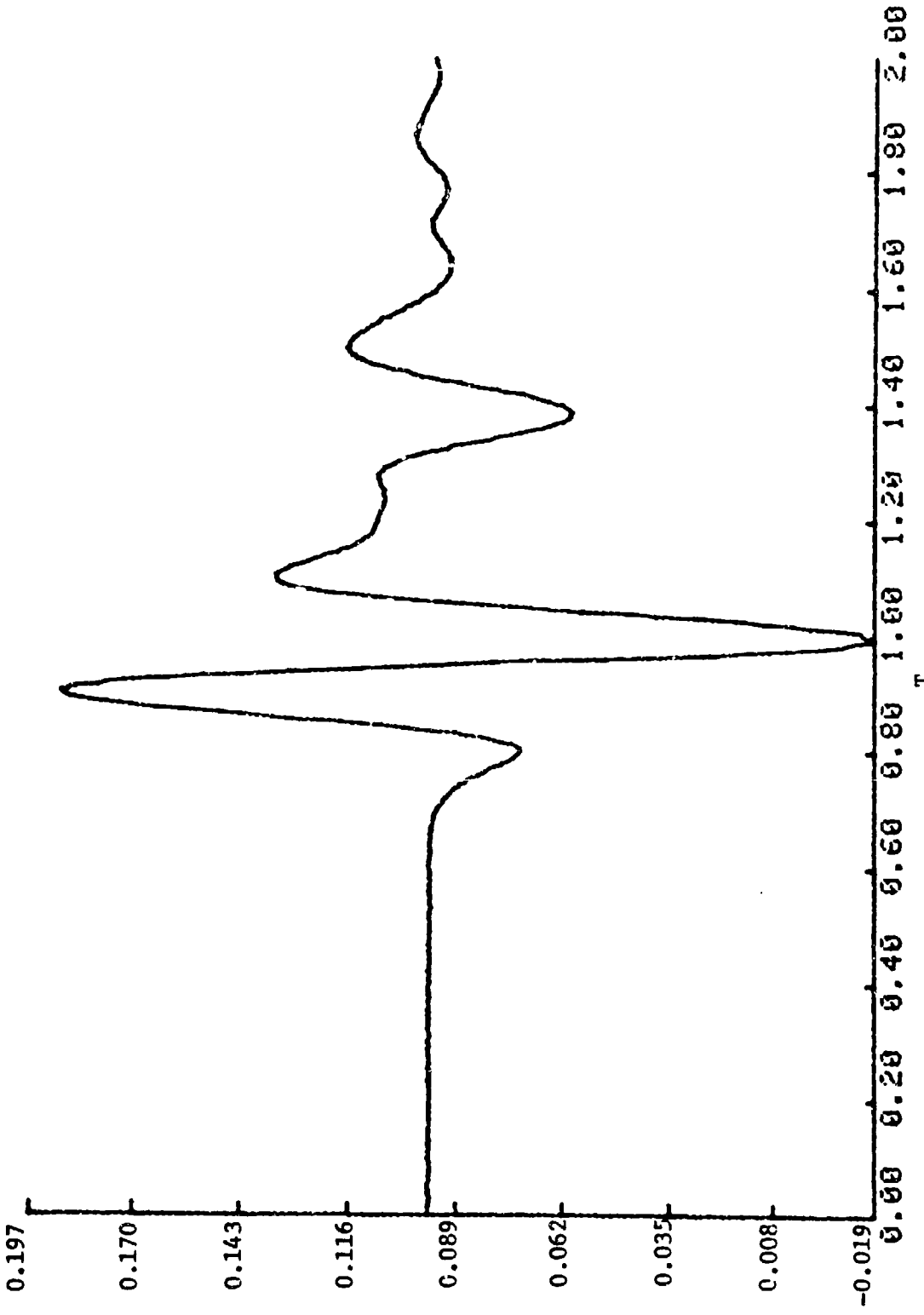

FIGURE B-6. MEASURED OUTPUT PULSE FOR ONE-HALF INCH ANTENNA AND ONE INCH ANTENNA

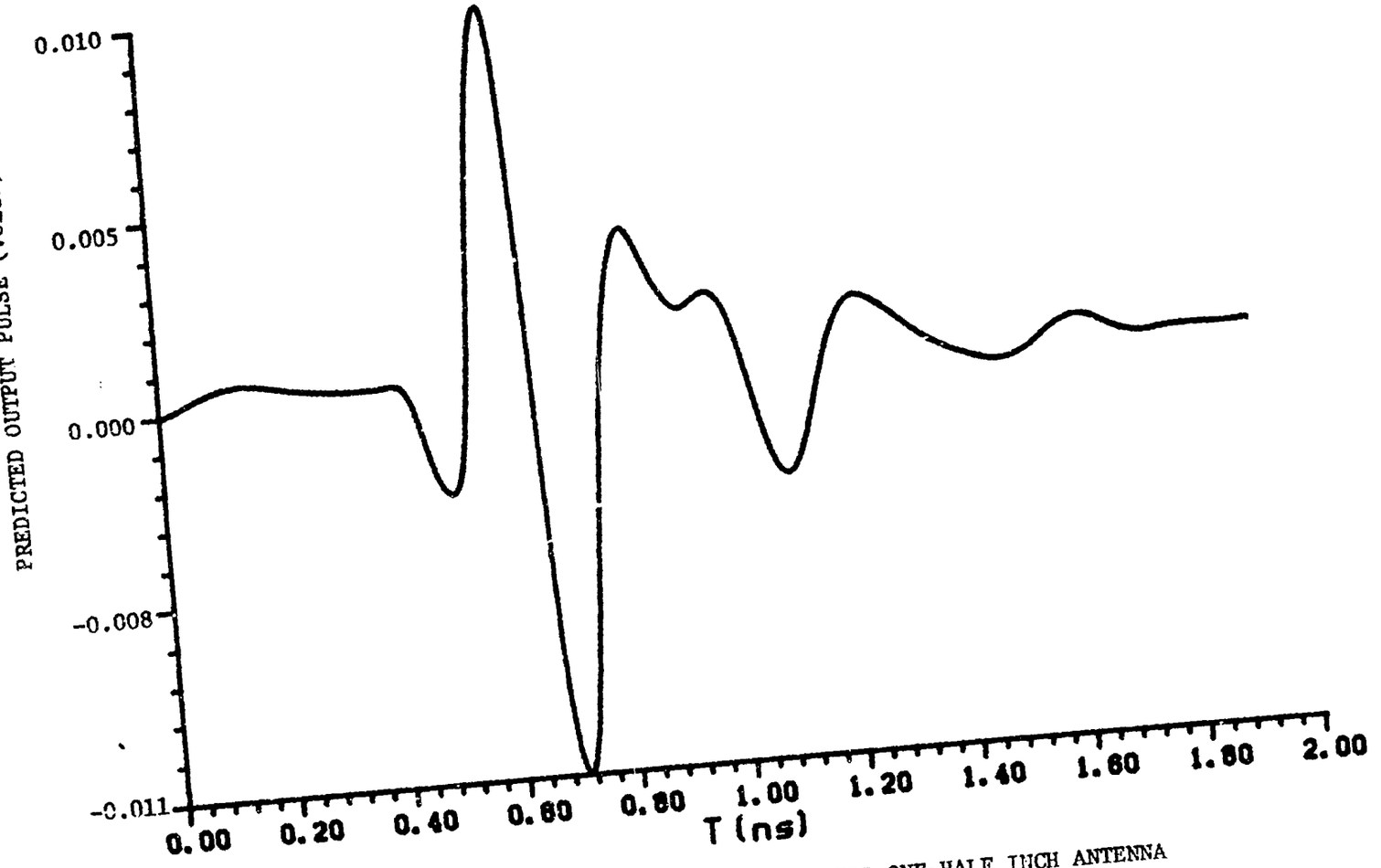

FIGURE B-7. PREDICTED OUTPUT PULSE FOR ONE-HALF INCH ANTENNA AND ONE INCH ANTENNA

APPENDIX C

TRANSIENT RADIATION OVER A GROUND PLANE AND BETWEEN TWO PARALLEL PLATES

APPENDIX C. TRANSIENT RADIATION OVER A GROUND PLANE AND BETWEEN TWO PARALLEL PLATES

I. TRANSIENT RADIATION OVER A GROUND PLANE

In this section we consider the signal received by a small probe antenna when the source of radiation is a short vertical current element with impulsive time behavior. It is assumed that the highest frequency components present in the current waveform are such that the probe antenna used for receiving is short relative to a wavelength ($\ell < 0.15\ \lambda_0$). This allows one to characterize the probe by its capacitive reactance since the radiation resistance is small by comparison. Figure C-1 shows the physical arrangement assumed. The ground plane is chosen so large that reflection from its sides is delayed long enough for the direct transmitted pulse signal to be received without interference.

The problem is solved using the following steps: The solution is first derived for steady sinusoidal fields with $e^{j\omega t}$ time dependence. This solution is obtained using image theory and the well known results for the field radiated by a short current filament. The open circuit received voltage is calculated by the expression

$$V_{oc} = -\frac{1}{I_{in}} \int_V I\ E\ dV \qquad \text{(C-1)}$$

where E is the vertical field produced by the probe antenna when it is radiating with an input current I_{in}. Equation (C-1) comes from an application of reciprocity and gives V_{oc} in terms of the interaction of the radiated field with the current I whose signal we wish to find when the probe is used for receiving. When the initial conditions are zero we can replace $j\omega$ by the Laplace transform variable s to obtain the Laplace transform of the solution. The inversion of this transform will give the time domain solution.

When the probe is used for transmitting the current on the probe is triangular, falling linearly from I_{in} to zero at the end, since the probe is short compared to all wavelengths present. The total radiated electric field in the vertical direction along the ground plane is

$$E = -\frac{jk_0 Z_0 I_{in} \ell}{4\pi} \left(\frac{1}{r} + \frac{1}{jk_0 r^2} - \frac{1}{k_0^2 r^3}\right) e^{-jk_0 r} \qquad \text{(C-2)}$$

We now replace $j\omega$ by s, i.e., jk_0 by s/c, to obtain ($c = 3 \times 10^8$ m/s is the speed of light propagation)

$$V_{oc}(s) = \frac{Z_0 \ell \ell_e}{4\pi} \left(\frac{s}{cr} + \frac{1}{r^2} + \frac{c}{sr^3}\right) e^{-(sr)/c} I(s) \qquad \text{(C-3)}$$

upon application of (C-1) and letting $I(s)$ be the Laplace transform of $i(t)$, the radiating current element with effective length ℓ_e.

The receiving circuit is shown in Figure C-2. Since the radiation resistance R is very small, the output voltage $V_0(s)$ is given by

$$V_0(s) = \frac{Z_c V_{oc}(s)}{Z_c + \frac{1}{sC}} = \frac{CZ_c s V_{oc}(s)}{1 + CZ_c s} \qquad \text{(C-4)}$$

where Z_c is the characteristic impedance of the coaxial line and C is the probe capacitance.

In the inverse Laplace transform a factor s in the numerator is equivalent to a time derivative. Hence, for $sV_{oc}(s)$ we obtain, in the time domain,

$$\frac{dv_{oc}(t)}{dt} = \frac{Z_0 \ell \ell_e}{4\pi} \left(\frac{1}{cr}\frac{d^2}{dt^2} + \frac{1}{r^2}\frac{d}{dt} + \frac{c}{r^3}\right) \frac{1}{2\pi j} \int_C e^{st - sr/c} I(s) ds \qquad \text{(C-5)}$$

The inverse transform in this equation is simply $i(t-r/c)$ which is the time delayed current waveform.

Consider the equation

$$\frac{V(s)}{s + a} = V_a(s) \qquad \text{(C-6a)}$$

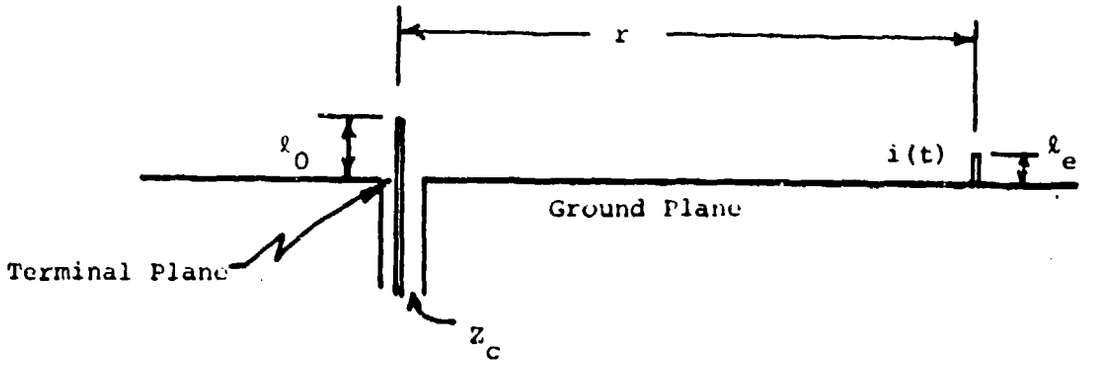

Figure C-1. Transient radiating current and receiving probe.

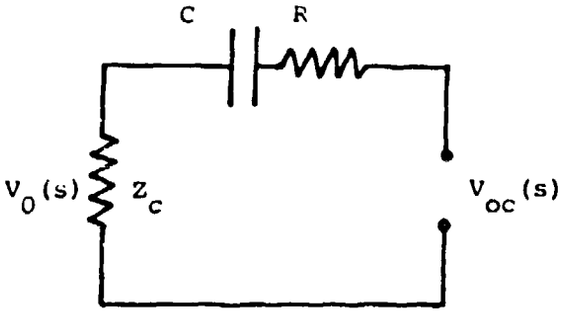

Figure C-2. Equivalent probe receiving circuit. Radiation resistance R is much smaller than Z_c.

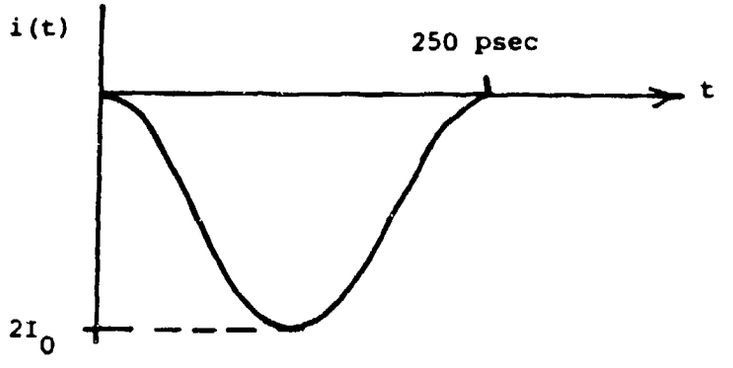

Figure C-3. Assumed current pulse.

or

$$(s + a)\ V_a(s) = V(s) \tag{C-6b}$$

In the time domain this is the differential equation

$$\left(\frac{d}{dt} + a\right)\ v_a(t) = v(t) \tag{C-6c}$$

This equation can be integrated by multiplying by the integrating factor e^{at} and noting that

$$e^{at}\ \left(\frac{d}{dt} + a\right)\ v_a(t) = \frac{d}{dt}\ [e^{at}\ v_a(t)].$$

Thus we obtain

$$v_a(t) = v_a(0)\ e^{-at} + e^{-at} \int_0^t e^{at'}\ v(t')\ dt' \tag{C-7}$$

as the solution of the system described by (C-6). We now apply this result to (C-4) and use (C-5) to obtain

$$v_0(t) = v_0(0)\ e^{-t/\tau} + \frac{Z_0 \ell_e}{4\pi}\ e^{-t/\tau} \int_0^t e^{t'/\tau}\ \left(\frac{1}{cr}\ \frac{d^2}{dt'^2} + \frac{1}{r^2}\ \frac{d}{dt'} + \frac{c}{r^3}\right) \cdot\ i(t' - r/c)\ dt' \tag{C-8}$$

since sV_{oc} transforms into dv_{oc}/dt as the applied signal at the input for the first order differential equation analogous to (C-6c). The time constant τ equals CZ_c. We can assume that there is no initial charge on C so that $v_0(0)$ is zero.

As a model for a typical pulse we will use

$$i(t) = -\ I_0\ (1 - \cos\ \omega_0 t), \quad 0 \leq t \leq \frac{2\pi}{\omega_0} \tag{C-9}$$

This pulse is shown in Figure C-3. For this pulse we have

$$\left(\frac{1}{cr}\frac{d^2}{dt'^2} + \frac{1}{r^2}\frac{d}{dt'} + \frac{c}{r^3}\right)\left(1 - \cos\omega_0(t' - r/c)\right)$$

$$= \frac{ck_0^2}{r}\cos\omega_0(t' - r/c) + \frac{ck_0}{r^2}\sin\omega_0(t' - r/c)$$

$$+ \frac{c}{r^3}\left(1 - \cos\omega_0\left(t' - \frac{r}{r}\right)\right) \qquad \text{(C-10)}$$

where $k_0 = \omega_0/c$. If the pulse duration $2\pi/\omega_0$ is short, say less than 250 picoseconds, then ω_0 is of order $8\pi \times 10^9$ or greater. The relative order of magnitude of the three terms in (C-10) is then $(4\pi^2/r\lambda_0^2)$, $(2\pi/r^2\lambda_0)$, and $1/r^3$. As long as r is greater than λ_0 which is of order 7.5 cm the first term will dominate. Thus we obtain

$$v_0(t) = -\frac{Z_0 \ell\ell_e I_0}{4\pi}\frac{ck_0^2}{r}e^{-t/\tau}\int_{r/c}^{t} e^{t'/\tau}\cos\omega_0(t' - r/c)\,dt' \qquad \text{(C-11)}$$

The lower limit has been replaced by r/c since $i(t - r/c)$ is zero when $t < r/c$. The maximum value of t in the integral is $r/c + 2\pi/\omega_0$. Since a typical probe that is a few centimeters long has a capacitance of only a fraction of a picofarad, the time constant τ is typically much shorter than the pulse duration. The integration in (C-11) can be performed to give

$$v_0(t) = -Z_0\frac{\tau c}{4\pi r}(k_0^2 \ell\ell_e)\frac{I_0}{1 + \omega_0^2\tau^2}\cdots$$

$$\begin{cases} \cos\omega_0(t - r/c) + \omega_0\tau\sin\omega_0(t - r/c) - e^{-(t-r/c)/\tau}, & \frac{r}{c} \le t \le \frac{r}{c} + \frac{2\pi}{\omega_0} \\ e^{-(t - r/c)/\tau}\left(e^{2\pi/\omega_0\tau} - 1\right), & t \ge \frac{r}{c} + \frac{2\pi}{\omega_0} \end{cases} \qquad \text{(C-12)}$$

For a typical set of parameters we will assume:

$2I_0$ = 10 ma = peak current

ℓ = 1 cm

ℓ_e = 3 mm

ω_0 = $8\pi \times 10^9$, pulse length = 250 picoseconds

C = 0.15 pfd

Z_c = 50 ohms

τ = 7.5 picoseconds, $\omega_0\tau = 0.06\pi = 0.188$

r = 30 cm

Z_0 = 377 ohms

r/c = 1000 picoseconds

The resultant received signal is sketched in Figure C-4. A peak signal voltage of nearly 0.25 millivolt is produced by a peak value of 10 ma for the radiating current. The incident electric field is related to the time derivative of the current pulse and hence is a sinusoidal pulse lasting for one period. The receiving circuit modifies this pulse as shown in Figure C-4 but it remains very nearly a sinusoidal pulse.

The waveform chosen for the radiating current was dictated by the desire to avoid step functions and impulse functions from occurring when the first and second time derivatives are taken. It also is a waveform for which the analysis is readily carried out. The analysis carried out above is similar to that made by Meadors and Poirier [16], and Peake, Meadors, and Poirier [17]. The main difference is that the finite time constant of the input circuit has been taken into account. This analysis was carried out primarily for the purpose of later comparison with the results for transient radiation between two parallel plates.

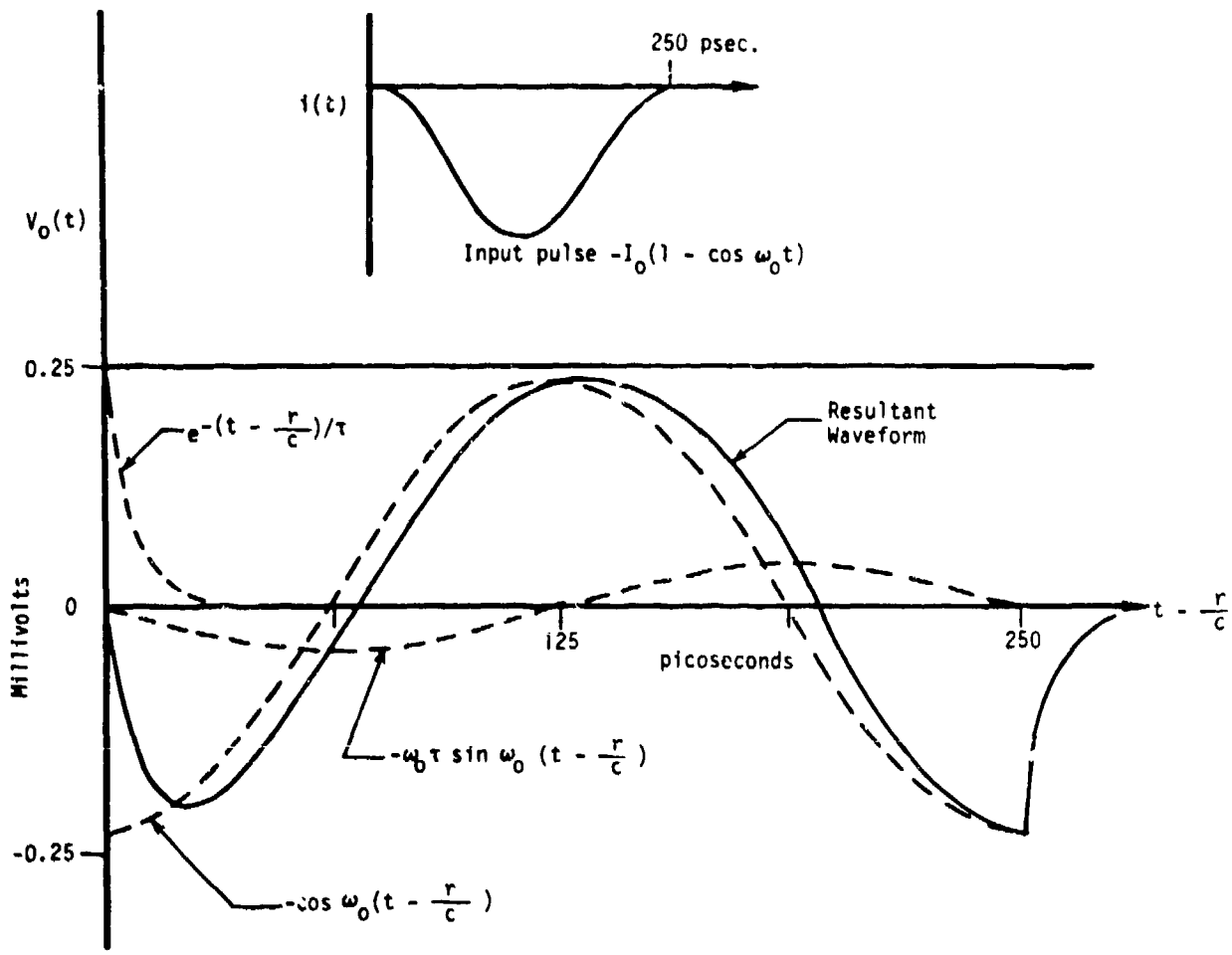

FIGURE C-4. RECEIVED SIGNAL FOR TRANSIENT RADIATION OVER A GROUND PLANE

II. TRANSIENT RADIATION BETWEEN PARALLEL PLATES

The configuration to be studied is shown in Figure C-5. It consists of a short impulsive current element radiating between two conducting plates with spacing b. The transient signal is received by a coaxial line probe. The spacing b is assumed to be small enough so that for all significant frequency components present in the signal only the dominant TEM field propagates.

When the probe is radiating it produces a vertical electric field that can be expressed as an infinite sum of modes of the form

$$E = \sum_{n=0}^{\infty} C_n \cos \frac{n\pi y}{b} H_0^2 \left(r\sqrt{k_0^2 - n^2\pi^2/b^2}\right) \qquad \text{(C-13)}$$

where H_0^2 is the Hankel function of the second kind. When $k_0 < n\pi/b$ this function decays exponentially so the higher order modes are evanescent. The dominant radiated mode is

$$E = C_0 H_0^2 (k_0 r)$$

The constant C_0 equals $-k_0 Z_0/4$ times the average current in the probe. When the spacing b is small the current in the probe is essentially uniform and equal to the input current I_{in} when the probe extends across to the upper plate as shown in Figure C-5. Thus the dominant radiated vertical electric field is

$$E = -\frac{k_0 Z_0}{4} I_{in} H_0^2 (k_0 r) \qquad \text{(C-14)}$$

Far from the probe the field is given by

$$E \sim -\frac{k_0 Z_0 I_{in}}{4} \sqrt{\frac{2j}{\pi k_0 r}} \; e^{-jk_0 r} \qquad \text{(C-15)}$$

The total radiated power is given by

$$2\pi rb \frac{|E|^2}{Z_0} = \frac{k_0 b Z_0}{4} |I_{in}|^2 \qquad \text{(C-16)}$$

The radiation resistance of the probe is the factor multiplying $|I_{in}|^2$, i.e.,

$$R = \frac{\pi b}{2\lambda_0} Z_0 \qquad \text{(C-17)}$$

and is much larger than that of a similar short probe radiating in free space. The probe reactance is inductive and is given approximately by the expression

$$X_L = Z_0 \frac{b}{\lambda_0} \ln \frac{2}{1.781 k_0 a} \qquad \text{(C-18)}$$

where a is the probe radius.

The open circuit received voltage when a current $I(\omega)$ of effective length ℓ_e is radiating is given by (C-1) and is

$$V_{oc} = \frac{k_0 Z_0}{4} I \ell_e H_0^2(k_0 r) \qquad \text{(C-19)}$$

In the Laplace transform domain the open circuit received voltage is

$$V_{oc}(s) = -j \frac{Z_0 I(s) \ell_e}{4c} s H_0^2(-js\, r/c) \qquad \text{(C-20)}$$

In the time domain we obtain

$$v_{oc}(t) = -j \frac{Z_0 \ell_e}{4c} \frac{d}{dt} \frac{1}{2\pi j} \int_C e^{st} I(s) H_0^2(-js\, r/c)\, ds \qquad \text{(C-21)}$$

This equation can be simplified by making use of the integral representation for the Hankel function, namely

$$-jH_0^2(-js \frac{r}{c}) = \frac{2}{\pi} \int_0^\infty e^{-\frac{sr}{c} \cosh u}\, du$$

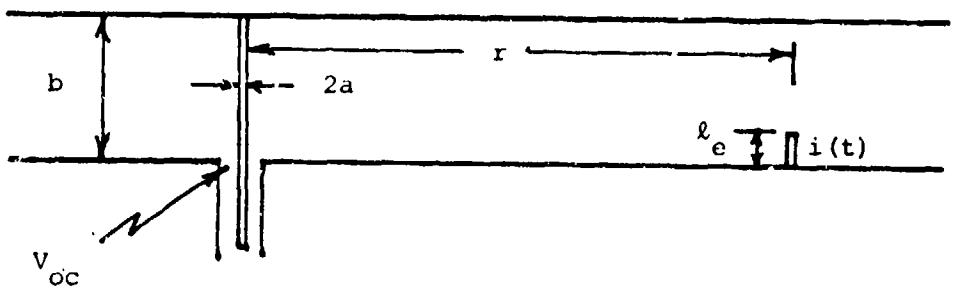

Figure C-5. Transient radiation between two parallel plates.

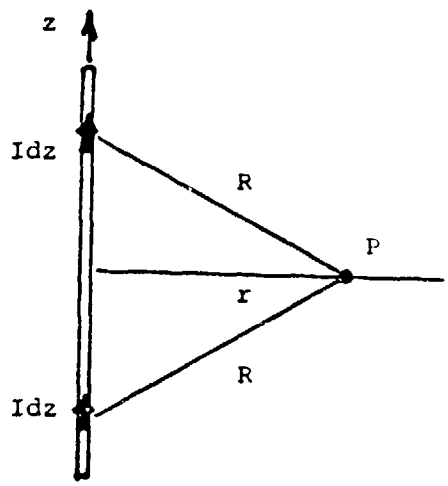

Figure C-6. Radiation from a line source formed by the images of the probe in the two parallel plates.

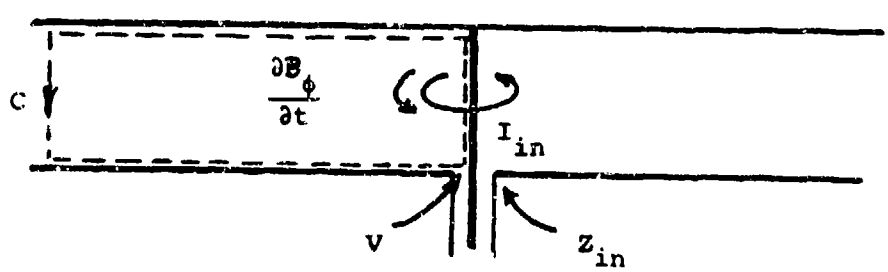

Figure C-7. Illustration for derivation of input impedance.

When we use this expression along with the inverse transform relationship

$$\frac{1}{2\pi j}\int_C e^{s(t-\frac{r}{c}\cosh u)} I(s)\,ds = i(t-\frac{r}{c}\cosh u)$$

we obtain

$$v_{oc}(t) = \frac{Z_0 \ell_e}{2\pi c}\,\frac{d}{dt}\int_0^\infty i(t-\frac{r}{c}\cosh u)\,du \qquad \text{(C-22)}$$

for $t \geq \frac{r}{c}\cosh u$. For earlier values of t, i is zero. We now let r cosh u = cv which transforms the integral into the form

$$v_{oc}(t) = \frac{Z_0 \ell_e}{2\pi c}\,\frac{d}{dt}\int_{r/c}^t \frac{i(t-v)}{\sqrt{v^2-(r/c)^2}}\,dv \qquad \text{(C-23)}$$

If the pulse duration is T and $t > T + r/c$ the lower limit in the integral is $t - T$.

The result given by (C-23) demonstrates the fundamental difference between radiation in a three dimensional space and that in a two dimensional space. In three dimensions a pulse of length T radiates a field also of duration T if the source is a point source. In two dimensions the source is a line source that extends to infinity and therefore at any time there will be a contribution to the field from the remote portions of the line source. Thus a pulse radiates a field with an infinitely long tail.

The result given by (C-23) can also be derived by beginning with the solution for a short current filament and integrating along the infinite line source. With reference to Figure C-6 the current elements at $\pm z$ will produce a z directed electric field at P given by

$$E = -\frac{jk_0 Z_C}{2\pi}\int_0^\infty \frac{e^{-jk_0 R}}{R}\,dz$$

The received open circuit voltage in the Laplace transform domain is thus

$$V_{oc}(s) = \frac{Z_0 \ell_e I(s)}{2\pi c} s \int_0^\infty \frac{e^{-sR/c}}{R} dz$$

In the time domain we obtain

$$v_{oc}(t) = \frac{Z_0 \ell_e}{2\pi c} \frac{d}{dt} \frac{1}{2\pi j} \int_0^\infty \int_C \frac{e^{s(t - R/c)}}{R} I(s)\, ds\, dz$$

$$= \frac{Z_0 \ell_e}{2\pi c} \frac{d}{dt} \int_0^\infty \frac{i(t - R/c)}{R} dz$$

where i is zero for $R > ct$. We now let $R^2 = z^2 + r^2 = c^2 v^2$, $dz = c^2 v\, dv/z$ and then

$$v_{oc}(t) = \frac{Z_0 \ell_e}{2\pi c} \frac{d}{dt} \int_{r/c}^t \frac{i(t - v)dv}{\sqrt{v^2 - r^2/c^2}}$$

which is the same as (C-23). The limits on the integral are dictated by the condition that $i(t - v)$ is zero for $v > t$ and that the first arrival of a signal at P occurs at a delayed time $t = r/c$.

Antenna Impedance Function

In order to calculate the voltage on the coaxial line as produced by the open circuit received voltage, it is necessary to have an expression for the input impedance function for the antenna. For an input current with time dependence $e^{j\omega t}$, the input impedance is approximately

$$Z_{in} = R + j X_L \qquad \text{(C-24)}$$

where R is given by (C-17) and X_L by (C-18). The radiation resistance is $\omega b Z_0/4c$ and is an odd function of ω. This is not a physically realizable impedance for which we can replace ω by $-js$. It would lead to a complex function in the time domain. Also X_L depends on the log of ω and this is a multivalued function. In order to obtain the appropriate impedance

function we return to the derivation of R and X_L. With reference to Figure C-7 assume that a voltage V across the coaxial transmission line excites a uniform current I_{in} on the antenna. The radiated electric field is given by

$$E_z = - \frac{k_0 Z_0}{4} H_0^2(k_0 r) I_{in}$$

The magnetic field B_ϕ is obtained from Maxwell's equation

$$\nabla \times \vec{E} = - j\omega \vec{B}$$

$$j\omega B_\phi = \frac{\partial E_z}{\partial r}$$

The line integral of $\vec{E}$ around the contour C shown in Figure C-7 equals -V since $\vec{E}$ is zero along the antenna, the parallel plates, and vanishes like $r^{-1/2}$ as r becomes infinite. The only contribution is from the open end of the coaxial line. The line integral also equals the negative total rate of change of magnetic flux through C, hence

$$-V = -j\omega \int_0^\infty \int_0^b B_\phi \, dr \, dz$$

or

$$V = b \int_0^\infty \frac{\partial E_z}{\partial r} dr = -b \, E_z(a)$$

We now see that

$$Z_{in} = \frac{V}{I_{in}} = \frac{k_0 b Z_0}{4} H_0^2(k_0 a)$$

$$= \frac{-jsbZ_0}{4c} H_0^2(-js\frac{a}{c})$$

upon replacing $j\omega$ by s. When sa/c is small we can use the small argument approximation for the Hankel function to obtain

$$Z_{in}(s) = \frac{-jsbZ_0}{4c}\left(1 + \frac{2j}{\pi}\ln\frac{2cj}{1.78\ sa}\right)$$

$$= \frac{sbZ_0}{2\pi c}\ln\frac{2c}{1.78\ sa} \qquad \text{(C-25)}$$

When $s = j\omega$ this reduces to the result given by (C-24). In order that the real part of $Z_{in}(s)$ will be equal to the real part of $Z_{in}(s^*)$ we must restrict the angle s in the complex plane to be between $-\pi$ and π by placing a branch cut along the negative real axis from the origin to infinity.

When $s = j\omega$ (C-25) gives

$$Z_{in}(\omega) = \frac{\omega bZ_0}{4c}\left(1 + \frac{2j}{\pi}\ln\frac{2c}{1.78\ \omega a}\right) \qquad \text{(C-26)}$$

When $s = -j|\omega| = |\omega|e^{-j\pi/2}$ we note that

$$\ln\frac{j}{s} = \ln\frac{e^{j\pi/2}}{|\omega|e^{-j\pi/2}} = \ln\frac{e^{j\pi}}{|\omega|} = j\pi + \ln\frac{1}{|\omega|}$$

and then see that (C-25) gives

$$Z_{in}(-\omega) = \frac{-|\omega|bZ_0}{4c}\left(1 - 2 + \frac{2j}{\pi}\ln\frac{2c}{1.78|\omega|a}\right) = R - jX_L \qquad \text{(C-27)}$$

As can be seen (C-25) does have the correct properties to be a physically meaningful impedance function.

Received Signal Waveform

In the Laplace transform domain the received signal voltage is (see Figure C-8)

$$V(s) = \frac{Z_c V_{oc}(s)}{Z_c + Z_{in}(s)}$$

When we introduce the Laplace transform of (C-23) to obtain $V_{oc}(s)$ and take the inverse transform of V(s) we obtain

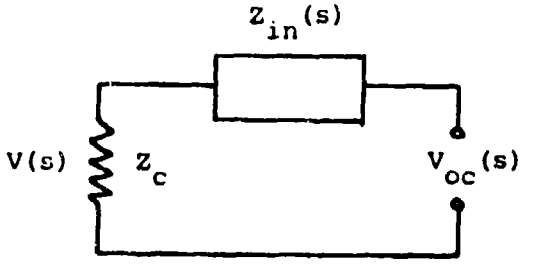

Figure C-8. Receiving equivalent circuit.

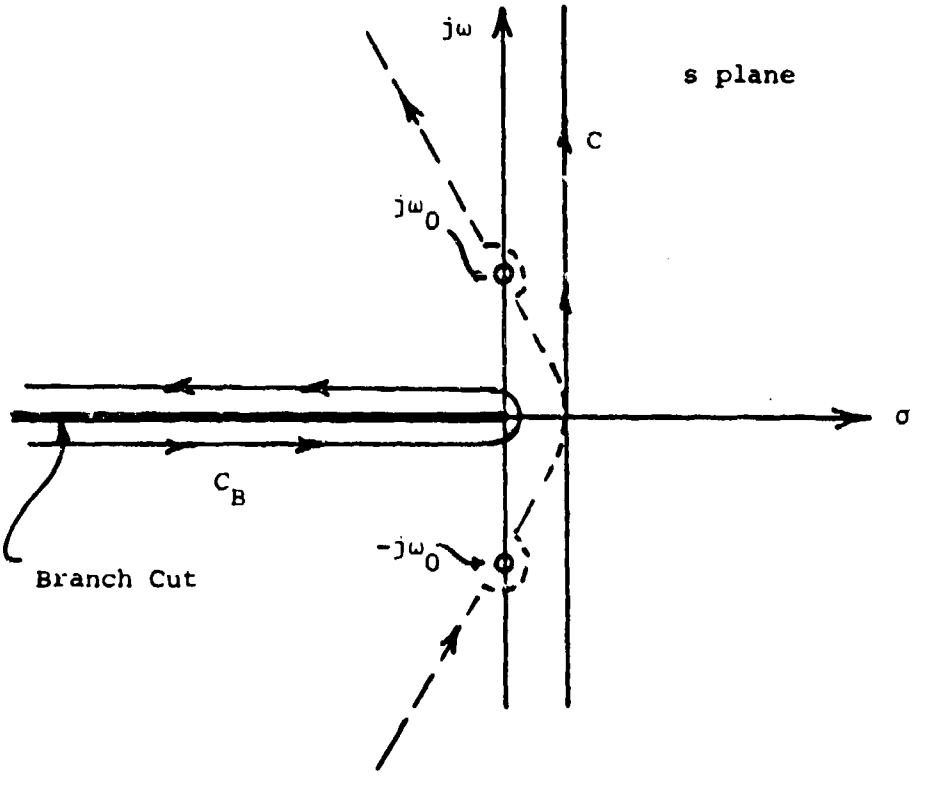

Figure C-9. Inversion contours for v(t).

$$v(t) = \frac{Z_0 Z_c \ell_e}{2\pi c} \int_{r/c}^{\infty} \frac{1}{\sqrt{v^2 - r^2/c^2}} \frac{1}{2\pi j} \int_C \frac{e^{st - sv} sI(s)ds}{Z_c + Z_{in}(s)} dv \qquad \text{(C-28)}$$

If we model the input pulse by the function $-I_0(1 - \cos \omega_0 t)$ for $0 \leq t \leq 2\pi/\omega_0 = T$, its Laplace transform will be

$$I(s) = -I_0 \frac{\omega_0^2}{s(s^2 + \omega_0^2)} (1 - e^{-sT}) \qquad \text{(C-29)}$$

Thus

$$v(t) = -\left\{\frac{Z_0 Z_c \ell_e I_0 \omega_0^2}{2\pi c} \int_{r/c}^{\infty} \frac{1}{\sqrt{v^2 - r^2/c^2}}\right\} \cdot \left\{\frac{1}{2\pi j} \int_C \frac{e^{s(t-v)}(1 - e^{-sT})\, ds}{(\omega_0^2 + s^2)[Z_c + Z_{in}(s)]} dv\right\} \qquad \text{(C-30)}$$

The contour is a line parallel to the imaginary axis in the right half plane. For $t - v > 0$ and $t - v - T > 0$ the contour can be closed in the half plane but not across the branch cut that is needed to keep $Z_{in}(s)$ single valued. When we close the contour in the manner shown in Figure C-9 the residues at the poles $\pm j\omega_0$ are picked up and the remainder is the branch cut integral along C_B.

The residue contributions give $v_1(t)$ where

$$v_1(t) = -\frac{Z_0 Z_c \omega_0 \ell_e I_0}{2\pi c \sqrt{(R+Z_c)^2 + X_L^2}} \int_{r/c}^{t} \frac{\sin[\omega_0(t-v) - \phi]}{\sqrt{v^2 - r^2/c^2}} dv \qquad \text{(C-31)}$$

for $v < t$ and $r < ct < r + cT$. When $ct > r + T$ the lower limit in (C-31) is replaced by $t - T$. In this equation R and X_L are as given by (C-17) and (C-18) for $k_0 = 2\pi/\lambda_0 = \omega_0/c$ and

$$\phi = \tan^{-1} \frac{X_L}{R+Z_c} \qquad \text{(C-32)}$$

The integral over v accounts for the long tail in the pulse response. This tail will decrease in amplitude for large t since the interval in v is from t - T to t and t becomes large relative to r/c so the pulse decays like $\ell n[t/(t-T)]$.

If the following change in variables is made

$$\lambda = cv/r \ , \quad t' = ct/r \ , \quad \omega_0' = \omega_0 \, r/c$$

the integral in (C-31) becomes

$$K(t') = \int_1^{t'} \frac{\sin\,[\omega_0'(t'-\lambda)-\phi]}{\sqrt{\lambda^2-1}}\, d\lambda$$

$$= \begin{cases} -\sin\phi\,\ell n(t'+\sqrt{t'^2-1}) + \omega_0' \int_1^{t'} \cos\,[\omega_0'(t'-\lambda)-\phi]\,\ell n(\lambda+\sqrt{\lambda^2-1})\, d\lambda & \text{for } 1<t'<1+T' \\ -\sin\phi\,\ell n \dfrac{(t'+\sqrt{t'^2-1})}{(t'-T'+\sqrt{(t'-T')^2-1})} + \omega_0' \int_{t'-T'}^{t'} \cos\,[\omega_0(t'-\lambda)-\phi]\,\ell n(\lambda+\sqrt{\lambda^2-1})\, d\lambda & \text{for } t'>1+T' \end{cases}$$

after integrating by parts once. The received signal is

$$v_1(t') = -\frac{Z_0 Z_c k_0 \ell_e I_0}{2\pi\sqrt{(R+Z_c)^2 + X_L^2}}\, K(t') \qquad \text{(C-33)}$$

The integral K(t') has been evaluated numerically and the results are tabulated below for the case when r = 30 cm, $r/c = 10^{-9}$, t' is measured in nanoseconds, and $\omega_0 = 8\pi \times 10^9$, $\omega_0' = 8\pi$, $\phi = 0.922$.

t' - 1	K(t')	t' - 1	K(t')
.000	.000	.225	-.145
.025	-.110	.250	-.220
.050	-.024	.275	-.081
.075	.110	.300	-.054
.100	.240	.325	-.040
.125	.300	.350	-.031
.150	.270	.500	-.012
.175	.160	.600	-.008
.200	-.001	.750	-.005

Note that there is a long tail associated with the received pulse but its amplitude is small. The input pulse length corresponds to $\Delta t' = T' = 0.25$ nanoseconds. The received signal is plotted in Figure C-10 where the following parameter values have been chosen.

T = 250 picosecs

ℓ_e = 3 mm

b = 2.5 cm

Z_c = 50 Ω

$2I_0$ = 10 ma

Probe radius a = 1 mm

R = 197.4 ohms

X_L = 326.17 ohms

r = 30 cm

The received signal is approximately 10 times larger than that for radiation over a ground plane. We have neglected the contribution from the branch cut integral which is expected to be small. If we had assumed that the probe impedance was constant the branch cut integral would not have arisen. The branch cut integral can be expressed in the form

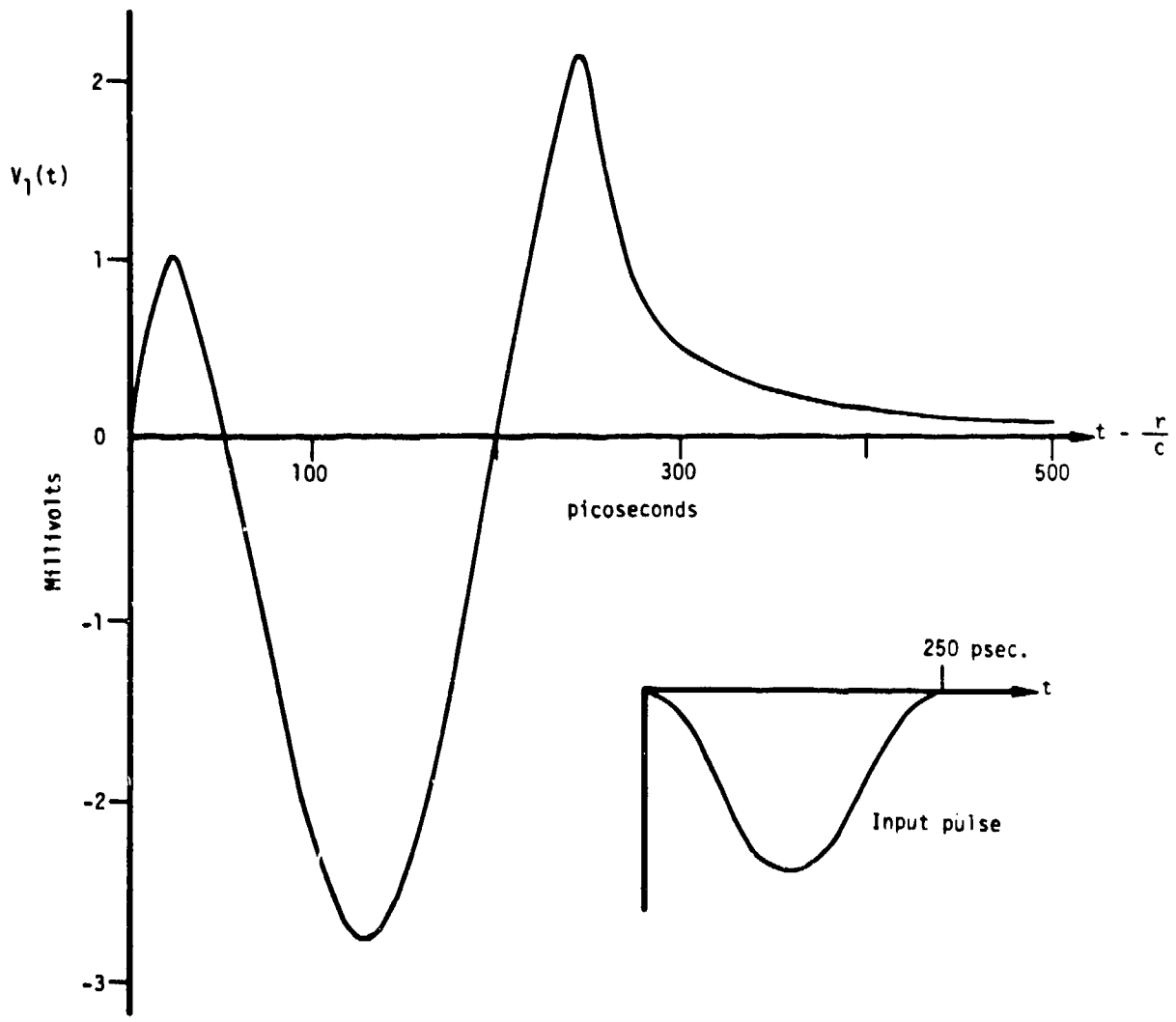

FIGURE C-10. RECEIVED SIGNAL FOR TRANSIENT RADIATION BETWEEN PARALLEL PLATES

$$v_B(t) = -\frac{Z_c \ell e I_0}{\pi^2} \int_{t_0'}^{t'} \frac{d\lambda}{\sqrt{\lambda^2-1}} \int_0^{\infty} e^{-\rho(t'-\lambda)} \frac{[1 - U(t'-1-T')\, e^{\rho T'}]\, d\rho}{(1 + \frac{\rho^2}{\omega_0'^2})[(\frac{2Z_c r}{bZ_0} - \frac{\rho}{\pi} \ln \frac{2r}{1.78a\rho}) + \rho^2]}$$

(C-34)

where $U(x) = 1$ for $x > 0$ and equals zero for $x < 0$. The lower limit t_0' in the integral over λ equals 1 for $t' < 1 + T'$ and equals $t' - T'$ when $t' > 1 + T'$. By estimating upper bounds on the integral in (C-34) it is found that its contribution to the received signal can be neglected.

APPENDIX D

A TRANSMISSION LINE CIRCUIT FOR AN ULTRA FAST SAMPLER

Transmission Line Circuit For Ultra Fast Sampler

In the discussion to follow it will be convenient to describe the length of a transmission line in terms of its equivalent time delay. Thus a line τ seconds long will have a physical length $\ell = v_0\tau$ where v_0 is the propagation velocity along the line. For example, if $v_0 = 0.7c$, c = speed of light, then a line 10 picoseconds long has a physical length of $0.7 \times 3 \times 10^{10} \times 10^{-11} = 0.21$ cm.

Consider a transient signal S(t) of duration T such as shown in Figure D-1a. If this signal is fed into a long transmission line then after a time interval T this signal is spatially spread out over a length T of transmission line as shown in Figure D-1b. An interchange between time and a spatial coordinate has been accomplished. If a photograph of the signal on the transmission line at time t = T could be taken, it would provide the time waveform. In place of sampling in time we can use spatial sampling along the transmission line. Hence, if we could acquire samples of the voltage on the transmission line at intervals 1/2B sec apart, these spatial samples would be equivalent to time samples and could be used to reconstruct the waveform.

A transmission line circuit for acquiring the spatial samples is shown in schematic form in Figure D-2. It consists of a main line of characteristic impedance Z_c terminated in a matched load at the far right hand side. A number of parallel connected branch lines a distance τ_s apart are connected to the main line through gallium-arsenide series switch elements. The number of branching lines equals the number of sample values required. The spacing τ_s equals the time duration that the series switches are on. Each branch line is of the same length (at least $\tau_s/2$

Transmission Line Circuit For Ultra Fast Sampler

In the discussion to follow it will be convenient to describe the length of a transmission line in terms of its equivalent time delay. Thus a line τ seconds long will have a physical length $\ell = v_0\tau$ where v_0 is the propagation velocity along the line. For example, if $v_0 = 0.7c$, c = speed of light, then a line 10 picoseconds long has a physical length of $0.7 \times 3 \times 10^{10} \times 10^{-11} = 0.21$ cm.

Consider a transient signal S(t) of duration T such as shown in Figure D-1a. If this signal is fed into a long transmission line then after a time interval T this signal is spatially spread out over a length T of transmission line as shown in Figure D-1b. An interchange between time and a spatial coordinate has been accomplished. If a photograph of the signal on the transmission line at time t = T could be taken, it would provide the time waveform. In place of sampling in time we can use spatial sampling along the transmission line. Hence, if we could acquire samples of the voltage on the transmission line at intervals 1/2B sec apart, these spatial samples would be equivalent to time samples and could be used to reconstruct the waveform.

A transmission line circuit for acquiring the spatial samples is shown in schematic form in Figure D-2. It consists of a main line of characteristic impedance Z_c terminated in a matched load at the far right hand side. A number of parallel connected branch lines a distance τ_s apart are connected to the main line through gallium-arsenide series switch elements. The number of branching lines equals the number of sample values required. The spacing τ_s equals the time duration that the series switches are on. Each branch line is of the same length (at least $\tau_s/2$

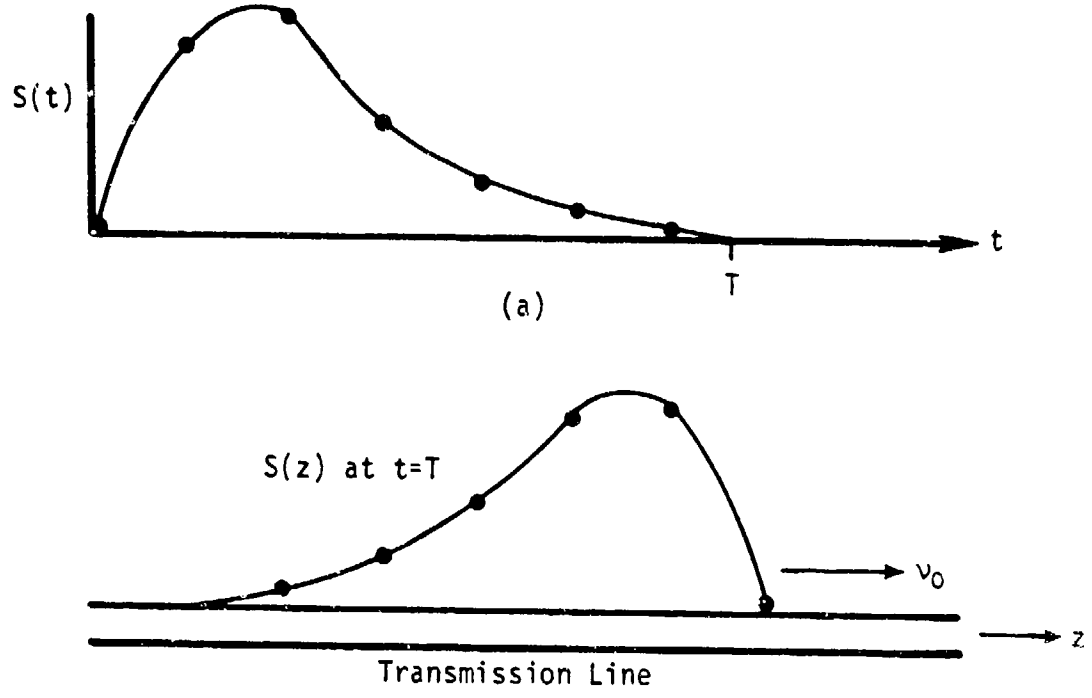

FIGURE D-1. (a). TRANSIENT SIGNAL IN TIME DOMAIN.

(b). TRANSIENT SIGNAL SPATIALLY DISTRIBUTED ALONG A TRANSMISSION LINE. THE DOTS SHOW DESIRED SAMPLE VALUES NEEDED TO RECONSTRUCT THE WAVEFORM.

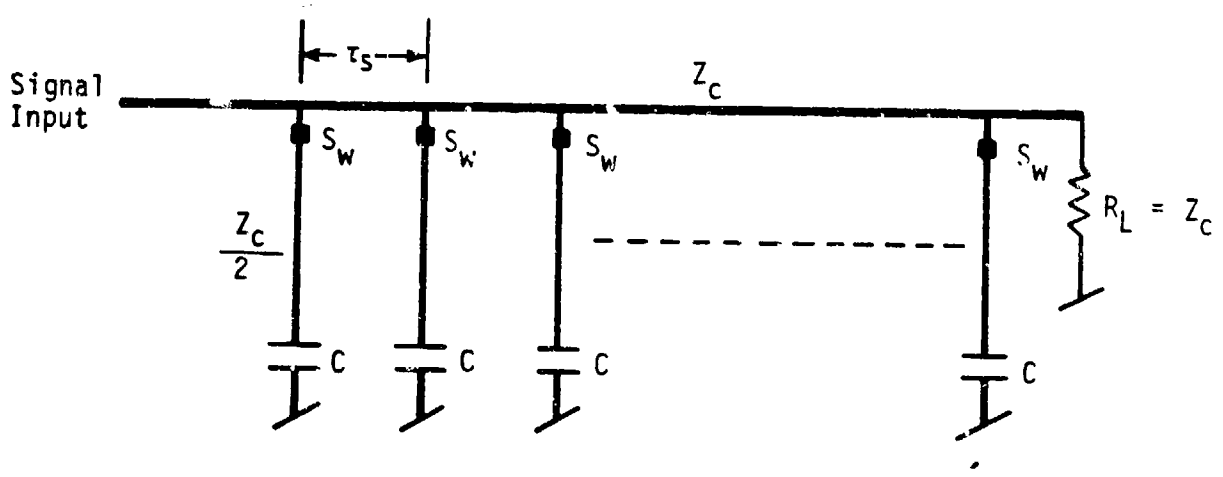

FIGURE D-2. TRANSMISSION LINE CIRCUIT FOR AN ULTRA FAST SAMPLER.

long) and is terminated in a capacitor C. For optimum power transfer into each branch line its characteristic impedance is $Z_c/2$ (this can be seen by noting that the impedance seen from the branch line looking into the main line is that of two lines with characteristic impedance Z_c connected in parallel). At the instant of time that the waveform to be sampled is properly positioned with respect to the sampling gates all switches are activated into the on state. Prior to this activation the branch lines are not connected so they produce only a small perturbation of the main line characteristics. This is important in order that the signal on the main line will be an accurate replica of the signal in the time domain.

Consider now what happens at the n'th sampling gate at the time that the switch is turned on (Figure D-3). The voltage signal on the main line is S_n. A voltage wave with initial value $S_n/2$ is launched into the n'th branch line and secondary waves of voltage $-S_n/2$ and propagating away from the junction in both directions are launched on the main line. As time progresses the signal moves to the right at a speed v_0 on the main line. When a time interval of length τ_s has elapsed a replica of the waveform between S_n and S_{n-1} has been launched onto the branch line. Also at this time the secondary waves are just arriving at the adjacent sampling gates on the main line. If however the switches open at this time, the secondary waves are not coupled onto the branch lines. Thus each branch line captures a portion of the main line signal of length τ_s and stores a voltage on the capacitor proportional to this. From the capacitor voltages the main line signal can be reconstructed. After the switches become non-conducting the waves on the main line are absorbed in the load R_L or reflected from the input end and eventually dissipated.

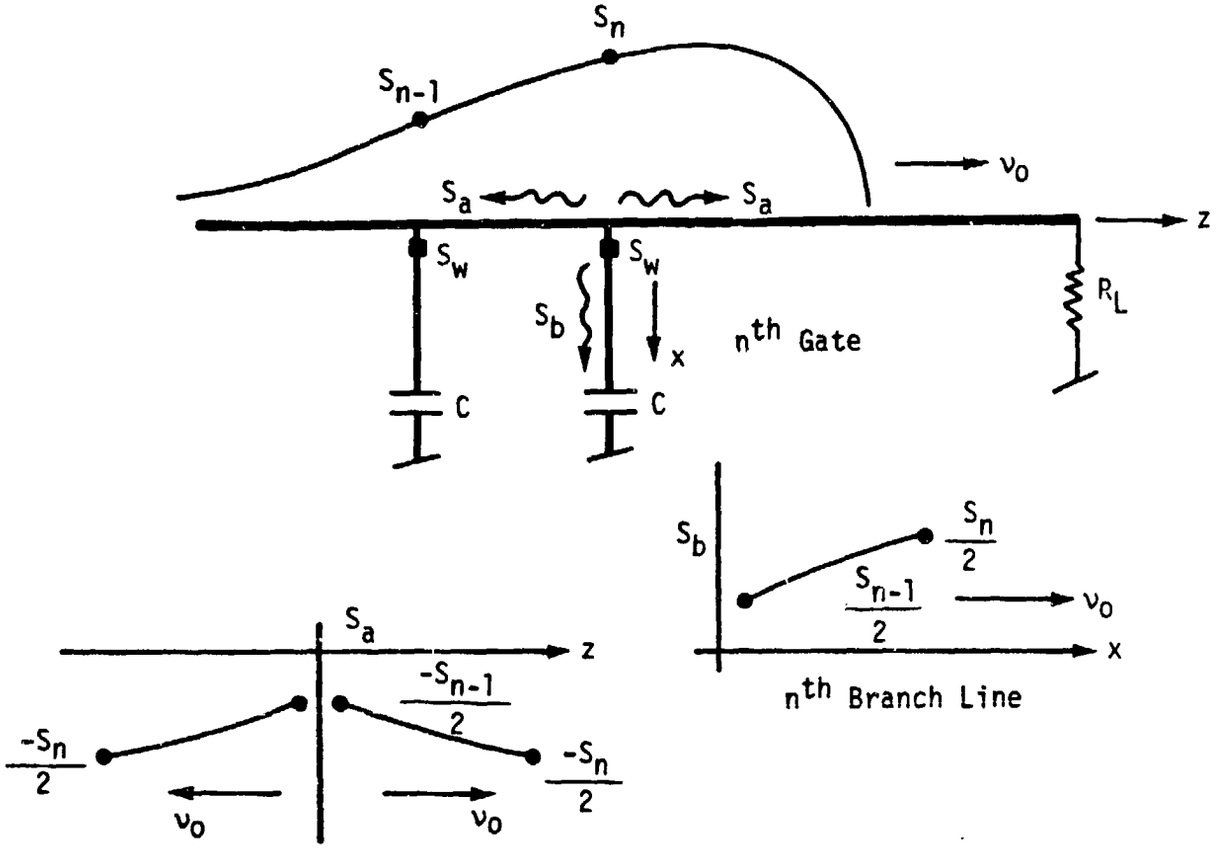

FIGURE D-3. TRANSIENT WAVEFORMS PRODUCED AT THE N'TH SAMPLING GATE WHEN THE SWITCH IS TURNED ON.

The basic principle of operation as outlined above is straightforward but for a more detailed understanding a complete analysis should be carried out. Some of the things that should be studied are:

(1) Optimum length for the branch lines.

(2) Optimum size capacitor to use.

(3) Ringing or multiple reflections on the branch line after the switch becomes highly resistive.

(4) Dissipation of the signal on the branch lines and the final voltage stored on the capacitors.

(5) The effect of the switch as it passes through the transition phase from on to off.

(6) Leakage through the switch.

(7) Dissipation of the signal on the main line. (This can be accounted for by weighting the capacitor voltages appropriately before waveform reconstruction is carried out.)

(8) Input coupling circuit and its transient response.

Physical limitations such as the switch on time τ_s and the minimum spacing between the branch lines that can be realized may result in an insufficient number of spatial samples. One way to overcome this problem is to use two or more sampler systems in parallel. For example, the number of spatial samples can be doubled by using the circuit shown in Figure D-4. In this system the signal is split and displayed on two main lines. The series of sampling gates on the second line are shifted by a distance $\tau_s/2$ in order to acquire sample values midway between those obtained on the first line.

In the ideal version of the proposed circuit there are several desirable features such as identical branch lines, no problems associated with line terminations, no multiple reflections to distort the sample

values, and no need to activate the switches in a sequential manner in time. The extent to which these features can be retained in a practical system will depend on the quality of the switching elements.

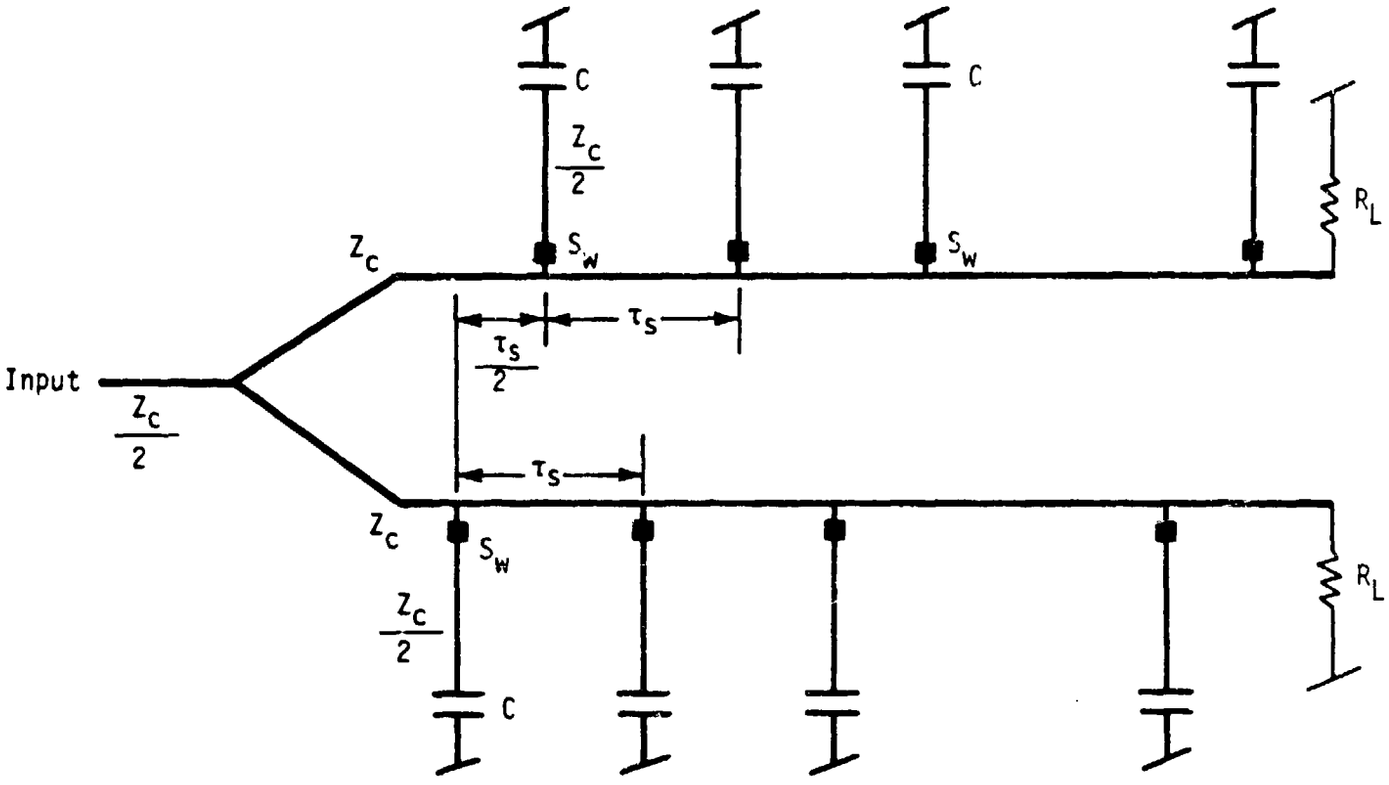

FIGURE D-4. A SAMPLER SYSTEM THAT DOUBLES THE NUMBER OF SPÁTIAL SAMPLES THAT CAN BE ACQUIRED.

APPENDIX E

SUMMARY OF TRANSMISSION LINE TRANSIENT PHENOMENA

APPENDIX E. SUMMARY OF TRANSMISSION LINE TRANSIENT PHENOMENA

For a loss free line the equations describing the voltage v(t,z) and current i(t,z) on the line are

$$\frac{\partial v}{\partial z} = -L \frac{\partial i}{\partial t}, \qquad \frac{\partial i}{\partial z} = -C \frac{\partial v}{\partial t}$$

From these equations we obtain

$$\frac{\partial^2 v}{\partial z^2} = LC \frac{\partial^2 v}{\partial t^2}, \qquad \frac{\partial^2 i}{\partial z^2} = LC \frac{\partial^2 i}{\partial t^2}$$

The solution for v is of the form

$$v = S^+(t - z/v_0) + S^-(t + z/v_0)$$

where $v_0 = (LC)^{-1/2}$ is the propagation velocity. S^+ is a voltage wave propagating in the +z direction while S^- is a voltage wave propagating in the -z direction. The associated current waves are

$$i^+ = Y_c S^+, \qquad i^- = -Y_c S^-$$

where $Y_c = (C/L)^{1/2}$ is the characteristic admittance of the line.

There are two basic ways to analyze transients on a transmission line. One method simply tracks the wave as it evolves in time and space and applies the proper terminal conditions in the time domain. The other method uses the Laplace transform technique and a form of analysis which is the same as that used for steady state sinusoidal signals but followed by an inverse Laplace transformation at the end.

Consider as an example a rectangular pulse input at z = 0, t = 0.

A capacitor C_1 is located a distance ℓ from the input. At time ℓ/v_0 the leading edge of the pulse arrives at the capacitor and then applies a voltage S^+ to C_1 for a time interval T where T is the pulse duration. Since C_1 is initially uncharged a reflected voltage wave $S^-(t - \ell/v_0)$ is produced. The incident and reflected current waves are $Y_c S^+ = i^+$ and $-Y_c S^-(t - \ell/v_0) = i^-$. The capacitor voltage v_1 equals $S^+ + S^-$ and the terminal condition $i_1 = C_1\, dv_1/dt$ must hold. Hence, we must have

$$Y_c(S^+ - S^-) = i = i_1 = C_1 \frac{d}{dt}(S^+ + S^-)$$

But S^+ is a constant during the pulse duration so

$$\frac{dS^-}{dt} = \frac{1}{C_1 Z_c} S^- + \frac{1}{C_1 Z_c} S^+$$

The solution for S^- is of the form

$$S^- = S^+ + A\, e^{-t/\tau}$$

where $\tau = C_1 Z_c$. At $t = \ell/v_0$ when the pulse first arrives $v_1 = 0$ so $S^- = -S^+$ initially. Hence,

$$S^- = -S^+ = S^+ + A\, e^{-\ell/\tau v_0} \qquad \text{and}$$

$$A = -2S^+ e^{\ell/\tau v_0} \qquad \text{and}$$

$$S^- = S^+[1 - 2\, e^{-(t-\ell/v_0)/\tau}]$$

This solution applies until time $t = \frac{\ell}{v_0} + T$ when the input pulse ceases. At this time the reflected wave has an amplitude $S^+[1 - 2\, e^{-T/\tau}]$. If the input end of the line is terminated in a matched generator no reflection of the wave reflected from C_1 occurs and C_1 will now simply discharge with

a time constant τ. Figure E-1 shows the relfected voltage waveform. Note that when S^+ drops to zero the reflected voltage wave increases by an amount S^+ in order to match the total line voltage to the capacitor voltage. If the pulse duration T is very long S^- will approach a value of S^+ and the final total line voltage and capacitor voltage will be $2S^+$. This condition must be achieved since when the capacitor is fully charged the line current is zero, i.e., $i^+ + i^- = 0$. The fully charged capacitor acts as an open circuit termination. If reflection from the generator end occurs then an additional voltage wave is launched and travels towards the capacitor and its effect must be tracked in time and position along the line. When there are several junctions and terminations it can become quite complex to track the multitude of waves that are generated. It then is more expedient to use the Laplace transform method of solution.

Laplace Transform Solution

We will illustrate the Laplace transform method by considering the same example as discussed above. The Laplace transform of the equations for v and i are:

$$\frac{\partial^2 V}{\partial z^2} = \frac{s^2}{v_0^2} V \ , \qquad \frac{\partial^2 I}{\partial z^2} = \frac{s^2}{v_0^2} I$$

where V and I are the transforms of v and i and the lower case s is the Laplace transform variable. The solutions for V and I are:

$$V = V^+ e^{-sz/v_0} + V^- e^{sz/v_0}$$

$$I = Y_c V^+ e^{-sz/v_0} - Y_c V^- e^{sz/v_0}$$

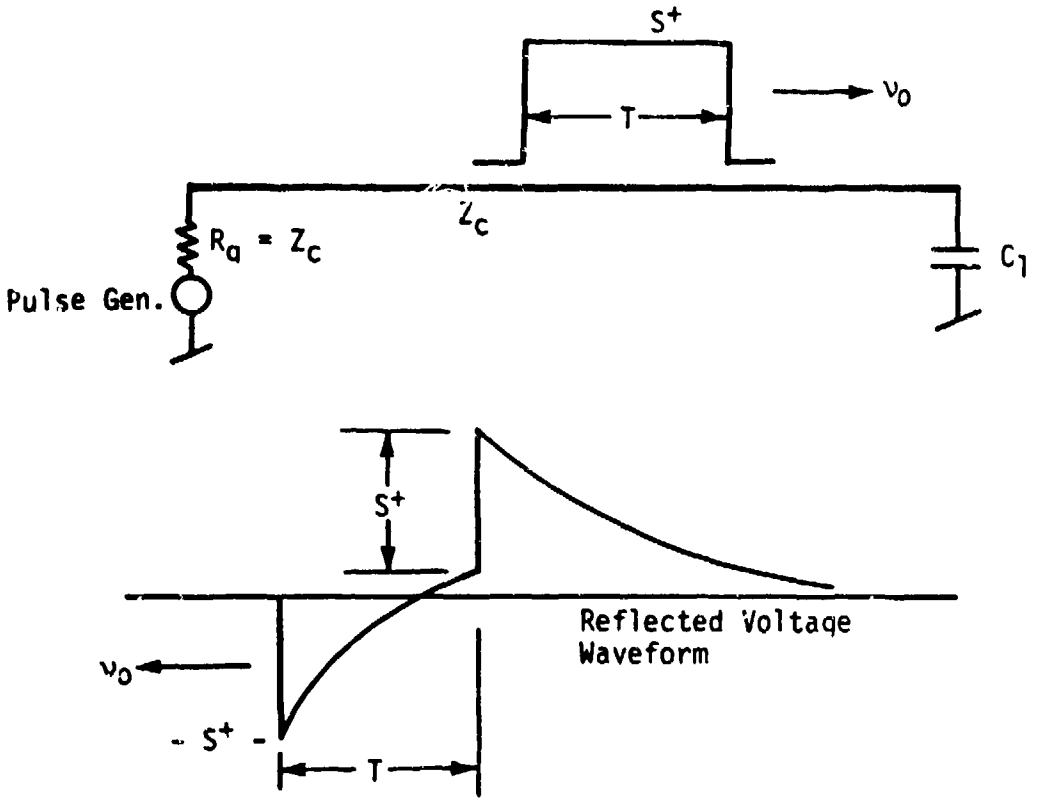

FIGURE E-1. TRANSIENT PULSE ON A TRANSMISSION LINE.

The reflection coefficient of the load is

$$R = \frac{Z_L - Z_c}{Z_L + Z_c} = \frac{\frac{1}{sC_1} - Z_c}{\frac{1}{sC_1} + Z_c} = \frac{1 - sC_1Z_c}{1 + sC_1Z_c} = \frac{1 - \tau s}{1 + \tau s}$$

Hence, $V^- e^{s\ell/v_0} = R\, V^+ e^{-s\ell/v_0}$. At the generator end we must have

$$V_g = V^+ + V^- + I_g Z_c = V^+ + V^- + Y_c(V^+ - V^-)Z_c = 2V^+$$

where V_g is the Laplace transform of the input signal. For a pulse of duration T and amplitude V_0 we get

$$V_g = V_0 \int_0^T e^{-st}\, dt = \frac{V_0}{s}(1 - e^{-sT})$$

The reflected wave at $z = \ell$ may now be found. It is given by

$$V^- e^{s\ell/v_0} = \frac{1 - s\tau}{1 + s\tau} e^{-s\ell/v_0} \frac{V_0}{2s}(1 - e^{-sT})$$

The inverse Laplace transform of this waveform is the same signal as found earlier. No reflection occurs before $t = \ell/v_0$ as can be seen from the delay factor $e^{-s\ell/v_0}$.

Switched Branching Line

Figure E-2 shows a signal S(z) on a transmission line at t = 0. At t = 0 the branch line is switched to the main line. As a result, voltage waves

$$S_1(t - z/v_0)\ , \qquad S_2(t + z/v_0)\ , \qquad S_3(t - x/v_0)$$

are launched on the three lines. The corresponding current waves are

$$Y_1S_1\ , \qquad -Y_1S_2\ , \qquad Y_2S_3$$

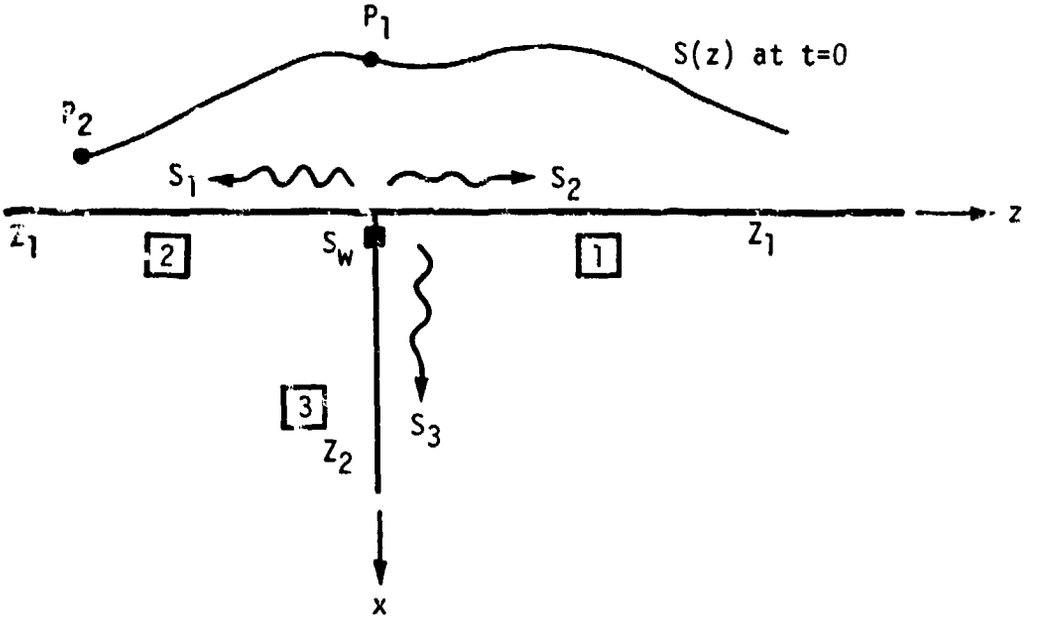

FIGURE E-2. A SWITCHED BRANCH LINE - MAIN LINE JUNCTION.

Since all three lines are connected in parallel, the total voltage on each line must be the same. thus

$$S + S_1 = S + S_2 = S_3 \quad \text{and hence} \quad S_1 = S_2.$$

The sum of the currents entering the junction node must be zero so we also have

$$Y_1(S - S_2) - Y_1(S + S_1) - Y_2S_3 = 0$$

Since $S_1 = S_2$ we obtain

$$2Y_1S_1 = -Y_2S_3 = -Y_2(S + S_1)$$

Thus we find that

$$S_1 = \frac{-Y_2}{2Y_1 + Y_2} S = RS$$

where R is the reflection coefficient seen on the input line 2. The solution for S_3 is

$$S_3 = \frac{2Y_1}{2Y_1 + Y_2} S = (1 + R)S$$

The power flow on line 3 is given by $\frac{1}{2} Y_2S_3^2 = \frac{1}{2} Y_2(1 + R)^2S^2$. This expression can be maximized with respect to the parameter Y_1/Y_2 and it is then found that the optimum value of Y_2 is $Y_2 = 2Y_1$. Only the portion of the original waveform S from the point P_1 to the point P_2 is launched onto the three lines after the switch is activated.

APPENDIX F.

FABRICATION PROCESS FOR THE OPTICALLY SENSITIVE GaAs SWITCH

APPENDIX F. FABRICATION PROCESS FOR THE OPTICALLY SENSITIVE GaAs SWITCH

Fabrication Process

Two alternative methods of fabrication of the devices have been explored. Process TYPE 1 which was first used is the more involved and utilizes four photoresist masking steps. The Process TYPE 2 combines the ohmic contact metal mask (MCM-3) and the stripped connection mask (MMC-4) thus saving on one photoresist step. Another major difference between the two processes is that a Si_3N_4 capping layer was used under the implant resist mask in process TYPE 1 while in process TYPE 2 only photoresist was used as the implant masking medium. In both processes the GaAs surface was uncapped during implantation in the source and drain regions.

FABRICATION PROCESS TYPE 1

1. GaAs surface preparation:
   - (i) Wafers degreased in isopropyl alcohol for 2 minutes.
   - (ii) Rinsed in DI water for 2 minutes.
   - (iii) Etch cleaned for 1 minutes at 40°C in the mixture:

DI H_2O	40 parts (by volume)
H_2SO_4	1 part (by volume)
H_2O_2	1 part (by volume)

   - (iv) Rinsed in DI water for 2 minutes.
   - (v) Etched for 1 minute in concentrated HCl.
   - (vi) Rinsed in DI water for 2 minutes.
   - (vii) Blown dry in filtered N_2.
2. Si_3N_4 cap of 1000 Å thickness deposited by plasma CVD process.

3. Photoresist implant mask lithography:

   (i) Baked at 180°C for 1 hour.

   (ii) HMDS spun for 40 seconds at 3000 RPM.

   (iii) AZ1350 spun for 40 seconds at 3000 RPM.

   (iv) Soft baked at 85°C for 1 hour.

   (v) Mask MSD-1 exposed for 15 seconds to mercury-arc source.

   (vi) Developed in (5:1) H_2O:DEV for 30 seconds.

   (vii) Rinsed in DI H_2O for 2 minutes.

   (viii) Hard baked at 85°C for 30 minutes.

   (ix) Si_3N_4 Plasma etched in CF_4 at 0.6 mm pressure and 100 Watts RF power for 1 minute.

4. Source-drain region implantation.

   (i) Wafer #B1W1G given silicon implants only:

Si^+ energy	Dose
100 keV	10^{13} cm^{-2}
160 keV	10^{13} cm^{-2}

   (ii) Wafer #B2W1G given silicon and phosphorus implants:

Si^+ energy	Dose
100 keV	10^{13} cm^{-2}
160 keV	10^{13} cm^{-2}
P^+ energy	
120 keV	10^{13} cm^{-2}
190 keV	10^{13} cm^{-2}

5. Photoresist stripping.

   (i) Soaked in acetone and scrubbed with Q-tip.

   (ii) Residue removed by plasma washing in O_2 plasma at 0.6 mm pressure and 150 Watts RF power for 5 minutes.

(iii) Rinsed in isopropyl alcohol for 2 minutes.

(iv) Rinsed in DI H_2O for 2 minutes.

(v) Etched in concentrated HCl for 1 minute.

(vi) Rinsed in DI H_2O for 2 minutes.

(vii) Blown dry with filtered N_2.

6. Annealing of implantation.

(i) 2000 Å of SiO_2 deposited on both sides of wafers by reactive sputtering in 35% O_2 in Argon at 400 Watts RF power for 30 minutes.

(ii) Implants annealed at 850°C, in forming-gas for:

Wafer #B1W1G: 30 minutes

Wafer #B2W1G: 15 minutes

7. Ohmic contact window lithography.

(i) AZ1350 Spun at 5000 RPM for 40 seconds.

(ii) Soft baked at 85°C for 30 minutes.

(iii) Mask MCW-2 aligned and exposed for 12 seconds.

(iv) Developed in (5:1) H_2O:DEV for 40 seconds.

(v) Rinsed in DI water for 2 minutes.

(vi) Blown dry in filtered N_2.

(vii) Postbaked at 85°C for 30 minutes.

(viii) SiO_2 etched for 2 minutes in 10% buffered HF.

(ix) Si_3N_4 etched in CF_4 plasma at 100 Watts RF power for 2 minutes.

(x) Resist stripped by soaking in acetone and scrubbing.

(xi) Resist residues removed by washing in O_2 plasma at 0.6 mm pressure and 100 Watts RF power and for 5 minutes.

8. Ohmic contact metal lithography.

   (i) AZ1350 spun at 2500 RPM for 40 seconds.

   (ii) Prebaked at 85°C for 15 minutes.

   (iii) Mask MCM-3 aligned and exposed for 15 seconds.

   (iv) Soaked in chlorobenzene for 5 minutes.

   (v) Blown dry with filtered H_2.

   (vi) Developed in (5:1) H_2O:DEV solution for 70 seconds.

   (vii) Rinsed in DI H_2O for 2 minutes.

   (viii) Postbaked at 85°C for 30 minutes.

   (ix) Unwanted metal removed by liftoff in hot acetone followed by ultrasound agitation.

   (x) Resist residues removed by washing in O_2 plasma.

9. Formation of ohmic contacts.

   (i) Sintering furnace temperature set at 450°C.

   (ii) Contacts alloyed for 2.5 minutes.

10. Source/drain metal lithography.

   (i) AZ1350 spun at 2500 RPM for 30 seconds.

   (ii) Prebaked at 85°C for 15 minutes.

   (iii) Mask MMC-4 aligned and exposed for 15 seconds.

   (iv) Soaked in chlorobenzene for 5 minutes and blown dry with filtered N_2.

   (v) Developed in (5:1) H_2O:DEV for 60 seconds.

   (vi) Rinsed in DI H_2O and blown dry.

   (vii) Postbaked at 85°C for 30 minutes.

11. Source/drain metal deposition.

   (i) Wafers loaded into evaporator and system evacuated to 2×10^{-6} Torr.

(ii) 200 Å of nickel evaporated.

(iii) 1000 Å of gold evaporated.

(iv) Unwanted metal removed by liftoff in hot acetone followed by ultrasound agitation.

(v) Resist residues removed in O_2 plasma at 100 W for 5 minutes.

FABRICATION PROCESS TYPE 2

1. GaAs surface prepared as in 1-1 above.

Implant window lithography.

(i) Wafers baked at 180°C for 1 hour.

(ii) HPR-206 spun at 5000 RPM for 30 seconds.

(iii) Soft baked at 105°C for 30 minutes

(iv) Mask MSD-1 exposed for 10 seconds.

(v) Developed in (1:1) H_2O:DEV solution for 20 seconds.

(vi) Rinsed in DI H_2O for 2 minutes.

(vii) Blown dry and postbaked at 125°C for 30 minutes.

(viii) GaAs slightly etched for 2 minutes in:

DI H_2O	100 parts
H_2SO_4	1 part
H_2O_2	1 part

3. Wafers implanted with Si at 100 keV and a dose of $10^{13} cm^{-2}$.

4. Si_3N_4 cap deposition.

(i) Resist stripped in O_2 plasma at 0.6 mm pressure and 150 Watts RF power for 10 minutes.

(ii) Rinsed in isopropyl alcohol for 2 minutes.

(iii) Rinsed in DI H_2O for 2 minutes.

(iv) Etched in concentrated HCl for 1 minute.

(v) Rinsed in DI H_2O for 2 minutes.

(vi) Blown dry in filtered N_2.

(vii) 1000 Å of Si_3N_4 deposited on front surface by plasma CVD.

5. 2000 Å SiO_2 cap deposited on both sides of wafers by reactive sputtering of silicon in 35% O_2 in Argon at 20 milliTorr and 400 Watts RF power.

6. Ion implants annealed at 850°C for 15 minutes.

7. SiO_2 layer removed by etching in 10% HF in NH_4F solution for 1.5 minutes.

8. Formation of ohmic contact windows.

(i) Wafers baked for 30 minutes at 180°C.

(ii) AZ1350J spun at 2500 RPM for 40 seconds.

(iii) Soft baked for 20 minutes at 85°C.

(iv) Mask MCW-2 aligned and exposed for 10 seconds.

(v) Soaked in chlorobenzene for 5 minutes.

(vi) Developed in (5:1) H_2O:DEV solution for 70 seconds.

(vii) Rinsed in DI H_2O for 2 minutes.

(viii) Blown dry with filtered N_2.

(ix) Postbaked 30 minutes at 85°C.

(x) Si_3N_4 etched for 2 minutes in CF_4 plasma at 100 Watts RF power.

9. Ohmic contact metal deposited as described in 1-8 above.

10. Contacts alloyed as described in 1-9 above.

11. Source/drain metal lithography.

(i) AZ1350 spun at 2500 RPM for 40 seconds.

(ii) Soft baked at 85°C for 15 minutes.

(iii) Mask MCM-3 aligned and exposed for 10 minutes.

(iv) Mask for MMC-4 aligned and exposed for 10 seconds.

(v) Soaked in chlorobenzene for 5 minutes.

(vi) Blown dry with filtered N_2.

(vii) Developed in (5:1) H_2O:DEV solution for 70 seconds.

(viii) Rinsed in DI H_2O for 2 minutes.

(ix) Blown dry with filtered N_2.

(x) Postbaked at 85°C for 30 minutes.

12. Source/drain nickel deposition.

(i) Wafers loaded into evaporator and system evaluated to 2×10^{-6} Torr.

(ii) 600 Å of nickel evaporated.

(iii) Excess metal removed by liftoff in hot acetone followed by ultrasound agitation.

(iv) Rinsed in hot isopropyl alcohol followed by cold isopropyl alcohol dip.

(v) Resist residues removed in O_2 plasma for 5 minutes at 150 Watts RF power.

(vi) Wafers baked for 30 minutes at 180°C.

13. Steps in 12 above were repeated for 0.5 μm aluminum to give a thick contact metal suitable for bonding purposes.

REFERENCES

1. Bennett, C.L., and Ross, G.F., "Time-Domain Electromagnetics and Its Applications", Proceedings of the IEEE, Vol 66, pp. 299-318, (March 1978).

2. Auston, D.H., Glass, A.M., and Ballman, A.A., "Optical Rectification By Impurities in Polar Crystals", Physics Review Letters, Vol 28, pp. 897-900 (April 1972).

3. Auston, D.H., and Glass, A.M., "Optical Generation of Intense Picosecond Electrical Pulses", Applied Physics Letters, Vol 20, pp. 398-399 (May 1972).

4. Peake, W.H., Meadors, J.G., Poirier, M.A., Young, J.D., and Richmond, J.H., "Laser Induced Transient Excitation of Conducting Targets", Report 784786-3, March 1980, The Ohio State University ElectroScience Laboratory, Department of Electrical Engineering; prepared under contract DASG60-77-C-0134 for Ballistic Missile Systems Command.

5. Lawton, R.A., and Scavannec, A.S., "A Photoconductive Detector of Fast Transition Waveforms", Electronic Letters, Vol 11, pp. 74-75 (February 1975)

6. Auston, D.H., Johnson, A.M., Smith, P.R. and Bean, J.C., "Picosecond Optoelectronic Detection, Sampling, And Correlation Measurements In Amorphous Semiconductors", Applied Physics Letters, Vol 37, No. 4, pp. 371-373 (August 1980).

7. Lee, C.H., "Picosecond Optoelectronic Switching in GaAs", Applied Physics Letters, Vol 30, No. 2, (January 1977).

8. Foyt, A.G., Leonberger, F.J. and Williamson, R.C., "Picosecond InP Optoelectronic Switches", Applied Physics Letters, Vol 40, No. 6, pp. 447-449 (March 1982).

9. Margulis, W., and Sibbett, W., "Picosecond CdSe Photodetector", Applied Physics Letters, Vol 42, No. 11, (June 1983).

10. Harrington, R.F. and Auckland, D.T., "Electromagnetic Transmission through Narrow Slots in Thick Conducting Screens", IEEE Transactions on Antenna and Propagation, Vol AP-28, pp. 616-622 (September 1980).

11. Kreyszig, E. Advanced Engineering Mathematics , Wiley, New York, pp. 680-688 (1962).

12. Harrington, R.F. and Auckland, D.T., op.cit.

13. Balanis, Constantine A., Antenna Theory: Analysis and Design , Harper & Row, Publishers, Inc. (1982).

14. Stutzman, W.L., and Thiele, G.A., Antenna Theory and Design , John Wiley and Sons, Inc. (1981).

15. Harrington, R.F., Time Harmonic Electromagnetic Fields, McGraw-Hill Book Company (1961).

REFERENCES (continued)

16. Meadors, J.G., and Poirier, M.A., "Laser Induced Transient Excitation of Conducting Targets by Thermionic Emission", J. Applied Physics, Vol 52, p. 449 (January 1981).

17. Peake, W.H., Meadors, J.G., and Poirier, M.A., "Laser Induced Transient Excitation of Conducting Targets", Applied Physics Letters, Vol 34, p. 844 (November 1980).